SEPTEMBER 1958 VOLUME 3 (1958) No. 3

GREGG M. SINCLAIR LIBRARY
UNIVERSITY OF HAWAII
8-7-63

NUCLEAR INSTRUMENTS & METHODS

A JOURNAL ON ACCELERATORS, INSTRUMENTATION AND TECHNIQUES IN NUCLEAR PHYSICS

EDITOR: K. SIEGBAHN - UPPSALA

CONTENTS

GEORGES HALL, Effets causés par la collection des électrons dans une chambre d'ionisation cylindrique 121
R. E. GREEN and R. E. BELL, Notes on a fast time-to-amplitude converter 127
L. A. KÖNIG und H. HINTENBERGER, Massenspektrographen mit korrigierten Bildfehlern . . 133
R. A. HEFFERLIN and W. E. KREGER, Collimator penetration and scattering effects 149
HERWIG SCHOPPER, Measurement of circular polarization of γ-rays 158
PETER WEINZIERL and GEORG TISLJAR-LENTULIS, Two-crystal-Compton-spectrometer with improved geometrical efficiency (Letter to the Editor) 177
Book reviews 179

NORTH-HOLLAND PUBLISHING COMPANY - AMSTERDAM

NUCLEAR INSTRUMENTS AND METHODS

A journal on accelerators, instrumentation and techniques in nuclear physics

EDITOR: K. SIEGBAHN, UPPSALA

EDITORIAL BOARD:

J. B. ADAMS (CERN)
F. A. ALSINA (Buenos Aires)
E. AMALDI (Rome)
H. L. ANDERSON (Chicago)
K. T. BAINBRIDGE (Cambridge, Mass.)
P. R. BELL (Oak Ridge)
R. E. BELL (Montreal)
A. BERTHELOT (Saclay)
H. BRINKMAN (Groningen)
E. H. COOKE-YARBOROUGH (Harwell)
S. DE BENEDETTI (Pittsburgh)
M. DE HEMPTINNE (Louvain)
A. DE-SHALIT (Rehovoth)
M. DEUTSCH (Cambridge, Mass.)
S. DU TOIT (Pretoria)
B. S. DŽELEPOV (Leningrad)
W. GENTNER (Heidelberg)
P. C. GUGELOT (Amsterdam)
H. HALBAN (Paris)
O. HAXEL (Heidelberg)
P. HUBER (Basel)
S. KIKUCHI (Tokyo)
J. KOCH (Copenhagen)
M. S. KOZODAEV (Moscow)
S. LIVINGSTON (Cambridge, Mass.)
E. M. MCMILLAN (Berkeley)
M. G. MEŠČERJAKOV (Moscow)
P. B. MOON (Birmingham)
M. L. OLIPHANT (Canberra)
W. PAUL (Bonn)
A. S. RAO (Bombay)
G. SALVANI (Rome)
P. SAVIĆ (Belgrade)
P. SCHERRER (Zürich)
CH. SCHMELZER (CERN)
H. W. B. SKINNER (Liverpool)
R. TANGEN (Oslo)
D. TAYLOR (Northampton)
V. I. VEKSLER (Moscow)
G. VON DARDEL (CERN)
O. WERNHOLM (Stockholm)
R. R. WILSON (Cornell)
S. D. WINTER (Saclay)

INSTRUCTIONS FOR CONTRIBUTORS

Contributions may be sent to the Editor, Professor K. Siegbahn, Institute of Physics, University of Uppsala, Sweden, either directly or through the intermediation of one of the members of the Editorial Board. Contributions may be written in English, French or German but should always, except for very short papers, be supplied with a brief abstract in English. Figures should be in inked original drawings or glossy prints and they should be sufficiently large. Contributors should make sure that important details in drawings and photographs will show up clearly in the diminished copy used by the publisher.

Books for review should be sent to Professor Siegbahn.

Objective and descriptive material on endeavours and product developments from the industry for the section "Spotlight on Industry" should be sent directly to the publishers, North-Holland Publishing Company, P.O. Box 103, Amsterdam.

Nuclear Instruments and Methods is published monthly. The subscription price of a volume of 360 pages is $ 17.00 (130 s), postage free.

Subscriptions should be sent to the publishers, North-Holland Publishing Company, P.O. Box 103, Amsterdam or to any subscription-agent.

No part of this issue may be reproduced in any form, by print, photoprint, microfilm or any other means without written permission from the publisher.

NUCLEAR INSTRUMENTS 3 (1958) 121–126; NORTH-HOLLAND PUBLISHING CO. – AMSTERDAM

EFFETS CAUSÉS PAR LA COLLECTION DES ÉLECTRONS DANS UNE CHAMBRE D'IONISATION CYLINDRIQUE

GEORGES HALL

Département de Physique, Université Laval, Quebec, Canada

Received 6 June 1958

The effect of using electron collection in a cylindrical, pulse ionization chamber is analysed. Ionizing trajectories crossing the chamber from end to end and ideal conditions are assumed. The probability of observing pulses of a given amplitude is shown to depend on this amplitude. The resulting statistical distribution of pulse amplitudes to be expected under typical conditions of operation is calculated as an example, from Landau's theoretical distribution of energy losses.

1. Introduction

La méthode la plus directe pour étudier l'ionisation produite dans un gaz par le passage d'une particule chargée, consiste à utiliser une chambre d'ionisation à impulsions, remplie de ce gaz. Les précautions à prendre pour que la grandeur d'une impulsion induite sur l'électrode collectrice soit rigoureusement proportionnelle au nombre d'ions initialement produits par la particule chargée sont bien connues aujourd'hui.

Cette méthode est cependant rarement utilisée lorsque la particule chargée est faiblement ionisante, parce que dans ce cas le bruit ou "souffle" de l'amplificateur peut fausser sérieusement les observations, à moins qu'on ne prenne soin (1) de réduire ce bruit autant que possible par un choix judicieux des constantes de temps de l'amplificateur et l'emploi de la collection des électrons[1]) et (2) de favoriser la production d'impulsions aussi grandes que possible en utilisant un gaz sous pression et, si la chambre est cylindrique, en disposant l'axe de celle-ci parallèlement aux trajectoires des particules ionisantes.

L'emploi conjugué de la collection des électrons et d'une chambre d'ionisation entraîne cependant une importante difficulté: dans ce cas, la grandeur des impulsions observées ne dépend pas seulement du nombre d'ions formés, mais aussi de l'endroit dans la chambre où ces ions ont été formés.

Nous étudierons les conséquences de cet effet dans le cas où les conditions sont idéales; nous supposerons (1) que toutes les trajectoires des particules ionisantes sont rectilignes et traversent complètement le volume sensible de la chambre d'ionisation, dans le sens de sa longueur, (2) que le taux d'ionisation est uniforme tout le long d'une trajectoire et le même pour toutes les trajectoires, (3) que les ions formés sont au repos, aussitôt après le passage de la particule ionisante et ne se mettent en mouvement que sous l'influence du champ électrique établi à l'intérieur de la chambre, (4) que ce champ électrique a une symétrie parfaitement cylindrique, jusqu'aux confins du volume sensible de la chambre, (5) que tous les effets secondaires: recombinaison, formation d'ions négatifs, diffusion, charge d'espace, etc., sont négligeables.

Cherchons quelle sera, dans ces conditons, la grandeur d'une impulsion causée par une trajectoire quelconque.

2. Grandeur d'une Impulsion

Supposons qu'une différence de potentiel adéquate est maintenue entre les deux électrodes de la chambre et qu'au temps $t = 0$, il se forme une paire d'ions à une distance r de l'axe. Le potentiel de l'électrode extérieure (généralement

[1]) R. Sherr et R. Peterson, Rev. Sci. Instr. 18 (1947) 567.

la cathode) est maintenu par une source de tension à basse impédance. On choisit par contre la constante de temps de l'électrode intérieure longue par rapport au temps de collection des électrons (mais courte par rapport au temps de collection des ions positifs). Celle-ci peut donc être considérée comme isolée (en ce qui concerne les charges induites par le mouvement d'un électron), et il s'y induira une charge q lorsque, sous l'influence du champ électrique, un électron (de charge e) se déplacera de r à r_t. Par des considérations électrostatiques, on démontre[2]) que

$$q = -\frac{e}{\ln b/a} \ln r/r_t \qquad (1)$$

où a et b sont les rayons de l'électrode intérieure et de l'électrode extérieure, respectivement. (Nous négligerons comme on le fait couramment, la charge induite par le mouvement des ions positifs, parce que leur mobilité est environ 1000 fois plus faible que celle des électrons.)

Si λ paires d'ions sont produites par unité de longueur, toutes à la même distance r de l'axe d'une chambre de longueur L (et pratiquement dans le même temps), la charge induite au temps t par le déplacement des électrons de r à r_t sera:

$$Q = -\frac{\lambda L e}{\ln b/a} \ln r/r_t \,.$$

Un cas plus général qu'on néglige toujours de traiter est celui d'une trajectoire oblique quelconque telle que représentée à la figure 1. L'équation (1) nous permet d'exprimer la charge qui aura été induite au temps t, alors que les électrons formés dans l'élément de trajectoire ds se seront déplacés de r à r_t:

$$\mathrm{d}Q = -\frac{e\lambda}{\ln b/a}\left(\ln \frac{r}{r_t}\right)\frac{\mathrm{d}y}{\cos\theta} \,.$$

Quand tous les électrons auront atteint l'électrode intérieure, le potentiel de celle-ci, c'est-à-dire la grandeur de l'impulsion sera donnée par:

$$V = \frac{1}{C}\int \mathrm{d}Q = \frac{Q}{C} = \frac{-e\,\lambda}{C\cos\theta \ln b/a}\int_0^L \ln\frac{r}{a}\cdot \mathrm{d}y \qquad (2)$$

[2]) B. B. Rossi et H. H. Staub, Ionization Chambers and Counters (McGraw-Hill, 1949); D. H. Wilkinson, Ionization Chambers and Counters (Cambridge, 1950).

si on désigne par C la capacité de l'électrode collectrice.

En considérant la figure 1, on obtient une expression de $\mathrm{d}y$ en fonction de $\mathrm{d}r$, qui permet d'effectuer l'intégration:

$$\mathrm{d}y = \frac{1}{\operatorname{tg}\theta}\cdot\frac{r\,\mathrm{d}r}{\sqrt{r^2 - r_0^2\sin^2\beta}}$$

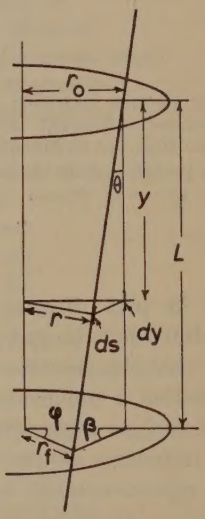

Fig. 1. Symboles employés dans la description d'une trajectoire oblique traversant la chambre d'ionisation.

Par l'étude de quelques cas particuliers, on peut déterminer sans ambiguité les signes à mettre devant les radicaux qui figurent dans la relation obtenue et après de nombreuses simplifications algébriques on parvient à l'expression suivante:

$$V = \frac{-e\lambda L}{C\cos\theta \ln b/a}\left\{\ln r_0/a - 1 + \right.$$
$$\left. + \frac{[(\gamma - \cos\varphi)\ln\gamma + \varphi(\sin\varphi)]\,\gamma}{\gamma^2 + 1 - 2\gamma\cos\varphi}\right\} \qquad (3)$$

où $\gamma = r_t/r_0$ et φ = angle entre r_0 et r_t.

Les impulsions les plus grandes seront dues à des trajectoires pour lesquelles $r_0 = r_t = b$; dans ces cas, $\gamma = 1$, $\varphi = 0$ et le troisième terme de (3) est égal à un, de sorte que $V_{\max} = -e\,\lambda\,L/C$.

La grandeur relative h d'une impulsion

quelconque, par rapport à celle d'une impulsion de grandeur maximum est donc

$$h = \frac{V}{V_{max}} = \frac{1}{\cos\theta \ln b/a} [\ln r_0/a - 1 + u(\gamma, \varphi)] \quad (4)$$

où

$$u(\gamma, \varphi) = \frac{[(\gamma - \cos\varphi) \ln\gamma + \varphi \sin\varphi]\gamma}{\gamma^2 + 1 - 2\gamma\cos\varphi} . \quad (5)$$

L'équation (4) signifie que, même si on suppose que toutes les particules produisent le même nombre d'électrons par unité de parcours dans la chambre, les impulsions qu'on observera ne seront pas toutes de même grandeur, puisque cette grandeur dépend du lieu de formation des ions dans la chambre. Par exemple, étant donné que les impulsions les plus grandes seront nécessairement dues à des trajectoires parallèles à l'axe et rasant la paroi du cylindre extérieur, les impulsions plus petites seront dues à des trajectoires obliques par rapport à l'axe et seront donc relativement plus nombreuses. En d'autres termes, la probabilité d'observer une impulsion de grandeur au moins égale à h varie en fonction de h. Cette probabilité peut être évaluée de la façon suivante.

3. Probabilité d'observer une Impulsion plus grande que h

Soit r_0 la distance à l'axe de la trajectoire verticale donnant une impulsion de grandeur h et considérons une autre trajectoire qui pénètre dans la chambre d'ionisation en un point E_1 situé à une distance r_0 de l'axe et qui en sort à une distance r_f de cet axe (cf. figure 2). Grâce à l'équation (4), nous pourrons trouver la courbe $r(\varphi)$ qui est le lieu des "points de sortie" des trajectoires qui, entrées par E_1, donnent lieu à des impulsions de même grandeur relative h que la trajectoire verticale. Toute trajectoire entrée par E_1, qui sortira par un point quelconque de S_2 (surface limitée par $r(\varphi)$ et le bord de la chambre) donnera des impulsions plus grandes que h. Il en sera de même de toute trajectoire qui, sortant de la chambre par un point de S_2, y aura pénétré par un point quelconque du segment E_1E_2. Or n'importe quel point de S_1 (surface limitée par un cercle de rayon r_0 et le bord de la chambre) peut être considéré comme faisant partie d'un segment E_1E_2, auquel correspond une surface S_2 symétriquement disposée sous ce segment.

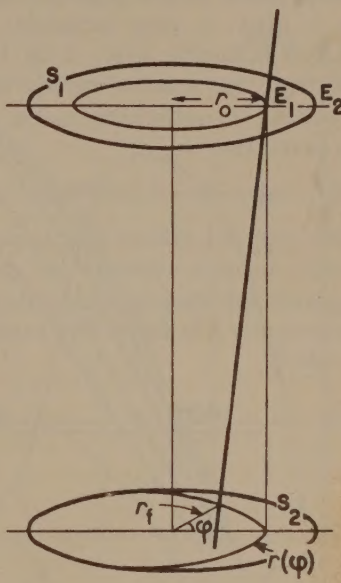

Fig. 2. Schéma servant au calcul de la probabilité d'observer une impulsion de grandeur relative supérieure à h.

Par conséquent, la probabilité d'observer une impulsion de grandeur au moins égale à h sera proportionnelle à S_1 et à l'angle solide $\omega(S_2)$ sous-tendu d'un point quelconque de E_1E_2 par la surface S_2; or, $S_1 = \pi b^2 (1 - r_0^2/b^2)$ et $\omega(S_2)$ pourra être calculé par l'approximation suivante: $\omega(S_2) \cong S_2/L^2$, si $L \gg 2b$. Dans ces conditions, on pourra donc écrire:

$$P(r_0/b) = \pi b^2 (1 - r_0^2/b^2) S_2/L^2 . \quad (6)$$

3.1. CALCUL DE $r(\varphi)$

Afin de trouver une expression analytique de la fonction $r(\varphi)$ qui est la limite intérieure de la surface S_2 et grâce à laquelle on pourra ensuite calculer l'aire de S_2, notons d'abord que d'après l'équation (4), toutes les trajectoires pour lesquelles $u(\gamma, \varphi) =$ constante, donneront des impulsions de même grandeur. On peut choisir cette constante à volonté, ce qui correspondrait dans chaque cas à une valeur différente de γ lorsque $\varphi = 0$. Nous choisirons $u(\gamma, \varphi) = 1$,

de sorte qu'une trajectoire pour laquelle φ est égal à zéro, est parallèle à l'axe de la chambre (i.e. $\gamma = 1$). On ne peut exprimer analytiquement γ en fonction de φ à partir de l'équation $u(\gamma, \varphi) = 1$, mais on peut facilement mettre en graphique la courbe $\gamma(\varphi)$, si on trace au voisinage de 1 les courbes de $u(\gamma, \varphi)$, pour diverses valeurs des paramètres γ et φ. On voit alors que la fonction

$$\gamma(\varphi) = 1 + 0.172\,\varphi^{2.36}$$

donne pour $\gamma(\varphi)$ des valeurs identiques (à 2% près) à celles qu'on a obtenues par graphique pour les mêmes valeurs de φ; c'est cette relation qui est représentée à la figure 3 et nous servira dans les calculs.

où φ_m est la valeur de φ pour laquelle $r = b$.

Après intégration,

$$S_2 = b^2 \times 2.105 \sqrt[2.36]{\frac{b}{r_0} - 1} \left\{ 1 - \frac{r_0^2}{b} \left[1 + 0.595 \left(\frac{b}{r_0} - 1 \right) + \right. \right.$$
$$\left. \left. + 0.175 \left(\frac{b}{r_0} - 1 \right)^2 \right] \right\} . \qquad (7)$$

(b) $r_0 < b/3.6$

Dans ce cas, l'aire de S_2 est donnée par la somme de deux termes: 1. une couronne circulaire comprise entre les rayons b et $3.6\ r_0$ et 2. l'aire comprise entre le cercle de rayon $3.6\ r_0$ et la courbe $r(\varphi)$:

$$S_2 = b^2 \left\{ \pi \left[1 - \left(\frac{r_0}{b} \right)^2 \cdot (3.6)^2 \right] + \left(\frac{r_0}{b} \right)^2 \cdot \left(\frac{3.6}{b} \right)^2 \cdot S'_2 \right\} \qquad (8)$$

où S'_2 désigne la valeur de S_2 lorsque $r_0 = b/3.6$.

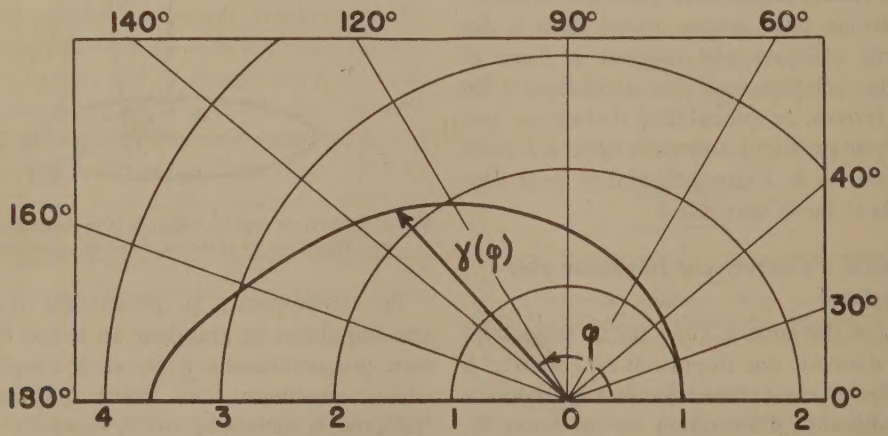

Fig. 3. Graphique de la fonction $\gamma(\varphi)$.

Une fois trouvé $\gamma(\varphi)$, il est facile de trouver $r(\varphi)$, puisque l'après la définition de γ,

$$r(\varphi) = r_0\,\gamma(\varphi) .$$

3.2. CALCUL DE S_2

Pour le calcul de S_2, il faut distinguer deux cas, selon que r_0 est supérieur ou inférieur à $b/3.6$, car $b/3.6$ est la valeur de r pour laquelle φ atteint sa valeur limite de 180°.

(a) $r_0 > b/3.6$

Dans ce cas, l'aire de S_2 sera donnée directement par

$$S_2 = 2 \int_r^b \int_0^{\varphi_m} r\,dr\,d\varphi$$

3.3 MISE EN GRAPHIQUE DE $P(r_0/b)$

La fonction $P(r_0/b)$ est donc maintenant entièrement déterminée par les équations (6) et (7) ou (8). On peut la mettre en graphique en fonction de h grâce à l'équation (4) qui donne la relation entre h et r_0/b. Elle est représentée à la figure 4 pour diverses valeurs de b/a. Dans cette figure, on voit aussi la courbe $P'(h) = dP/dh$ pour $b/a = 750$, qui a été utilisée dans l'exemple suivant.

4. Exemple

Une chambre d'ionisation cylindrique dont la cathode a un rayon intérieur de 3.81 cm et

l'anode un rayon de 0.0051 cm ($b/a = 750$), est remplie d'argon purifié à 3.90 atm (0° C) et disposée verticalement. La longueur L du volume sensible est de 45.0 cm. Un système approprié

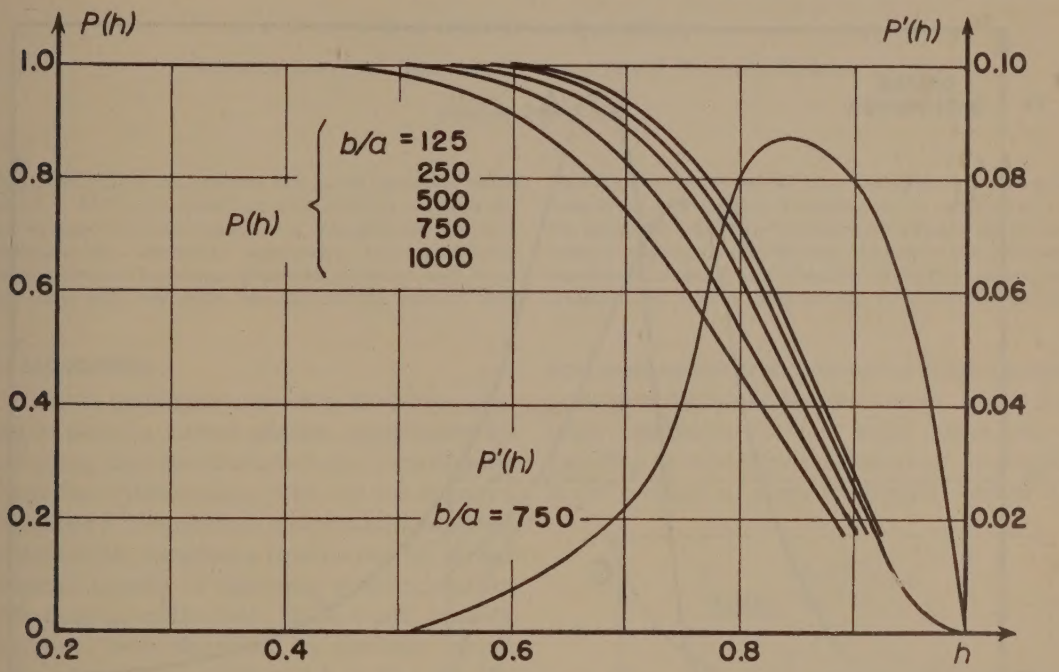

Fig. 4. $P(h)$: Probabilité d'observer une impulsion de grandeur relative supérieure à h, pour diverses valeurs de b/a. $P'(h) = \mathrm{d}P/\mathrm{d}h$ pour $b/a = 750$; courbe obtenu à partir de $P(h)$ et normalisée de sorte que son intégrale soit égale à 1.

de compteurs et d'absorbants de plomb permet de photographier sur l'écran d'un oscilloscope à rayons cathodiques les impulsions dues aux mésons mu de la radiation cosmique, dont l'énergie est voisine de celle qui correspond au minimum d'ionisation, et qui traversent la chambre dans toute sa longueur.

Dans ces conditions, il y aura proportionnalité exacte entre la perte d'énergie Δ subie par le méson et le nombre de paires d'ions produits dans le gaz. Si la grandeur des impulsions enregistrées par l'appareil n'était fonction que de ce nombre de paires d'ions, une perte d'énergie Δ_L donnerait toujours lieu à des impulsions de même grandeur V_L. Par conséquent, à la distribution statistique des pertes d'énergie que prévoit la théorie de Landau[3]) correspondrait une distribution proportionnelle de la grandeur des impulsions (courbe A, figure 5).

A cause de l'effet étudié dans cet article, cependant, à la distribution statistique de la grandeur des impulsions décrite ci-dessus vient se superposer une autre distribution: n_L mésons qui subissent une même perte d'énergie Δ_L donnent des impulsions de grandeur V, variable selon la position de la trajectoire dans la chambre; en d'autres termes, chaque ordonnée de la courbe A donne lieu à une distribution (courbe C, figure 5), définie par la courbe $P'(h)$ de la figure 4 (ici, $h = V/V_L$), les ordonnées étant multipliées par un facteur $k(V_L)$, de sorte que $\int_0^1 k(V_L)\, P'(h)\, \mathrm{d}h = n_L$. Une fois tracées plusieurs courbes $k(V_L) \cdot P'(h)$ de ce genre pour différentes valeurs de V_L, on effectue graphiquement les intégrales du type $\int_0^\infty k(V_L) P'(h)\, \mathrm{d}V_L$; chacune d'elles donne un point de la distribution nouvelle. Celle-ci est représentée par la courbe B de la figure 5.

[3]) L. Landau, J. Phys. (USSR) 8 (1944) 201.

D'après la théorie de Landau, les impulsions de grandeur V_{0L} correspondraient à une perte d'énergie (perte la plus probable) de 350 keV dans les conditions de cette expérience. En Landau, la largeur (à la demi-hauteur) de la courbe de distribution devrait être dans cet exemple de 27%, alors que la largeur de la courbe B est de 38%.

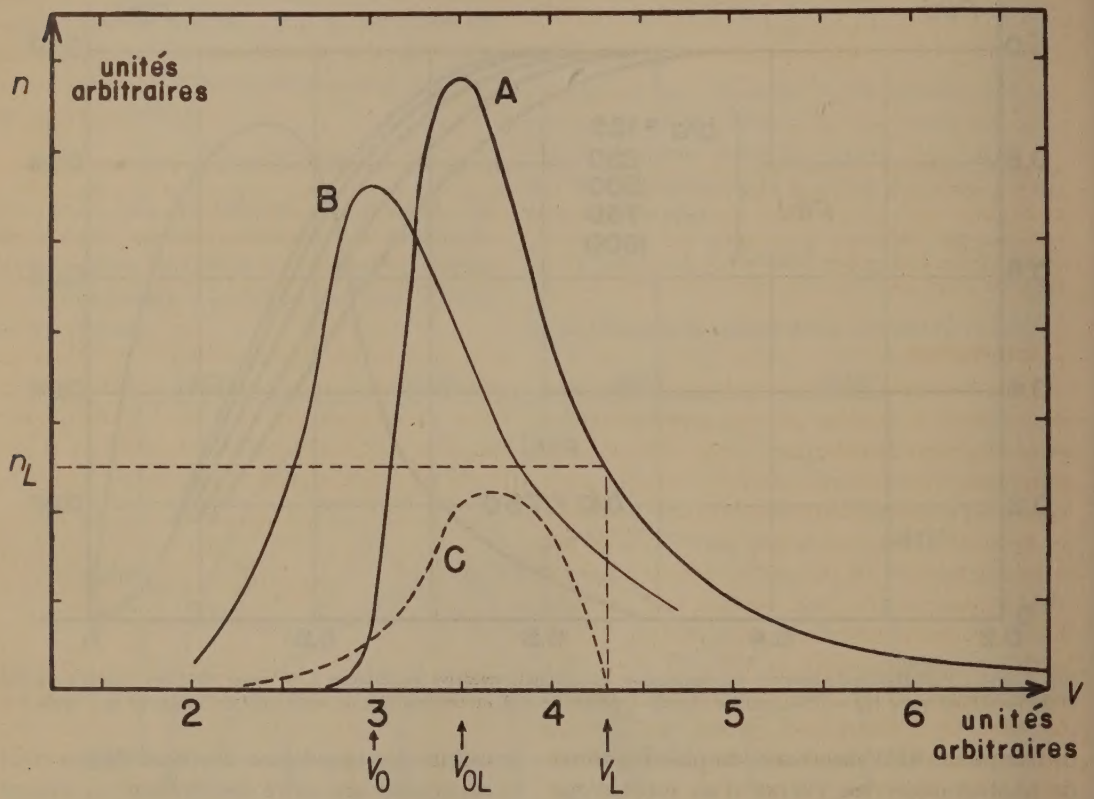

Fig. 5. A: courbe différentielle théorique de distribution des impulsions en fonction de leur grandeur V. Cette courbe est proportionnelle à une courbe de Landau pour laquelle, dans l'exemple étudié ici, à chaque unité de V correspondrait une perte d'énergie de 100 keV. B: courbe différentielle de distribution des impulsions en fonction de leur grandeur V, obtenue à partir de la courbe A en tenant compte de l'effet de la collection des électrons dans la chambre d'ionisation décrite dans le texte. C: courbe différentielle de distribution (échelle verticale multipliée par 10) des n_L trajectoires qui, en l'absence de l'effet de collection des électrons auraient toutes donné lieu à des impulsions de grandeur V_L.

supposant une proportionnalité exacte entre les grandeurs V et les pertes d'énergie Δ, on voit que le maximum de la courbe se trouvant à V_0, la perte la plus probable semblera être, expérimentalement, de 300 keV seulement.

Une autre conséquence évidente de l'effet de la collection des électrons est l'élargissement de la courbe de distribution; d'après la théorie de

Remerciements

L'auteur remercie l'Université Laval et le Conseil canadien pour la défense qui ont contribué fianancièrement à la poursuite du travail dont cette étude fait partie. Il remercie également monsieur le professeur Fernand Bonenfant qui a revisé le manuscrit.

NUCLEAR INSTRUMENTS 3 (1958) 127–132; NORTH-HOLLAND PUBLISHING CO. – AMSTERDAM

NOTES ON A FAST TIME-TO-AMPLITUDE CONVERTER

R. E. GREEN† and R. E. BELL

Radiation Laboratory, Department of Physics, McGill University, Montreal

Received 2 May 1958

A time-to-amplitude converter with a full resolution width of 8.5×10^{-10} sec is described. The circuit is based on the 6BN6 gated beam tube operated at unusually low electrode voltages. An additional supervisory fast coincidence circuit ensures that output pulses are produced only when the pulse delay lies within the desired time interval, thus avoiding the double-valued time-to-amplitude conversion inherent in such systems. Examples of the performance of the apparatus are shown for prompt coincidences and for the delayed coincidence distribution observed when positrons annihilate in fused quartz. The time-to-amplitude converter is easily added to an existing fast-slow coincidence assembly.

1. Introduction

Time-to-amplitude converters have been used many times in nuclear physics experiments for recording time distributions in the form of pulse amplitude distributions. With the aid of such a converter a conventional multichannel analyzer, or kicksorter, becomes a time-sorter. We do not attempt to refer to the many circuits used for this purpose in the past. Neilson and James[1]), however, have described an excellent circuit with a resolution width of 1.5×10^{-9} sec. We have independently developed a system similar to that of Neilson and James, but having advantages that lead to an improved performance. This converter has been in use for several years in this Laboratory.

The circuit employs the type 6BN6 gated beam tube having two control grids, g_1 and g_3, each of which is biased so as just to cut off the anode current. Positive pulses of fixed duration from two counters are applied respectively to the two grids in such a way that a constant anode current flows during the time interval in which the two pulses overlap. The integrated anode pulse is proportional to this overlap time and is therefore linearly related to the delay time between the two counter pulses. This system gives zero pulse output for zero overlap, i.e. for a single pulse, and thus has a distinct advantage over some earlier arrangements in which a single pulse gave the largest possible output. Under the latter conditions the few small pulses corresponding to coincidence events must be sought in the presence of many large pulses caused by

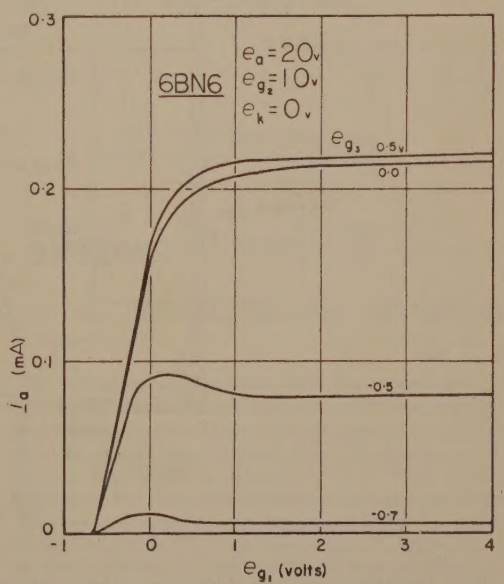

Fig. 1. Characteristic curves of the type 6BN6 tube operated at low electrode voltages ($e_a = 20$V, $e_{g_2} = 10$V). Anode current limiting is produced when both g_1 and g_3 are driven 1 volt positive from cutoff, but neither grid alone can cause anode current to flow.

† Now at Atomic Energy of Canada, Ltd., Chalk River, Ontario, Canada.

[1]) G. C. Neilson and D. B. James, Rev. Sci. Instr. 26 (1955) 1018.

one of the single counting rates. The circuit to be outlined here has the following further advantages.

1.1. OPERATION OF THE 6BN6 AT LOW ELECTRODE VOLTAGES

The 6BN6 tube has the feature that as its grids are driven positive from cutoff, the anode current increases towards a limiting value that is nearly independent of further positive excursions of the grids. Thus small residual inequalities in the supposedly uniform pulses used to drive the grids are unimportant, provided only that these pulses are large enough. When the tube is operated at the normal electrode voltages suggested in the receiving tube manual ($e_a = e_{g2} = 60$ volts), the grid voltage swing required to go from cutoff to full anode current limiting is about 5 volts. If, however, the operating voltages on the 6BN6 are reduced to $e_a = 20$ volts, $e_{g2} = 10$ volts, the characteristic curves of fig. 1 are obtained.

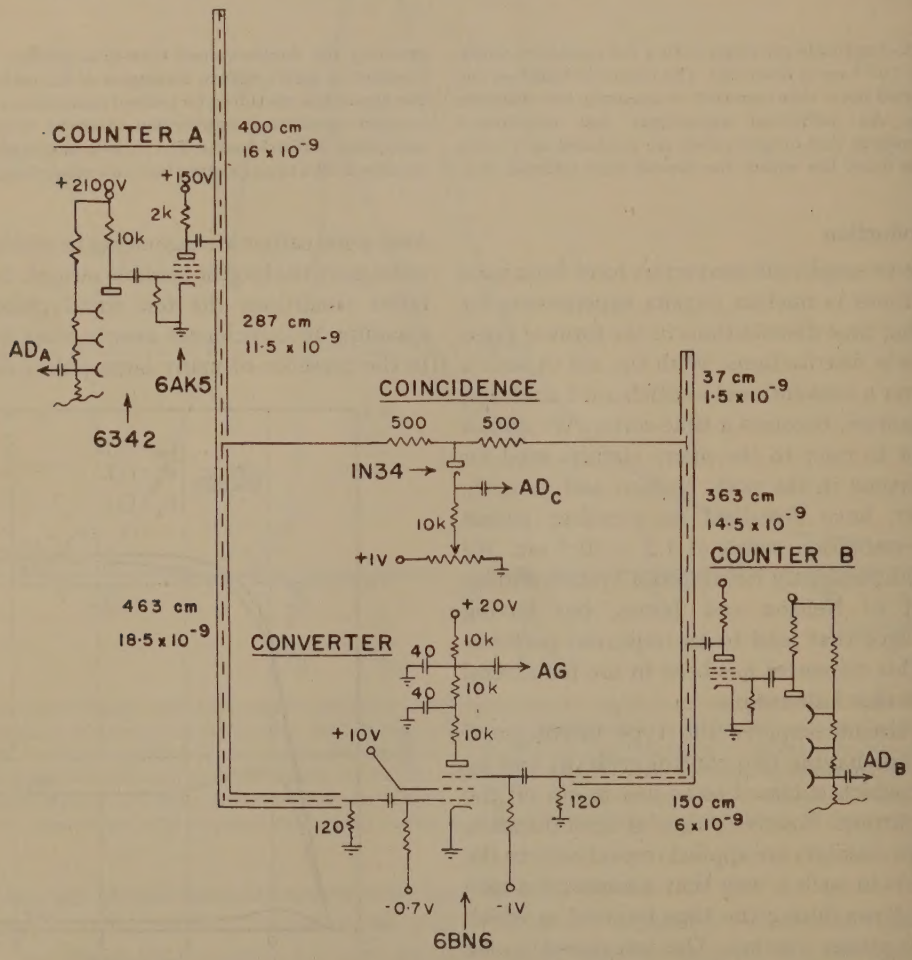

Fig. 2. Diagram of the part of the circuit concerned with the fast pulses. The two 6342 photomultipliers are shown only in part. The fast coincidence circuit appears at the centre of the diagram, and the 6BN6 converter at the bottom. The lengths of the cables are given in centimetres, and the number below each length marked on the diagram is the one-way transit time of that section of cable in seconds.

Here we see that a positive pulse of 1 volt on both grids will drive the tube from cutoff to its anode current limit. In the present apparatus this pulse is provided by using the anode pulses of a type 6342 photomultiplier operated at 2100 volts to cut off a standing anode current of 16 mA in a pentode (6AK5). The anode load of this pentode is a branched 125 ohm standard coaxial cable (RG63/U), one section of which leads to the appropriate 6BN6 grid. The effective anode impedance of the pentode is 62.5 ohms, and the anode pulse is therefore equal to 1 volt.

It is clearly easier to provide a fast 1 volt driving pulse than one five times as large, no matter what the source of pulses may be. Neilson and James[1]), for example, use the same photomultiplier (type 6342) to cut off a standing current of 15 mA in a secondary emission pentode whose anode load is a section of special 330 ohm delay cable. The resulting 5 volt pulse is conducted to their 6BN6 converter through a cathode follower and a length of standard 90 ohm coaxial cable. Other workers have used distributed amplifiers to raise the photomultiplier pulses to the required level. These expedients are effective, but they inevitably involve some loss of pulse speed, as well as extra circuit complications.

1.2. AVOIDANCE OF DOUBLE VALUES OF THE DELAY

In any system that measures a delay by the degree of overlap of two pulses, there are in fact two values of the delay that yield the same degree of overlap and hence the same size of output pulse. The main bad effect is to cause the chance coincidence rate in any channel of the time-sorter to be double the rate expected from the width of the channel and the single counting rates. The present circuit avoids this difficulty by adding a supervisory fast coincidence circuit to the assembly, whose output vanishes unless the delay lies within the desired time interval; the output of this circuit gates the output of the 6BN6 converter.

2. Circuit Details

The arrangement of the fast pulse part of the converter is shown in fig. 2. Two scintillation counters, A and B, are shown with their anodes connected to the grids of the equalizing pentodes. The arrangement shown is intended to measure the delay of counter B pulses relative to those of counter A over the range from 0 to 25×10^{-9} sec. The cables are all RG63/U, 125 ohms, velocity of propagation $0.84c$, and the lengths in centimeters are marked on each section. Since counter A is connected to g_1 of the 6BN6, and since the transit time of electrons

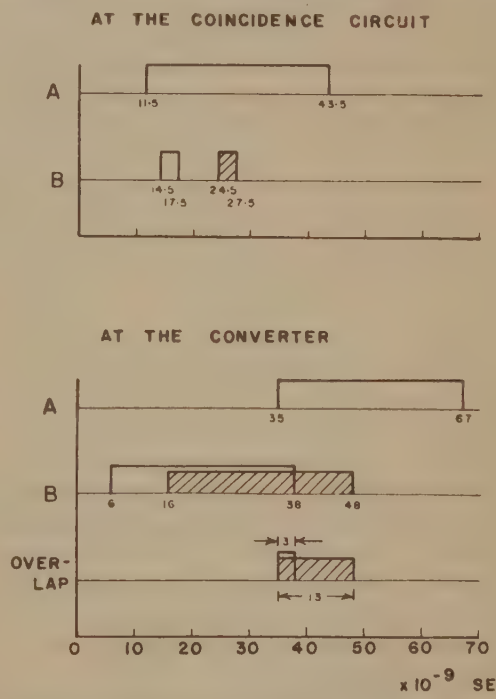

Fig. 3. Time sequence of the pulses from counters A and B at the coincidence circuit (upper part of diagram) and at the 6BN6 converter (lower part of dagram). The abscissa scale represents time elapsed since the appearance of the pulse at the anode of counter A, in 10^{-9} sec units. For counter B, the open pulses represent an event simultaneous wit that in counter A, and the shaded pulses represent an event delayed by 10×10^{-9} sec relative to that in counter A. The exact times of beginning and ending of each pulse are shown by numbers at the foot of the pulse. The finite rise times of the pulses have been ignored. The degree of overlap of the pulses at the converter is shown in the bottom line of the dagram.

from g_1 to g_3 is about 5×10^{-9} sec at these operating voltages, there is an "invisible delay" of 5×10^{-9} sec in series with the pulses from counter A. The time sequences of the pulses at the coincidence circuit and at the converter are shown in fig. 3, where this invisible delay is included. All the pulses are positive, 1 volt in amplitude. Two sets of pulses are shown for counter B, one set corresponding to a prompt event (open pulses) and one to an event delayed by 10×10^{-9} sec (shaded pulses). We see that if the coincidence circuit will detect any B pulse that overlaps the A pulse by more than half its own width, it will give an output for any B pulse delay relative to the A pulse lying between $-(4.5 \times 10^{-9})$ and $+(27.5 \times 10^{-9})$ sec. The position of the B pulse at the converter, corresponding to the limiting delay of 27.5×10^{-9} sec, is such that the pulses at the converter are almost completely overlapping.

Returning to fig. 2, the supervisory coincidence circuit is a simple diode arrangement like that of Bell, Graham, and Petch[2]), with the addition of 500 ohm isolating resistors to reduce reflections on the two transmission lines and cross-coupling between them. The output of the coincidence diode is taken to an amplifier and discriminator AD_C. The two photomultipliers A and B also have slow outputs from their eighth dynodes to amplifiers and discriminators AD_A and AD_B. The outputs from these units are used for pulse height selection by the fast-slow system shown later.

At the 6BN6 time-to-amplitude converter the overlapping input pulses are integrated in the anode circuit, which consists of three resistors and two condensers. This arrangement was adopted in order to minimize capacity transmission to the anode circuit of the B pulses on g_3. The effective integrating time constant of this circuit is about 0.5 μsec, or 20 times as long as the longest delay to be measured. The output of the converter circuit is taken to an amplifier and gate circuit AG. The cables in fig. 2 are assembled by clamping and soldering, so as to avoid the extra capacity of standard coaxial connectors.

Fig. 4 is a block diagram of the whole apparatus showing the connections between the various units, but not attempting to show the delays involved. This circuit ensures that a pulse will enter the kicksorter for registration of its equivalent delay only if the corresponding pulses in counters A and B both lie within the desired range of amplitude and if the relative delay of the pulses from A and B lies within the desired interval. The units AD_A and AD_B may of course contain differential discriminators if desired. Fig. 4 omits the ratemeters and recording milliammeters that monitor the single counting rates of A and B and the triple coincidence rate.

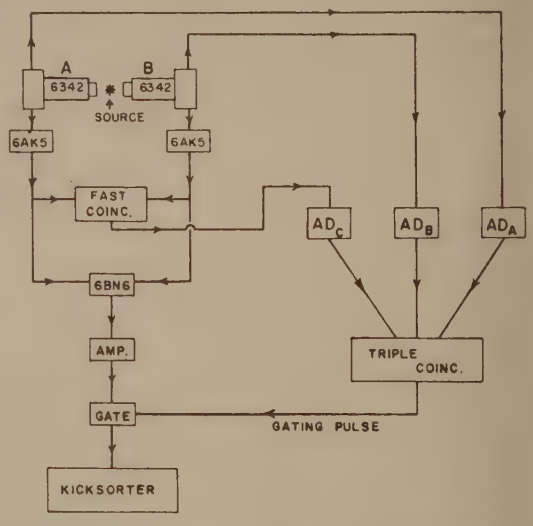

Fig. 4. Simplified block diagram of the whole time-to-amplitude assembly. It consists of a conventional fast-slow coincidence apparatus plus the units 6BN6, AMP., GATE, KICKSORTER.

The scale of the kicksorter is calibrated in terms of time by placing a source of prompt coincidences between the counters, and observing the movement of the centre of the prompt coincidence peak along the scale as the cable marked 150 cm in fig. 2 is varied in length by known amounts. The calibration curve obtained in this way is linear for pulse overlap times greater than 2×10^{-9} sec; for smaller overlap

[2]) R. E. Bell, R. L. Graham and H. E. Petch, Can. J. Phys. **30** (1952) 35.

times the calibration shows a curvature owing to the finite rise times of the pulses. As shown by fig. 3, the converter is operated with prompt pulses overlapping by 3×10^{-9} sec, and delayed pulses by a larger amount, so that the short non-linear section of the calibration curve is avoided.

provided that a multi-channel analyzer is available.

3. Performance

The converter assembly can be used to advantage for any purpose where a conventional fast delayed coincidence apparatus is used. In

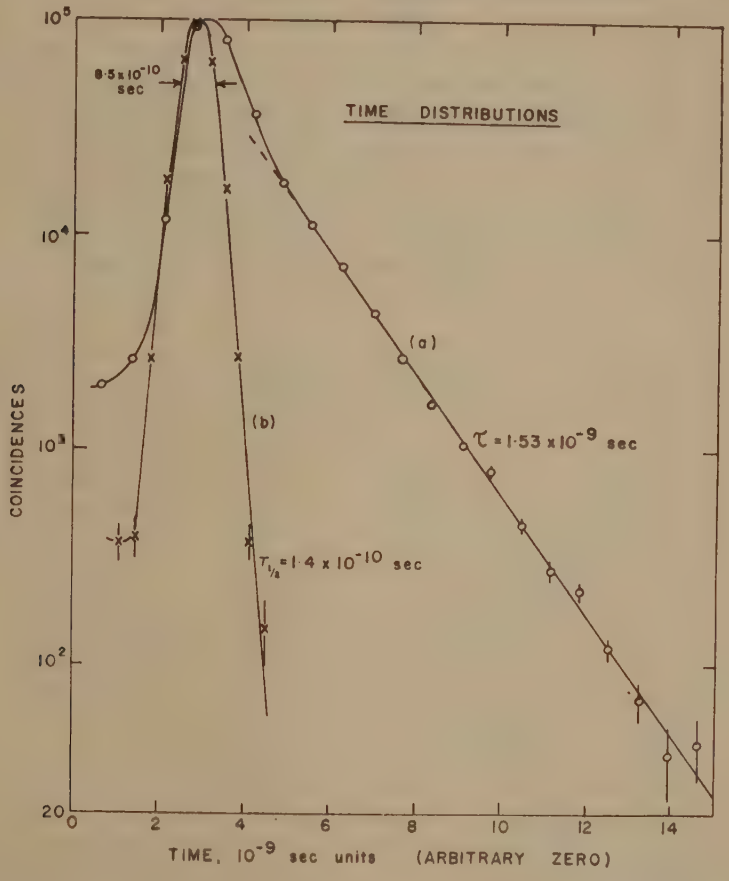

Fig. 5. Curve (a), time distribution of positron annihilations in fused quartz, observed with the time-to-amplitude converter. Curve (b), time resolution observed for prompt gamma-gamma coincidences from a Co^{60} source, the biases on the two counters being approximately the same as for curve (a). Curve (b) should not be interpreted as furnishing an accurate zero of time for curve (a), since the two curves were recorded some days apart and on different kicksorter scales.

Figs. 2 and 4 show that most of the components of this circuit are similar to those of the fast-slow coincidence circuit of Bell, Graham and Petch[2]). Laboratories possessing such a circuit can add the converter circuit to their present assembly with relatively little trouble, this laboratory it has so far been used mainly for measuring delay distributions of positron annihilations in condensed materials. Curves illustrating its performance are shown in fig. 5 In each of these curves the number of counts recorded in a given channel is plotted on a

logarithmic scale as a function of the equivalent delay time found from the cable calibration. The kicksorter used to record the results is a 28-channel machine designed and built in this laboratory (Skarsgard and Bell unpublished). For the positron lifetime measurements, a source of about 10 μC of Na^{22} is sandwiched or embedded in the sample being tested, and this assembly is placed between the counters. Counter A is integrally biased to accept only the upper part of the Compton pulse distribution of the 1.28 MeV nuclear gamma ray, and counter B is differentially biased to accept the upper half of the Compton pulse distribution of the 0.51 MeV annihilation quanta. These arrangements have been standard for positron lifetime measurements ever since the early work of Shearer and Deutsch[3]). Both counters used diphenylacetylene phosphors.

Curve (a) of fig. 5 shows the delay distribution for positrons annihilating in a sample of "Vitreosil" fused quartz ($> 99.8\%$ SiO_2). It shows a short-lived peak and a very prominent long-lived component whose decay is followed over three decades without any sign of departure from an exponential shape. The adherence of the curve to the expected exponential shape is further evidence of the linearity of the instrument. Curve (a), containing over 200 000 counts, was recorded in about two hours. An analysis of this curve gives a lifetime, τ_2, of $(1.53 \pm 0.05) \times 10^{-9}$ sec and an intensity, I_2, of $(53 \pm 8)\%$ for the long-lived component. These results are quite different from those given by Bell and Graham[4]) for a different sample of "fused quartz". We have taken up this question in more detail in another publication[5]).

Curve (b) of fig. 5 is a prompt coincidence curve made with a source of Co^{60} in place of the Na^{22}, with the counters biased roughly the same as in the positron experiment. This curve shows a full width at half maximum of 8.5×10^{-10} sec and a slope on its right hand side corresponding to a half life of 1.4×10^{-10} sec. Some improvement in this curve could be expected if both counters, instead of only counter A, were biased to accept the higher energy pulses from the Co^{60} gamma ray. A further improvement might be realized if the 6AK5 limiting pentodes at the counters were replaced by higher performance tubes, such as the E-2133 secondary emission tube used by Neilson and James[1]) or a high performance pentode like the WE-404A. Nevertheless the curve of fig. 5 (b) is at least equal in resolution to results obtained with conventional delayed coincidence equipment.

Both curves (a) and (b) of fig. 5 show a few small spurious pulses to the left of the main peak. The same effect is seen in the prompt curve of Neilson and James. No serious attempt has been made to trace these pulses to their source, since they neither distort the right hand part of the curve where long lifetime measurements are made, nor shift the position of the centroid of the curve, nor appreciably falsify the total area under the curve. They are probably due to pile-up effects, since their relative number decreases at low counting rates.

It is interesting to reflect that the kicksorter used with such an instrument as that described here could easily be of the Wilkinson[6]) or Hutchinson-Scarrott[7]) types. In that case the original time distribution on the 10^{-9} sec scale would be converted into a pulse amplitude distribution, amplified, and applied to the kicksorter; here it would be converted to time on a 10^{-5} sec scale or longer, in the well known manner of such kicksorters, and registered as a distribution that is interpreted as an amplitude spectrum; finally this pulse amplitude distribution would be re-converted to a time distribution on the 10^{-9} sec scale by means of a calibration factor.

[3]) J. W. Shearer and M. Deutsch, Phys. Rev. **76** (1949) 462.

[4]) R. E. Bell and R. L. Graham, Phys. Rev. **90** (1953) 644.

[5]) R. E. Green and R. E. Bell, Can. J. Phys. **35** (1957) 398.

[6]) D. H. Wilkinson, Proc. Camb. Phil. Soc. **46** (1949) 508.

[7]) G. W. Hutchinson and G. G. Scarrott, Phil. Mag. **42** (1951) 792.

NUCLEAR INSTRUMENTS 3 (1958) 133–148; NORTH-HOLLAND PUBLISHING CO. – AMSTERDAM

MASSENSPEKTROGRAPHEN MIT KORRIGIERTEN BILDFEHLERN

L. A. KÖNIG und H. HINTENBERGER

Max-Planck-Institut für Chemie, Mainz

Received 2 May 1958

The general expressions derived in a previous paper[1]) for second-order angle aberration, angle-velocity aberration, and velocity aberration of mass spectrometers consisting of a radial electric field and a homogeneous magnetic sector field in series, are developed for the special case of mass spectrographs with double focusing of the first order for all masses along a straight image curve. The possibilities for correcting these image defects are investigated. Tables are presented of solutions for apparatus types in which at one point of the image curve all three or two of the image defects simultaneously vanish. Almost each apparatus with simultaneous correction of the three image defects possesses a large radial field. On the other hand there are useful solutions according to which either the two image defects depending on aperture or the two depending on velocity vanish.

The numerical calculations were carried out by means of an IBM-magnetic-drum-computer, type 650. The computation procedure is outlined briefly.

1. Einleitung

Bei einem Massenspektrometer, das aus einem elektrischen Radialfeld und einem dahintergeschalteten homogenen magnetischen Sektorfeld zusammengesetzt ist, wird in der Regel mit einem einzigen Auffänger gemessen, der hinter dem Austrittschlitz des Instruments angebracht ist. Verschiedene Massen werden dann durch Veränderung des magnetischen Ablenkfeldes nacheinander auf den Auffänger gebracht. Es genügt daher, dass jeweils für die eine gerade beobachtete Masse optimale Fokussierungsbedingungen erreicht werden. Für Instrumente dieser Art haben wir aus früher angegebenen allgemeinen Gleichungen über die Bildfehler in Massenspektrometern und Massenspektrographen[1]) die Bedingungen dafür angegeben, dass die vom Öffnungswinkel α und der relativen Geschwindigkeitsabweichung $\beta = \Delta v/v_0$ der Ionen quadratisch abhängenden Bildfehler (Glieder mit α^2, $\alpha\beta$ und β^2) korrigiert werden. Es konnten dabei die Abmessungen für eine grosse Zahl von Massenspektrometern angegeben werden, die vollständige Doppelfokussierung zweiter Ordnung aufweisen[2,3]).

Für Massenspektrographen ist es vorteilhaft, wenn möglichst viele Massen gleichzeitig entlang einer geraden Photoplatte fokussiert werden. Wie Mattauch und Herzog[4]) bereits 1934 gezeigt haben, kann Doppelfokussierung erster Ordnung entlang einer geraden Photoplatte für alle Massen gleichzeitig erreicht werden, wenn zwischen den Ablenkwinkeln φ_e und φ_m und dem Eintrittswinkel ins Magnetfeld ε' die von ihnen angegebene Doppelfokussierungsbedingung erfüllt wird und die Verlängerung der Photoplatte durch den Eintrittspunkt des Mittelstrahls ins Magnetfeld geht. Die Gleichungen für die Korrektur der Bildfehler für Apparate dieser Art haben wir, soweit geradlinig begrenzte Magnetfelder verwendet werden, bereits in einer früheren Arbeit abgeleitet[5]) und eine Reihe von Apparaten mit korrigierten Bildfehlern angegeben[5,6]). Insbesondere wurde gezeigt, dass für ein bestimmtes Verhältnis der Bahnradien im elektrischen und magnetischen Feld, also für eine bestimmte Masse, der

[1]) H. Hintenberger und L. A. König, Zs. Naturf. **12a** (1957) 140.

[2]) H. Hintenberger und L. A. König, Zs. Naturf. **12a** (1957) 773.

[3]) H. Hintenberger und L. A. König, Zs. Naturf. **13a** (1958) 236.

[4]) J. Mattauch und R. Herzog, Zs. f. Phys. **89** (1934) 786.

[5]) H. Hintenberger, H. Wende und L. A. König, Zs. Naturf. **10a** (1955) 605; siehe auch Berichtigung: Zs. Naturf. **12a** (1957) 88.

[6]) H. Hintenberger, H. Wende und L. A. König, Zs. Naturf. **10a** (1955) 344.

Öffnungsfehler in einem Apparat vom Mattauch-Herzogschen Typ verschwindet[6]). In der Zwischenzeit ist auch von Robinson[7]) gezeigt worden, dass in einem Mattauch-Herzogschen Massenspektrographen durch eine geeignete Krümmung der Grenze des Magnetfeldes auf der Einschussseite die von $\alpha\beta$ und β^2 abhängigen Bildfehler an einer Stelle der Photoplatte gleichzeitig korrigiert werden können. Ferner haben Liebl und Ewald[8]) Massenspektrographen, die aus einem Toroidkondensator mit einem dahintergeschalteten homogenen Magnetfeld mit gekrümmter Einschussgrenze bestehen, untersucht und gefunden, dass in diesen Apparaten bei stigmatischer Abbildung eine Korrektur der von α^2 und von $\alpha\beta$ abhängigen Bildfehler an einer Stelle der Photoplatte möglich ist.

In der vorliegenden Arbeit werden aus unseren früher angegebenen allgemeinen Formeln für die Bildfehler und ihre Korrektur in Massenspektrometern und Massenspektrographen[1,2]) die Korrekturbedingungen für die von α^2, $\alpha\beta$ und β^2 abhängigen Bildfehler in Massenspektrographen, die Doppelfokussierung erster Ordnung für alle Massen zeigen, abgeleitet, wobei auch eine gekrümmte Begrenzung des Magnetfeldes auf der Einschussseite zugelassen wird. Mit Hilfe einer elektronischen Rechenmaschine wurde systematisch nach vorhandenen Lösungen der Korrekturgleichungen gesucht. Dabei wurde auch der Bereich $\pi < \sqrt{2}\,\varphi_e \leqq \frac{3}{2}\pi$, den wir in unseren früheren Arbeiten als für den praktischen Bau von Apparaten zu ungünstig stets ausgeschlossen hatten, mitbehandelt. Es zeigte sich nämlich, dass gerade in diesem Bereich viele Lösungen der Korrekturgleichungen liegen. Das Ergebnis gestattet durch seine Vollständigkeit, die Möglichkeiten zur Korrektur der Bildfehler zu überblicken. Es gibt Lösungen für Massenspektrographen, bei denen die drei von α und β abhängigen Bildfehler zweiter Ordnung an einer Stelle der Photoplatte gleichzeitig verschwinden, doch sind die Abmessungen der Radialfelder dieser Apparate in der Regel ziemlich gross. Bei Beschränkung auf die gleichzeitige Korrektur von nur zwei Bildfehlern wurden dagegen viele bisher unbekannte Lösungen für Apparate mit günstigen Abmessungen gefunden.

[7]) Ch. F. Robinson, Rev. Sci. Instr. **28** (1957) 777.
[8]) H. Liebl und H. Ewald, Zs. Naturf. **12a** (1957) 538, 541.

2. Die Korrekturgleichungen für die Bildfehler

Die Korrekturgleichungen für die Bildfehler können auf zwei voneinander unabhängigen Wegen abgeleitet werden[1,3,5]). Wir machen von beiden Ableitungen Gebrauch, um eine wirksame Rechenkontrolle zu erreichen.

2.1. ERSTE METHODE

Die erste Methode geht von der Berechnung der Bildfehler aus. Nullsetzen der Ausdrücke für die Bildfehler ergibt die Korrekturgleichungen. Die Bildfehler selbst wurden bereits früher berechnet[1]), indem der Mittelstrahl s_0 und ein Nebenstrahl s_1 eines Strahlenbündels beim Durchgang durch ein elektrisches Ablenkfeld und ein dahintergeschaltetes magnetisches Sektorfeld verfolgt wurden. Hierbei war vorausgesetzt, dass der Nebenstrahl nach Durchlaufen des elektrischen Feldes sich in der Form darstellen lässt:

$$y_e = r_e\,[K_1\alpha_e + K_2\beta + K_{11}\alpha_e^2 + K_{12}\alpha_e\beta + K_{22}\beta^2] + x_e\,[L_1\alpha_e + L_2\beta + L_{11}\alpha_e^2 + L_{12}\alpha_e\beta + L_{22}\beta^2]\,. \tag{1}$$

Die Grössen K und L sind Abkürzungen der folgenden Form:

$$\left.\begin{aligned} K_1 &= \varkappa_{1a} + \varkappa_{1b}\frac{l'_e}{r_e}\,,\\ K_2 &= \varkappa_{2a}\,,\\ K_{11} &= \varkappa_{11a} + \varkappa_{11b}\frac{l'_e}{r_e} + \varkappa_{11c}\left(\frac{l'_e}{r_e}\right)^2\,,\\ K_{12} &= \varkappa_{12a} + \varkappa_{12b}\frac{l'_e}{r_e}\,,\\ K_{22} &= \varkappa_{22a}\,; \end{aligned}\right\} \tag{2}$$

$$\left.\begin{aligned} L_1 &= \lambda_{1a} + \lambda_{1b}\frac{l'_e}{r_e}\,,\\ L_2 &= \lambda_{2a}\,,\\ L_{11} &= \lambda_{11a} + \lambda_{11b}\frac{l'_e}{r_e} + \lambda_{11c}\left(\frac{l'_e}{r_e}\right)^2\,,\\ L_{12} &= \lambda_{12a} + \lambda_{12b}\frac{l'_e}{r_e}\,,\\ L_{22} &= \lambda_{22a}\,, \end{aligned}\right\} \tag{3}$$

wobei die Grössen $\varkappa$ und λ von der Art und den Dimensionen des elektrischen Feldes abhängen. Für den Fall eines elektrischen Zylinder-

kondensators werden diese Grössen später als Gln. (11) und (12) im Detail angegeben. Koordinatensystem und Bezeichnungen sind in Abb. 1 erklärt.

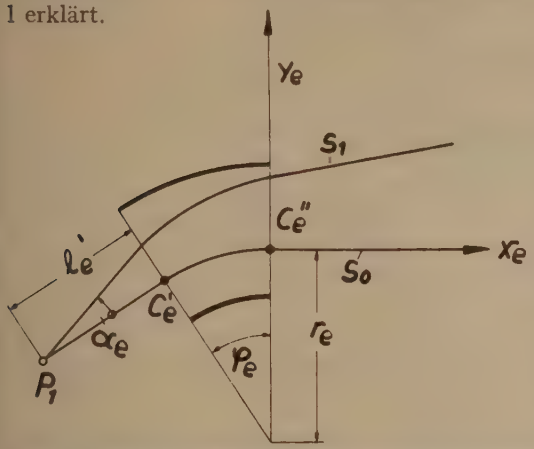

Abb. 1. Koordinatensystem zur Bahnberechnung des aus dem Zylinderkondensator austretenden Ionenstrahls (s_0 = Mittelbahn, die von Teilchen der Geschwindigkeit $v = v_0$ mit $\alpha_e = 0$ durchlaufen wird; s_1 = Nachbarbahn von Teilchen mit $v = v_0(1+\beta)$ und $\alpha_e \neq 0$).

Eine analoge Voraussetzung wurde für den aus dem Magnetfeld austretenden Nebenstrahl gemacht:

$$y_m = r_m[M_1\alpha_m + M_2\beta + M_{11}\alpha_m^2 + M_{12}\alpha_m\beta + M_{22}\beta^2] + x_m[N_1\alpha_m + N_2\beta + N_{11}\alpha_m^2 + N_{12}\alpha_m\beta + N_{22}\beta^2]. \quad (4)$$

Koordinatensystem und Bezeichnungen sind in Abb. 2 erklärt. Die Grössen M und N lassen sich in analoger Weise wie die Grössen K, L zerlegen, was aus den Potenzreihenansätzen für y_e bzw. y_m folgt. Es ist also:

$$\left.\begin{aligned} M_1 &= \mu_{1a} + \mu_{1b}\frac{l'_m}{r_m}, \\ M_2 &= \mu_{2a}, \\ M_{11} &= \mu_{11a} + \mu_{11b}\frac{l'_m}{r_m} + \mu_{11c}\left(\frac{l'_m}{r_m}\right)^2, \\ M_{12} &= \mu_{12a} + \mu_{12b}\frac{l'_m}{r_m}, \\ M_{22} &= \mu_{22a}; \end{aligned}\right\} \quad (5)$$

$$\left.\begin{aligned} N_1 &= \nu_{1a} + \nu_{1b}\frac{l'_m}{r_m}, \\ N_2 &= \nu_{2a}, \\ N_{11} &= \nu_{11a} + \nu_{11b}\frac{l'_m}{r_m} + \nu_{11c}\left(\frac{l'_m}{r_m}\right)^2, \\ N_{12} &= \nu_{12a} + \nu_{12b}\frac{l'_m}{r_m}, \\ N_{22} &= \nu_{22a}. \end{aligned}\right\} \quad (6)$$

Die Grössen μ und ν sind von der Art und den Dimensionen des magnetischen Ablenkfeldes und auch vom Verlauf der Hauptbahn in diesem Feld abhängig. Für homogene magnetische Sektorfelder mit beliebig gekrümmten Feldgrenzen und beliebigen Ablenk- sowie Ein- und Austrittswinkeln sind diese Grössen in den Gln. (13) und (14) im Detail angegeben.

Unter diesen Voraussetzungen für die Einzelfelder ergibt sich in einer Kombination zweier Felder (siehe Abb. 3 und Abb. 4) für die Ordinate y_B des Punktes, in dem der Nebenstrahl auf einem zum Hauptstrahl senkrechten und durch den Punkt $x_m = l''_m$ der x_m-Achse gehenden Schirm auftrifft, die Beziehung

$$y_B = r_m[B_1\alpha + B_2\beta + B_{11}\alpha^2 + B_{12}\alpha\beta + B_{22}\beta^2], \quad (7)$$

worin die Grössen B Abkürzungen für die folgenden Ausdrücke sind[1]):

$$\left.\begin{aligned} B_1 &= \pm S_{1a}L_1 \pm S_{1b}T_1, \\ B_2 &= \pm S_{1a}L_2 \pm S_{1b}T_2 + S_{2a}, \\ B_{11} &= \pm S_{1a}L_{11} \pm S_{1b}T_{11} + S_{11a}L_1^2 \\ &\quad + S_{11b}L_1T_1 + S_{11c}T_1^2, \\ B_{12} &= \pm S_{1a}L_{12} \pm S_{1b}T_{12} + 2S_{11a}L_1L_2 \\ &\quad + S_{11b}(L_1T_2 + L_2T_1) + 2S_{11c}T_1T_2 \\ &\quad \pm S_{12a}L_1 \pm S_{12b}T_1, \\ B_{22} &= \pm S_{1a}L_{22} \pm S_{1b}T_{22} + S_{11a}L_2^2 + S_{11b}L_2T_2 \\ &\quad + S_{11c}T_2^2 \pm S_{12a}L_2 \pm S_{12b}T_2 + S_{22a}. \end{aligned}\right\} \quad (8)$$

(Das obere Vorzeichen gilt für gleichsinnige Ablenkung, das untere für gegensinnige Ablenkung im elektrischen und magnetischen Feld.) Die Grössen S_i und T_k haben die Bedeutung:

$$S_i = \mu_i + \nu_i\frac{l''_m}{r_m} \quad (9)$$

$$(i = 1a, 1b, 2a, 11a, 11b, 11c, 12a, 12b, 22a)$$

$$T_k = K_k\frac{r_e}{r_m} + L_k\frac{d}{r_m} \quad (k = 1, 2, 11, 12, 22). \quad (10)$$

Die Ausdrücke K und L sind durch die Gln. (2) und (3) gegeben, die Grössen μ und ν wurden durch die Gln. (5) und (6) definiert. d ist der Abstand der beiden Felder (siehe Abb. 3 und Abb. 4).

Der Koeffizient B_1 verschwindet für Richtungsfokussierung erster Ordnung. B_2 ist der Koeffizient der Geschwindigkeitsdispersion. B_{11}, B_{12} und B_{22} sind die Koeffizienten für den Öffnungsfehler, die gemischt geschwindigkeits-

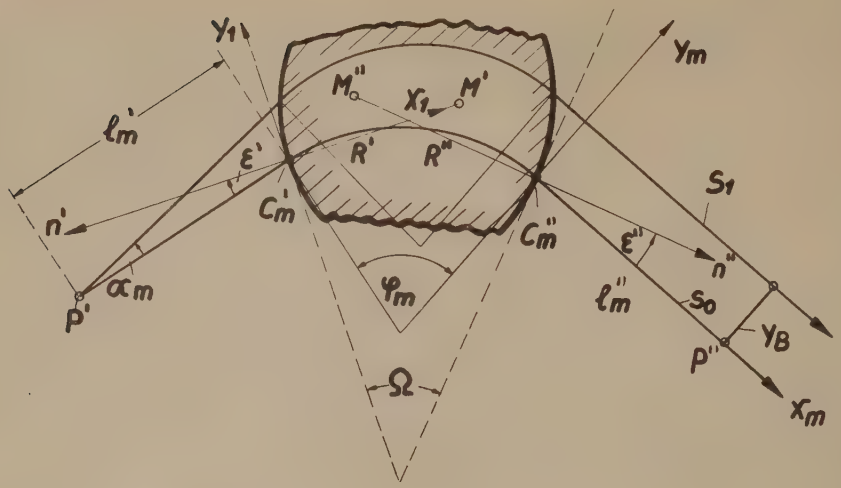

Abb. 2. Die Koordinatensysteme x_m, y_m und x_1, y_1, die zur Bahnberechnung für das homogene Sektorfeld benutzt wurden (s_0 = Mittelbahn, die von Teilchen der Geschwindigkeit $v = v_0$ mit $\alpha_m = 0$ durchlaufen wird; s_1 = Nachbarbahn von Teilchen mit $v = v_0\,(1 + \beta)$ und $\alpha_m \neq 0$). ε' und ε'' sind positiv, wenn die Normalen n' und n'' auf der vom Ablenkungszentrum abgewendeten Seite von s_0 liegen. Die Krümmungsradien der Feldgrenzen R' und R'' in den Punkten C'_m und C''_m sind für konvexe Krümmung der Polschuhe (wie in der Abb.) positiv, für konkave Krümmung negativ in die angegebenen Formeln einzusetzen.

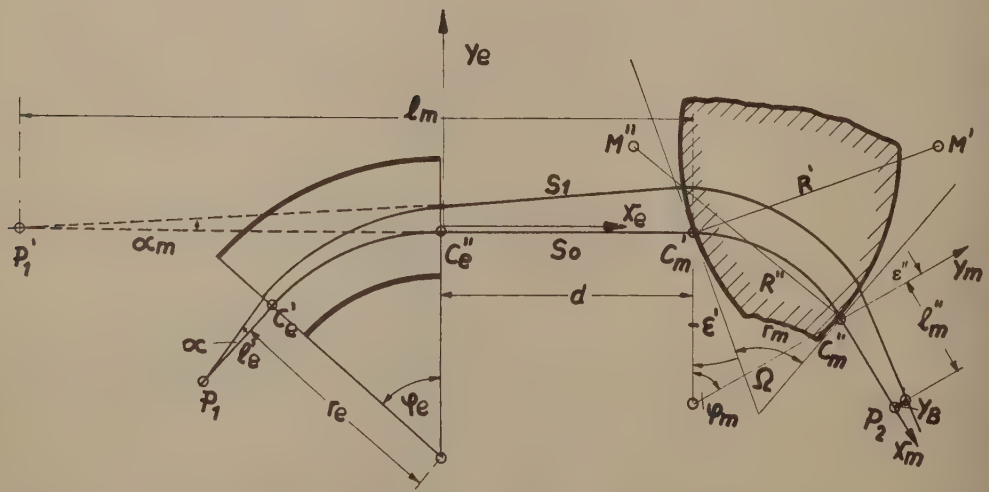

Abb. 3. Bahnverlauf (schematisch) bei gleichsinniger Ablenkung im elektrischen und magnetischen Feld. Die Lage des "Zwischenbildes" P'_1 ist von α und β abhängig (s_0 = Mittelbahn, die von Teilchen der Geschwindigkeit $v = v_0$ mit $\alpha = 0$ durchlaufen wird; s_1 = Nachbarbahn von Teilchen mit $v = v_0\,(1 + \beta)$ und $\alpha \neq 0$).

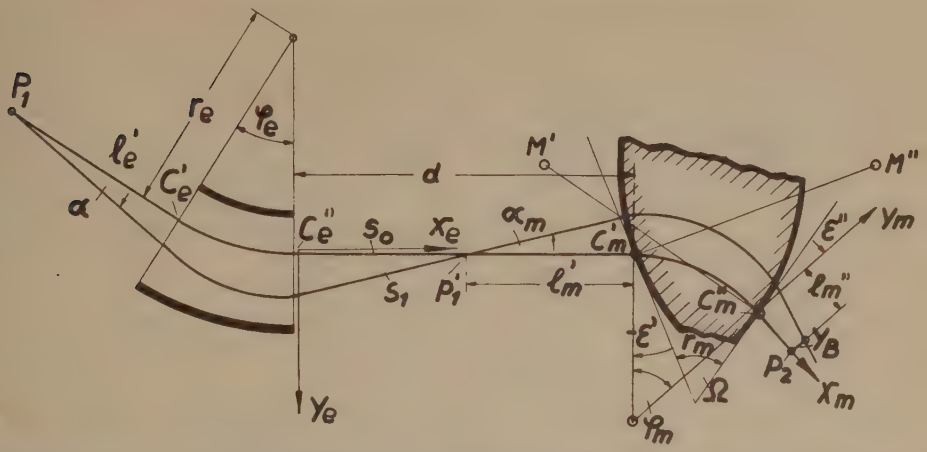

Abb. 4. Bahnverlauf (schematisch) bei gegensinniger Ablenkung im elektrischen und magnetischen Feld. Die Lage des "Zwischenbildes" P'_1 ist von α und β abhängig (s_0 = Mittelbahn, die von Teilchen der Geschwindigkeit $v = v_0$ mit $\alpha = 0$ durchlaufen wird; s_1 = Nachbarbahn von Teilchen mit $v = v_0\,(1+\beta)$ und $\alpha \neq 0$).

und öffnungswinkelabhängige Aberration und die rein geschwindigkeitsabhängige Aberration.

In einem doppelfokussierenden Massenspektrographen sind in der Regel ein elektrisches und ein magnetisches Feld hintereinandergeschaltet. Für den Fall, dass als elektrisches Feld ein Zylinderkondensator und als magnetisches Feld ein beliebig begrenztes homogenes magnetisches Sektorfeld benutzt wird, sind die in den Gln. (2) und (3) vorkommenden Koeffizienten $\varkappa$ und λ bzw. die in den Gln. (5) und (6) vorkommenden Koeffizienten μ und ν gegeben durch[1])

$$
\left.\begin{aligned}
\varkappa_{1a} &= \frac{1}{\sqrt{2}}\sin(\sqrt{2}\,\varphi_e)\,,\\
\varkappa_{1b} &= \cos(\sqrt{2}\,\varphi_e),\\
\varkappa_{2a} &= 1-\cos(\sqrt{2}\,\varphi_e)\,,\\
\varkappa_{11a} &= -\frac{3}{8}+\frac{2}{3}\cos(\sqrt{2}\,\varphi_e)-\frac{7}{24}\cos(2\sqrt{2}\,\varphi_e),\\
\varkappa_{11b} &= -\frac{4}{3\sqrt{2}}\sin(\sqrt{2}\,\varphi_e)+\frac{7}{6\sqrt{2}}\sin(2\sqrt{2}\,\varphi_e),\\
\varkappa_{11c} &= -\frac{3}{4}+\frac{1}{6}\cos(\sqrt{2}\,\varphi_e)+\frac{7}{12}\cos(2\sqrt{2}\,\varphi_e)\,,\\
\varkappa_{12a} &= \frac{7}{3\sqrt{2}}\left(\sin(\sqrt{2}\,\varphi_e)-\frac{1}{2}\sin(2\sqrt{2}\,\varphi_e)\right),\\
\varkappa_{12b} &= \frac{3}{2}-\frac{1}{3}\cos(\sqrt{2}\,\varphi_e)-\frac{7}{6}\cos(2\sqrt{2}\,\varphi_e)\,,\\
\varkappa_{22a} &= \frac{1}{4}-\frac{5}{6}\cos(\sqrt{2}\,\varphi_e)+\frac{7}{12}\cos(2\sqrt{2}\,\varphi_e)\,;
\end{aligned}\right\}\quad(11)
$$

$$
\left.\begin{aligned}
\lambda_{1a} &= \cos(\sqrt{2}\,\varphi_e)\,,\\
\lambda_{1b} &= -\sqrt{2}\sin(\sqrt{2}\,\varphi_e)\,,\\
\lambda_{2a} &= \sqrt{2}\sin(\sqrt{2}\,\varphi_e)\,,\\
\lambda_{11a} &= -\frac{\sqrt{2}}{3}\left(2\sin(\sqrt{2}\,\varphi_e)-\sin(2\sqrt{2}\,\varphi_e)\right)\,,\\
\lambda_{11b} &= -\frac{4}{3}\left(\cos(\sqrt{2}\,\varphi_e)-\cos(2\sqrt{2}\,\varphi_e)\right)\,,\\
\lambda_{11c} &= -\frac{\sqrt{2}}{6}\left(\sin(\sqrt{2}\,\varphi_e)+4\sin(2\sqrt{2}\,\varphi_e)\right)\,,\\
\lambda_{12a} &= \frac{4}{3}\left(\cos(\sqrt{2}\,\varphi_e)-\cos(2\sqrt{2}\,\varphi_e)\right)\,,\\
\lambda_{12b} &= \frac{4}{3}\sqrt{2}\left(\sin(\sqrt{2}\,\varphi_e)+\sin(2\sqrt{2}\,\varphi_e)\right)\,,\\
\lambda_{22a} &= -\frac{\sqrt{2}}{6}\left(\sin(\sqrt{2}\,\varphi_e)+4\sin(2\sqrt{2}\,\varphi_e)\right)\,.
\end{aligned}\right\}\quad(12)
$$

(Die Bedeutung des in (11) und (12) vorkommenden Winkels φ_e ist aus Abb. 1 zu ersehen.)

$$
\left.\begin{aligned}
\mu_{1a} &= \sin\varphi_m\,,\\
\mu_{1b} &= \frac{\cos(\varphi_m-\varepsilon')}{\cos\varepsilon'}\,,\\
\mu_{2a} &= 1-\cos\varphi_m\,,\\
\mu_{11a} &= \frac{1}{2}\left[\cos\varphi_m\,(1-\cos\varphi_m)+\mathrm{tg}^2\,\varepsilon''\sin^2\varphi_m\right],\\
\mu_{11b} &= \frac{\cos(\varphi_m-\varepsilon')}{\cos\varepsilon'}\left[\mathrm{tg}\,\varepsilon'+\mathrm{tg}\,\varepsilon''\frac{\cos(\varphi_m-\varepsilon'')}{\cos\varepsilon''}\right]\\
&\quad+\cos\varphi_m\frac{\sin(\varphi_m-\varepsilon'-\varepsilon'')}{\cos\varepsilon'\cos\varepsilon''}\\
\mu_{11c} &= -\frac{1}{2}\frac{\sin(\varphi_m-\varepsilon'-\varepsilon'')}{\cos\varepsilon'\cos\varepsilon''}\left[\frac{\sin(\varphi_m-\varepsilon'-\varepsilon'')}{\cos\varepsilon'\cos\varepsilon''}\right.
\end{aligned}\right\}\quad(13)
$$

$$+ 2 \operatorname{tg} \varepsilon'' \frac{\cos(\varphi_m - \varepsilon')}{\cos \varepsilon'} \Big] + \frac{\sin \varphi_m}{2 \cos^3 \varepsilon'} \frac{r_m}{R'},$$

$$\mu_{12a} = \sin \varphi_m \frac{1 - \cos \varphi_m}{\cos^2 \varepsilon''},$$

$$\mu_{12b} = \operatorname{tg} \varepsilon'' \left[\operatorname{tg} \varepsilon'' + \frac{\sin(\varphi_m - \varepsilon'')}{\cos \varepsilon''}\right] \frac{\cos(\varphi_m - \varepsilon')}{\cos \varepsilon'} + \sin \varphi_m \frac{\sin(\varphi_m - \varepsilon' - \varepsilon'')}{\cos \varepsilon' \cos \varepsilon''},$$

$$\mu_{22a} = \operatorname{tg} \varepsilon'' \left[\operatorname{tg} \varepsilon'' + \frac{\sin(\varphi_m - \varepsilon'')}{\cos \varepsilon''}\right] (1 - \cos \varphi_m) - \frac{1}{2} \left[\operatorname{tg} \varepsilon'' + \frac{\sin(\varphi_m - \varepsilon'')}{\cos \varepsilon''}\right]^2;$$

$$\nu_{1a} = \frac{\cos(\varphi_m - \varepsilon'')}{\cos \varepsilon''},$$

$$\nu_{1b} = -\frac{\sin(\varphi_m - \varepsilon' - \varepsilon'')}{\cos \varepsilon' \cos \varepsilon''},$$

$$\nu_{2a} = \operatorname{tg} \varepsilon'' + \frac{\sin(\varphi_m - \varepsilon'')}{\cos \varepsilon''},$$

$$\nu_{11a} = -\frac{1}{2} \left[\frac{\sin(\varphi_m - \varepsilon'')}{\cos \varepsilon''} + \operatorname{tg} \varepsilon'' \frac{\cos^2(\varphi_m - \varepsilon'')}{\cos^2 \varepsilon''}\right] + \frac{\sin^2 \varphi_m}{2 \cos^3 \varepsilon''} \frac{r_m}{R''},$$

$$\nu_{11b} = -\frac{\sin(\varphi_m - \varepsilon' - \varepsilon'')}{\cos \varepsilon' \cos \varepsilon''} \left[\operatorname{tg} \varepsilon' - \operatorname{tg} \varepsilon'' \times \frac{\cos(\varphi_m - \varepsilon'')}{\cos \varepsilon''}\right] + \frac{\sin \varphi_m}{\cos^3 \varepsilon''} \frac{\cos(\varphi_m - \varepsilon')}{\cos \varepsilon'} \frac{r_m}{R''},$$

$$\nu_{11c} = -\frac{1}{2} \operatorname{tg} \varepsilon'' \frac{\sin^2(\varphi_m - \varepsilon' - \varepsilon'')}{\cos^2 \varepsilon' \cos^2 \varepsilon''} + \frac{\cos^2(\varphi_m - \varepsilon')}{2 \cos^2 \varepsilon' \cos^3 \varepsilon''} \frac{r_m}{R''} + \frac{\cos(\varphi_m - \varepsilon'')}{2 \cos^3 \varepsilon' \cos \varepsilon''} \frac{r_m}{R'},$$

$$\nu_{12a} = -\frac{\cos(\varphi_m - \varepsilon'')}{\cos \varepsilon''} \left[\operatorname{tg} \varepsilon'' + \frac{\sin(\varphi_m - \varepsilon'')}{\cos \varepsilon''}\right] \operatorname{tg} \varepsilon'' + \frac{\sin \varphi_m (1 - \cos \varphi_m)}{\cos^3 \varepsilon''} \frac{r_m}{R''}$$

$$\nu_{12b} = \frac{\sin(\varphi_m - \varepsilon' - \varepsilon'')}{\cos \varepsilon' \cos \varepsilon''} \left\{1 + \operatorname{tg} \varepsilon'' \left[\operatorname{tg} \varepsilon'' + \frac{\sin(\varphi_m - \varepsilon'')}{\cos \varepsilon''}\right]\right\} + \frac{\cos(\varphi_m - \varepsilon')}{\cos \varepsilon'} \frac{1 - \cos \varphi_m}{\cos^3 \varepsilon''} \frac{r_m}{R''}$$

$$\nu_{22a} = -\frac{1}{2} \operatorname{tg} \varepsilon'' \left[\operatorname{tg} \varepsilon'' + \frac{\sin(\varphi_m - \varepsilon'')}{\cos \varepsilon''}\right]^2 - \left[\operatorname{tg} \varepsilon'' + \frac{\sin(\varphi_m - \varepsilon'')}{\cos \varepsilon''}\right] + \frac{(1 - \cos \varphi_m)^2}{2 \cos^3 \varepsilon''} \frac{r_m}{R''}. \qquad (14)$$

(Die Bedeuting der in (13) und (14) vorkommenden Grössen ist aus Abb. 2 zu ersehen.)

Soll Doppelfokussierung erster Ordnung erreicht werden, so müssen die nachstehenden Gln. (15a) und (15b) erfüllt sein. Soll vollständige Doppelfokussierung zweiter Ordnung erreicht werden, so müssen die Gln. (15a) bis (15e) gleichzeitig befriedigt werden. Diese Gleichungen lauten:

$$\begin{aligned} &\text{a)}\ B_1 = 0\,, && \text{c)}\ B_{11} = 0\,, \\ &\text{b)}\ B_2 = 0\,, && \text{d)}\ B_{12} = 0\,, \\ & && \text{e)}\ B_{22} = 0\,. \end{aligned} \qquad (15)$$

Die Grössen B sind durch die Gln. (8) zusammen mit (2), (3), und (9) bis (14) bestimmt.

Für Massenspektrographen mit Doppelfokussierung erster Ordnung für alle Massen entlang einer geraden Bildkurve wird in den obigen Gleichungen $S_{1b} = L_1 = 0$.

2.2. ZWEITE METHODE

Die zweite Methode zur Berechnung der Korrekturgleichungen ist die folgende[5]; man denkt sich — siehe Abb. 5 — vom Gegenstandspunkt P_1 aus ein Strahlenbündel in das elektrische Feld und vom Bildpunkt P_2 aus ein weiteres Strahlenbündel in das magnetische Ablenkfeld hineingeschossen. Hierbei sollen die Mittelstrahlen beider Strahlenbündel zusammenfallen. Fordert man nun, dass auch jeder Nebenstrahl des einen Bündels mit einem Nebenstrahl des andern Bündels zusammenfällt, so erhält man die Bedingungen für dieDoppelfokussierung zweiter Ordnung in neuer Formulierung. Wir beschränken uns in dieser Arbeit auf Massenspektrographen mit Doppelfokussierung erster Ordnung für alle Massen entlang einer geraden Bildkurve. Dann liegt der Gegenstand im Brennpunkt der elektrostatischen Linse und das Bild im Brennpunkt der magnetischen Linse. Für diesen Fall lauten die Bedingungsleichungen für die Korrektur der Bildfehler, die sich nach dem zweiten Verfahren ergeben[5])

$$A_i = 0 \quad (i = 11, 12, 22)\,. \qquad (16)$$

Die grössen A_i sind Abkürzungen mit der Bedeutung

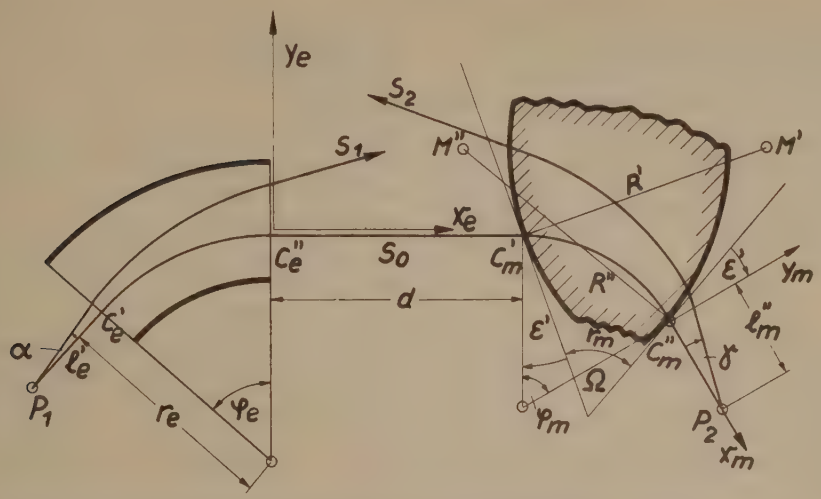

Abb. 5. Von den Punkten P_1 und P_2 ausgehende Strahlenbündel ,für die die Mittelstrahlen ($\alpha = \beta = \gamma = \vartheta$) zusammenfallen. Aus der Forderung, dass die Nebenstrahlen s_1 ($\alpha \neq 0, \beta \neq 0$) und s_2 ($\gamma \neq 0, \beta \neq 0$) zusammenfallen sollen, folgt die zweite Fassung der Doppelfokussierungsbedingungen zweiter Ordnung[5]).

$$
\left.
\begin{aligned}
\text{a)}\ A_{11} &= \pm L_{11} + N'_{11}\frac{K_1^2}{M'^2_1}\left(\frac{r_e}{r_m}\right)^2, \\
\text{b)}\ A_{12} &= \pm L_{12} + 2\frac{N'_{11}K_1}{M'^2_1}\frac{r_e}{r_m}\left[\frac{r_e}{r_m}K_2 \right. \\
&\quad \left. + \frac{d}{r_m}L_2 \mp M'_2\right] \pm \frac{r_e}{r_m}\frac{N'_{12}K_1}{M'_1}, \\
\text{c)}\ A_{22} &= \pm L_{22} + N'_{22} \\
&\quad \pm \frac{N'_{12}}{M'_1}\left[\frac{r_e}{r_m}K_2 + \frac{d}{r_m}L_2 \mp M'_2\right] \\
&\quad + \frac{N'_{11}}{M'^2_1}\left[\frac{r_e}{r_m}K_2 + \frac{d}{r_m}L_2 \mp M'_2\right]^2.
\end{aligned}
\right\} \quad (17)
$$

Die Grössen M'_i, N'_i ($i = 1, 2, 11, 12, 22$) gehen aus den M, N der Gln. (5), (6), (13) und (14) hervor, indem man die Indizes' und" vertauscht, die die Ein- und Austrittsseite kennzeichnen. Wie wir in einer früheren Arbeit[1]) gezeigt haben, sind die Bedingungen $B_i = 0$ mit den Bedingungen $A_i = 0$ äquivalent, weil zwischen den A_i und den B_i die Beziehung

$$B_i = M'_1 A_i \qquad \text{mit} \qquad M'_1 \neq 0 \qquad (18)$$

besteht. Bei der Ableitung der Umrechnungsformeln (18) wurden nur die Gln. (5) und (6), nicht aber die Gln. (13) und (14) für die μ, ν benutzt. Hieraus folgt, dass die μ, ν der Gln. (13) und (14) richtig berechnet sind, wenn die Gln. (18) für jedes Beispiel zahlenmässig erfüllt sind. Dies stellt eine wertvolle Kontrollmöglichkeit für die allgemeine und die numerische Rechnung dar.

3. Die Umformung des Gleichungssystems

Die im Falle der Massenspektrometer in einer früheren Arbeit[2]) vorgenommenen Umformungen können wegen des Verschwindens einiger Koeffizienten bei der Behandlung der längs einer geraden Bildkurve in erster Ordnung doppelfokussierenden Massenspektrographen nicht wiederholt werden. Es ist vielmehr eine getrennte Behandlung dieses Spezialfalles notwendig.

Hierbei ergeben sich wesentliche Vereinfachungen, weil man in diesem Fall das System der Bedingungsleichungen weitgehend allgemein auflösen kann.

3.1. DIE BEDINGUNG FÜR DOPPELFOKUSSIERUNG ERSTER ORDNUNG FÜR ALLE MASSEN BEI GERADER BILDKURVE

Die Lage von Gegenstand und Bild in den Brennpunkten der elektrostatischen und magnetischen Linse hat das bereits erwähnte Verschwinden von L_1 und N'_1 ($= S_{1b}$) zur Folge.

Damit lassen sich l'_e und l''_m berechnen. Es folgen die bekannten Ausdrücke

$$\frac{l'_e}{r_e} = \frac{1}{\sqrt{2}} \operatorname{ctg}(\sqrt{2}\,\varphi_e)\,, \tag{19}$$

$$\frac{l''_m}{r_m} = \frac{\cos\varepsilon'' \cos(\varphi_m - \varepsilon')}{\sin(\varphi_m - \varepsilon' - \varepsilon'')}\,. \tag{20}$$

Wir benutzen r_m fortan als Längeneinheit. Mit L_1 und S_{1b} verschwindet auch B_1. Für

$$\varepsilon'' = \frac{\varphi_m}{2} - \frac{\pi}{2} \tag{21}$$

und eine gerade hintere Feldgrenze wird auch die Bildkurve gerade. In diesem Fall ist also

$$1/R'' = 0\,. \tag{22}$$

Beide Gerade (Feldgrenze und Bildkurve) gehen durch den Eintrittspunkt des Mittelstrahles in das Magnetfeld. Aus den Gln. (19) bis (21) und aus der Bedingung für Geschwindigkeitsfokussierung erster Ordnung $B_2 = 0$ folgt die bekannte Beziehung[4]) für ε'

$$\operatorname{tg}\varepsilon' = \mp\frac{\sqrt{2}}{2}\frac{\sin(\sqrt{2}\,\varphi_e)}{\sin^2(\varphi_m/2)} - \operatorname{ctg}\left(\frac{\varphi_m}{2}\right). \tag{23}$$

Aus den Gln. (19), (21) bis (23) ergeben sich für die Koeffizienten K, L, μ und ν sowie für den Bildabstand l''_m/r_m wesentliche Vereinfachungen. Es gilt für Massenspektrographen mit Doppelfokussierung erster Ordnung für alle Massen:

$$\frac{l''_m}{r_m} = \frac{\sqrt{2}\sin^2(\varphi_m/2)}{\sin(\sqrt{2}\,\varphi_e)}\left[\pm 1 + \sqrt{2}\sin(\sqrt{2}\,\varphi_e)\operatorname{ctg}\left(\frac{\varphi_m}{2}\right)\right]; \tag{24}$$

$$\left.\begin{aligned}
K_1 &= \frac{\sqrt{2}}{2}\frac{1}{\sin(\sqrt{2}\,\varphi_e)}\,,\\
K_2 &= 1 - \cos(\sqrt{2}\,\varphi_e)\,,\\
K_{11} &= \frac{\cos^3(\sqrt{2}\,\varphi_e) - 1}{12\sin^2(\sqrt{2}\,\varphi_e)}\,,\\
K_{12} &= \frac{7\sqrt{2}}{6}\sin(\sqrt{2}\,\varphi_e)\\
&\quad + \frac{\sqrt{2}\cos(\sqrt{2}\,\varphi_e)}{6\sin(\sqrt{2}\,\varphi_e)}\left[1 - \cos(\sqrt{2}\,\varphi_e)\right],\\
K_{22} &= \frac{1}{4} - \frac{5}{6}\cos(\sqrt{2}\,\varphi_e) + \frac{7}{12}\cos(2\sqrt{2}\,\varphi_e)\,;
\end{aligned}\right\} \tag{25}$$

$$\left.\begin{aligned}
L_1 &= 0\,,\\
L_2 &= \sqrt{2}\sin(\sqrt{2}\,\varphi_e)\,,\\
L_{11} &= -\frac{\sqrt{2}}{12}\frac{8 + \cos^2(\sqrt{2}\,\varphi_e)}{\sin(\sqrt{2}\,\varphi_e)}\,,\\
L_{12} &= \frac{4}{3}\left[1 + 2\cos(\sqrt{2}\,\varphi_e)\right],\\
L_{22} &= -\frac{\sqrt{2}}{6}\left[\sin\sqrt{2}\,\varphi_e) + 4\sin(2\sqrt{2}\,\varphi_e)\right].
\end{aligned}\right\} \tag{26}$$

(Die Gln. (25) und (26) sind bereits in einer früheren Arbeit[5]) enthalten.)

$$\left.\begin{aligned}
\mu_{1a} &= \sin\varphi_m\,,\\
\mu_{1b} &= -1 \mp \sqrt{2}\sin(\sqrt{2}\,\varphi_e)\operatorname{ctg}\left(\frac{\varphi_m}{2}\right),\\
\mu_{2a} &= 1 - \cos\varphi_m\,,\\
\mu_{11a} &= \frac{1}{2}\left[1 + 3\cos\varphi_m\right],\\
\mu_{11b} &= \pm\sqrt{2}\sin(\sqrt{2}\,\varphi_e) + \frac{\sin^2(\sqrt{2}\,\varphi_e)\cos(\varphi_m/2)}{\sin^3(\varphi_m/2)},\\
\mu_{11c} &= \pm\frac{\sqrt{2}}{4}\frac{\sin(\sqrt{2}\,\varphi_e)}{\sin^2(\varphi_m/2)}\left[\mp\frac{\sqrt{2}}{2}\sin(\sqrt{2}\,\varphi_e\right]\\
&\quad \times\left(1 - 3\operatorname{ctg}^2\left(\frac{\varphi_m}{2}\right)\right) + 2\operatorname{ctg}\left(\frac{\varphi_m}{2}\right)\Big]\\
&\quad + \frac{1}{2}\sin\varphi_m\left[1 + \left(\mp\frac{\sqrt{2}}{2}\frac{\sin(\sqrt{2}\,\varphi_e)}{\sin^2(\varphi_m/2)}\right.\right.\\
&\quad \left.\left. - \operatorname{ctg}\left(\frac{\varphi_m}{2}\right)\right)^2\right]^{3/2}\frac{r_m}{R'}\,,\\
\mu_{12a} &= 2\sin\varphi_m\,,\\
\mu_{12b} &= \mp\sqrt{2}\sin(\sqrt{2}\,\varphi_e)\operatorname{ctg}\left(\frac{\varphi_m}{2}\right),\\
\mu_{22a} &= 0\,.
\end{aligned}\right\} \tag{27}$$

$$\left.\begin{aligned}
\nu_{1a} &= -1\,,\\
\nu_{1b} &= \pm\frac{\sqrt{2}}{2}\frac{\sin(\sqrt{2}\,\varphi_e)}{\sin^2(\varphi_m/2)}\,,\\
\nu_{2a} &= 0\,,\\
\nu_{11a} &= 0\,,\\
\nu_{11b} &= \pm\frac{\sqrt{2}}{2}\frac{\sin(\sqrt{2}\,\varphi_e)}{\sin^2\varphi_m/2)}\left[\frac{\mp\sqrt{2}\sin(\sqrt{2}\,\varphi_e)}{2\sin^2(\varphi_m/2)}\right.\\
&\quad \left. - 2\operatorname{ctg}\left(\frac{\varphi_m}{2}\right)\right],\\
\nu_{11c} &= \frac{\sin^2(\sqrt{2}\,\varphi_e)\cos(\varphi_m/2)}{4\sin^5(\varphi_m/2)}\\
&\quad - \frac{1}{2}\left[1 + \left(\mp\frac{\sqrt{2}}{2}\frac{\sin(\sqrt{2}\,\varphi_e)}{\sin^2(\varphi_m/2)}\right.\right.\\
&\quad \left.\left. - \operatorname{ctg}\left(\frac{\varphi_m}{2}\right)\right)^2\right]^{3/2}\frac{r_m}{R'}\,,\\
\nu_{12a} &= 0\,,\\
\nu_{12b} &= \mp\frac{\sqrt{2}}{2}\frac{\sin(\sqrt{2}\,\varphi_e)}{\sin(\varphi_m/2)}\,,\\
\nu_{22a} &= 0\,.
\end{aligned}\right\} \tag{28}$$

3.2. DIE BEDINGUNGEN FÜR DIE KORREKTUR DER EINZELNEN BILDFEHLER

Die Bedingungsgleichungen für die Korrektur der einzelnen Bildfehler enthalten die fünf Grössen φ_m, φ_e, R'/r_m, r_e/r_m und d/r_m. Im Prinzip

kann man vier davon frei wählen. Werden φ_m und φ_e vorgegeben, so lassen sich aus den Bedingungen für die Doppelfokussierung erster Ordnung nach den Gln. (19), (21), (23) und (24) die Grössen l'_e, ε'', ε' und l'_m bestimmen. Zwei von den übrig bleibenden Grössen R'/r_m, r_e/r_m und d/r_m können also noch frei gewählt werden. Die dritte ist dann durch die Korrekturgleichung für den betreffenden Bildfehler bestimmt.

(a) Die Korrektur des Öffnungsfehlers

Die Beziehung $B_{11} = 0$ lässt sich leicht nach r_e/r_m auflösen. Man erhält

$$\left(\frac{r_e}{r_m}\right)_{\alpha^2} = \sqrt{\mp \frac{S_{1a} L_{11}}{K_1^2 S_{11c}}}\,. \tag{29}$$

Die Grössen K, L und S sind durch die Gln. (25), (26) und (9) zusammen mit (24), (27) und (28) bestimmt.

Durch den Index α^2 wird angedeutet, dass der Koeffizient von α^2 in Gl. (7) verschwindet, wenn $r_e/r_m = (r_e/r_m)_{\alpha^2}$ gewählt wird.

Wir haben diese Bedingung in etwas anderer Formulierung bereits früher[6]) angegeben und gezeigt, dass z.B. für einen Apparat vom Mattauch-Herzogschen Typ der Öffnungsfehler an der Stelle der Photoplatte, für die $r_e/r_m = \sqrt{(17/6)}$ ist, korrigiert ist.

(b) Die Korrektur der gemischt öffnungswinkel- und geschwindigkeitsabhängigen Aberration

Aus $B_{12} = 0$ folgt für d/r_m

$$\left(\frac{d}{r_m}\right)_{\alpha\beta} = \mp \frac{S_{1a} L_{12}}{2\, S_{11c} K_1 (r_e/r_m) L_2} - \frac{S_{11b}}{2\, S_{11c}} - \frac{K_2}{L_2}\frac{r_e}{r_m} \mp \frac{S_{12b}}{2\, S_{11c} L_2}\,. \tag{30}$$

Die Grössen K, L und S sind durch die Gln. (25), (26) und (9) zusammen mit (24), (27) und (28) bestimmt. Durch den Index $\alpha\beta$ wird angedeutet, dass der Koeffizient von $\alpha\beta$ in Gl. (7) verschwindet, wenn $d/r_m = (d/r_m)_{\alpha\beta}$ gewählt wird. Im Gegensatz von $(r_e/r_m)_{\alpha^2}$ hängt $(d/r_m)_{\alpha\beta}$ von einem Parameter mehr ab. Statt $(d/r_m)_{\alpha\beta}$ hätte man aus $B_{12} = 0$ auch den Ausdruck für $(r_e/r_m)_{\alpha\beta}$ ableiten können.

(c) Die Korrektur der rein geschwindigkeitsabhängigen Aberration

Die Gleichung $B_{22} = 0$ ist bezüglich d/r_m vom zweiten Grad. Ihre Lösungen lauten:

$$\text{a)}\ \left(\frac{d}{r_m}\right)_{\beta^2,1} = \frac{1}{L_2}\left[-\frac{r_e}{r_m} K_2 - \frac{U}{2} + \sqrt{\frac{U^2}{4} - V}\right]$$

$$\text{b)}\ \left(\frac{d}{r_m}\right)_{\beta^2,2} = \frac{1}{L_2}\left[-\frac{r_e}{r_m} K_2 - \frac{U}{2} - \sqrt{\frac{U^2}{4} - V}\right] \tag{31}$$

mit $U = \frac{1}{S_{11c}}[\pm S_{12b} + S_{11b} L_2]$, (31)′

und $V = \frac{1}{S_{11c}}[\pm S_{1a} L_{22} + S_{11a} L_2^2 \pm S_{12a} L_2]$.

Die Grössen K, L und S sind durch die Gln. (25), (26) und (9) zusammen mit (24), (27) und (28) bestimmt.

Sinngemäss abgeändert gilt hier dieselbe Bemerkung wie nach Gl. (30).

3.3. BEDINGUNGEN FÜR DIE GLEICHZEITIGE KORREKTUR ZWEIER BILDFEHLER

An den Gln. (29) bis (31) erkennt man, dass es möglich sein muss, zwei Bildfehler gleichzeitig zu korrigieren. Allerdings kann man nicht ohne genaue Prüfung ersehen, ob diese Lösungen wirklich sinnvoll sind.

Praktisch wichtig sind die Fälle, für welche die beiden von α oder die beiden von β abhängigen Bildfehler zweiter Ordnung verschwinden. Die so gefundenen Apparate fokussieren also entweder Strahlenbündel mit grossen Öffnungswinkel oder grössere Bereiche energieinhomogener Ionen.

(a) Gleichzeitige Korrektur der von α^2 und von $\alpha\beta$ abhängigen Bildfehler

Aus den Gln. (29) und (30) folgt, dass B_{11} und B_{12} gleichzeitig verschwinden, wenn

$$\frac{d}{r_m} = \left(\frac{d}{r_m}\right)_{\alpha\beta}\left(\varphi_m, \sqrt{2}\,\varphi_e, \frac{r_m}{R'}, \left(\frac{r_e}{r_m}\right)_{\alpha^2}\right) \tag{32}$$

gewählt wird. Da nach Gl. (29) $(r_e/r_m)_{\alpha^2} = (r_e/r_m)_{\alpha^2}(\varphi_m, \sqrt{2}\,\varphi_e, r_m/R')$ ist, wird damit nach Gl. (32) d/r_m eine Funktion von φ_m, $\sqrt{2}\,\varphi_e$, r_m/R'. Zu vorgegebenen Wertetripel $(\varphi_m, \sqrt{2}\,\varphi_e, r_m/R')$ folgen also aus den Gln. (19), (21), (23), (24), (29) und (32) die Abmessungen der Apparate mit korrigiertem B_{11} und B_{12}.

(*b*) *Gleichzeitige Korrektur der von $\alpha\beta$ und β^2 abhängigen Bildfehler*

Die Bedingungen für das gleichzeitige Verschwinden von B_{12} und B_{22} erhält man nach etwas Zwischenrechnung. Der Ansatz nach den Gln. (30) und (31)

$$\left(\frac{d}{r_m}\right)_{\alpha\beta} = \left(\frac{d}{r_m}\right)_{\beta^2,1} \text{ bzw. } \left(\frac{d}{r_m}\right)_{\alpha\beta} = \left(\frac{d}{r_m}\right)_{\beta^2,2}$$

ergibt eine Beziehung für r_e/r_m

$$\frac{r_e}{r_m} \equiv \left(\frac{r_e}{r_m}\right)_{\alpha\beta,\beta^2} = \left\{\frac{S_{1a}^2 L_{12}^2}{4 S_{11c}^2 K_1^2}\left(\frac{U^2}{4} - V\right)^{-1}\right\}^{1/2}, \quad (33)$$

wobei die Ausdrücke U, V, K, L durch die Gln. (31)′, (25) und (26) erklärt sind. Zu vorgegebenem φ_m, φ_e und r_m/R' liefert Gl. (33) den zugehörigen Wert von r_e/r_m. Aus φ_m, φ_e, r_m/R' und r_e/r_m folgen nach den Gln. (19), (21), (23), (24) und (30) die übrigen Abmessungen der Apparate mit korrigiertem B_{12} und B_{22}.

3.4. Die Bedingung für die gleichzeitige Korrektur der drei von α und β quadratisch abhängigen Bildfehler (vollständige Doppelfokussierung zweiter Ordnung)

Die Bedingung für die vollständige Doppelfokussierung zweiter Ordnung folgt sofort aus den Gln. (29) und (33), wenn man ansetzt

$$\left(\frac{r_e}{r_m}\right)_{\alpha^2} = \left(\frac{r_e}{r_m}\right)_{\alpha\beta,\beta^2}.$$

Nach Umformung erhält man das Ergebnis

$$\frac{U^2}{4} - V = \mp \frac{S_{1a} L_{12}^2}{4 S_{11c} L_{11}} \quad (34)$$

wobei die Ausdrücke U, V, S und L durch die Gln. (31)′, (9), (24), (27), (28) und (26) erklärt sind. Gl. (34) stellt eine Beziehung zwischen φ_m, φ_e und r_m/R' dar. Zu jedem Wertetripel dieser Parameter, von denen zwei willkürlich gewählt und der dritte aus Gl. (34) bestimmt werden kann, folgen aus den Gln. (19), (21), (23), (24), (29) und (30) die übrigen Abmessungen der Apparate mit vollständiger Doppelfokussierung zweiter Ordnung.

4. Das numerische Rechenverfahren

Wenn nur zwei Bildfehler korrigiert werden sollen, ist die numerische Rechnung einfach, weil dann nur in die allgemeinen Ausdrücke (19), (21), (23), (24), (29) und (30) bzw. (31) vorgegebene Werte von φ_m, φ_e und R' einzusetzen sind. Im Falle der von zweiter Ordnung vollständig doppelfokussierenden Apparate muss hingegen die bezüglich φ_m und φ_e transzendente Gl. (34) gelöst werden. Dies wurde so durchgeführt, dass wir

$$f = \frac{U^2}{4} - V \pm \frac{S_{1a} L_{12}^2}{4 S_{11c} L_{11}}$$

(U, V, S und L werden durch die Gln. (9), (24), (27), (28), (26) und (31)′ bestimmt) ansetzten und für konstante φ_e und R' für verschiedene φ_m in äquidistanten Schritten $\Delta\varphi_m$ die Funktionswerte f berechneten. Trat in einem Intervall Vorzeichenwechsel ein, so wurde dasselbe halbiert und so fort, bis $|f| < 10^{-2}$ geworden war. Mit den so bestimmten Werten φ_m, φ_e, R' wurden nach den Gln. (19), (21), (23), (24), (29) und (30) die Abmessungen der zugehörigen Apparate mit gleichzeitig korrigiertem B_{11} und B_{12} berechnet. Es zeigte sich, dass die Schranke 10^{-2} fast immer $|B_{22}| < 10^{-3}$ werden lässt. Auch in den ungünstigsten Fällen bleibt $|B_{22}| < 5 \times 10^{-2}$, so dass auf diesem Wege die Abmessungen von Apparaten mit vollständiger Doppelfokussierung zweiter Ordnung erhalten werden. Wegen des Vorzeichenwechsels von f kann durch Vorgabe einer kleineren Schranke für $|f|$ auch $|B_{22}|$ *beliebig* klein gemacht werden. Es ist jedoch praktisch nicht mehr sinnvoll, die Schranke noch kleiner zu wählen, und kompliziert nur die Rechnung.

Wir haben zur Berechnung der Nullstellen von f auch versuchsweise die regula falsi benutzt. Es zeigte sich jedoch, dass das Verfahren der Intervallhalbierung sehr viel schneller zum Ziel führte.

Alle numerischen Rechnungen wurden auf IBM-Magnettrommelrechnern Type 650 in den Rechenzentren der Firma IBM Deutschland in Sindelfingen/Württ. bzw. der Deutschen Bau- und Bodenbank, Mainz, durchgeführt. Die Programmierung wurde von dem einen von uns (L.A.K.) besorgt.

Die Rechenkontrollen waren dieselben wie in einer früheren Arbeit[2]). Es wurden die vorein-

ander unabhängig abgeleiteten Gln. (15) und (16) benutzt, wobei in den berechneten $B'_i = M'_1 A_i$ (Gl. (18)) die μ' ν' in der ursprünglichen, von ε' und ε'' abhängigen Form eingesetzt wurden. Zu jeder in den Tabellen angegebenen Lösung wurde mit der elektronischen Rechenmaschine eine Probe gerechnet. Ausserdem wurden mit der Tischrechenmaschine Stichproben vorgenommen.

5. Die Ergebnisse

Sowohl für gleichsinnige als auch für gegensinnige Ablenkung können Apparate, für die an einer Stelle der Photoplatte

(a) $B_{11} = B_{12} = 0, \quad B_{22} \neq 0,$
oder (b) $B_{12} = B_{22} = 0, \quad B_{11} \neq 0,$
oder (c) $B_{11} = B_{12} = B_{22} = 0$ ist,

angegeben werden. Allgemein kann man sagen, dass die Apparate mit vollständiger Doppelfokussierung zweiter Ordnung (c) stets grosse Radialfelder aufweisen. Apparate von den Typen (a) und (c) gibt es nur in dem Bereich $\sqrt{2}\,\varphi_e > \pi$. In unserer früheren Arbeit[5]) hatten wir diesen Bereich nicht behandelt.

Neben den physikalisch brauchbaren Lösungen gibt es auch unbrauchbare. Die Bedingungen für Doppelfokussierung erster Ordnung und für die Form der Bildkurve bewirken, dass es unabhängig von R' in der $(\varphi_m, \sqrt{2}\,\varphi_e)$-Ebene verbotene Bereiche gibt, in denen l'_e bzw. l''_m negativ werden. In den Abb. 6 und 7 sind diese Bereiche schraffiert eingetragen. Neben l'_e und l''_m können nun auch d und r_e physikalisch sinnlos werden. d kann negativ oder komplex werden, r_e imaginär. Die Bereiche, in denen dies der Fall ist, liegen teilweise in den bezüglich l'_e und l''_m erlaubten Bereichen. Da ihre Grenzen von R' abhängig sind, werden die Verhältnisse sehr kompliziert. Zu ihrer Darstellung wäre eine grössere Zahl von Diagrammen notwendig, weshalb wir aus Platzersparnis auf eine ausführliche Wiedergabe verzichten.

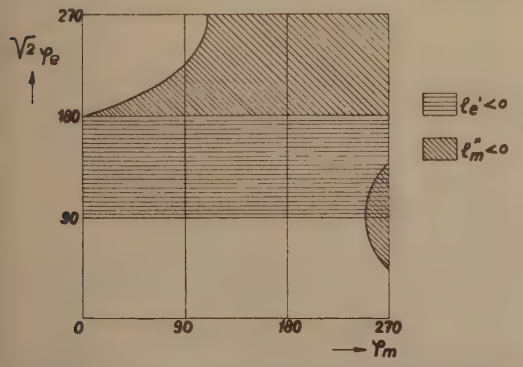

Abb. 6. Bereiche, in denen bei gleichsinniger Ablenkung keine Doppelfokussierung erster Ordnung möglich ist, weil $l'_e < 0$ oder $l''_m < 0$ wird.

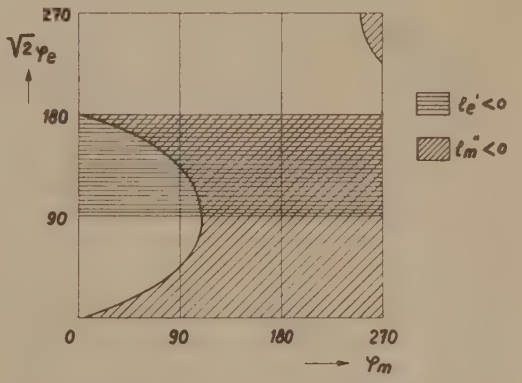

Abb. 7. Bereiche, in denen bei gegensinniger Ablenkung keine Doppelfokussierung erster Ordnung möglich ist, weil $l'_e < 0$ oder $l''_m < 0$ wird.

In den beiden folgenden Abschnitten gehen wir auf die Ergebnisse für gleichsinnige und für gegensinnige Ablenkung näher ein. Wir möchten besonders darauf hinweisen, dass wir für die folgenden Tabellen nur die besten von den vielen bei der systematischen Suche gefundenen Lösungen ausgewählt haben.

5.1. GLEICHSINNIGE ABLENKUNG

(a) Apparate mit $B_{11} = B_{12} = 0, B_{22} \neq 0$

Es gelang uns nur, in dem Bereich $180° < \sqrt{2}\,\varphi_e \leq 270°$ physikalisch brauchbare Lösungen für Apparate mit gleichsinniger Ablenkung zu finden, bei denen die beiden von α abhängigen Bildfehler B_{11} und B_{12} gleichzeitig korrigiert sind. Eine Auswahl von solchen Lösungen ist in Tabelle 1 zusammengestellt. Wie man sieht, gibt es Apparate von vernünftigen Abmessungen. (Siehe Abb. 8.)

(*b*) *Apparate mit* $B_{12} = B_{22} = 0$, $B_{11} \neq 0$

Die von β abhängigen Bildfehler B_{12} und B_{22} lassen sich ebenfalls im Falle gleichsinniger Ablenkung gleichzeitig korrigieren, wobei es auch für $0 < \sqrt{2}\,\varphi_e \leq 90°$ brauchbare Lösungen gibt. Einige von den vielen berechneten

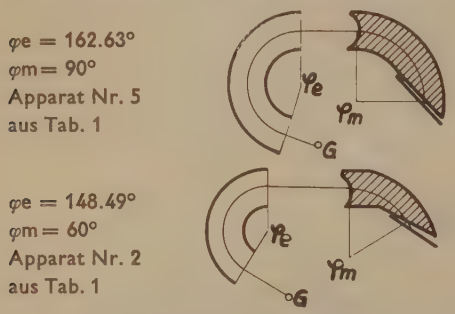

Abb. 8. Zwei Beispiele für Massenspektrographen mit Doppelfokussierung erster Ordnung für alle Massen entlang einer geraden Photoplatte, bei denen in der Mitte der Photoplatte gleichzeitig die von α^2 und $\alpha\beta$ abhängigen Bildfehler korrigiert sind. (Gleichsinnige Ablenkung.)

Lösungen sind in Tabelle 2 zusammengestellt. Wie man aus der Tabelle ersieht, besitzen die Lösungen für φ_m um 100° grosse ε' und ε''. Um

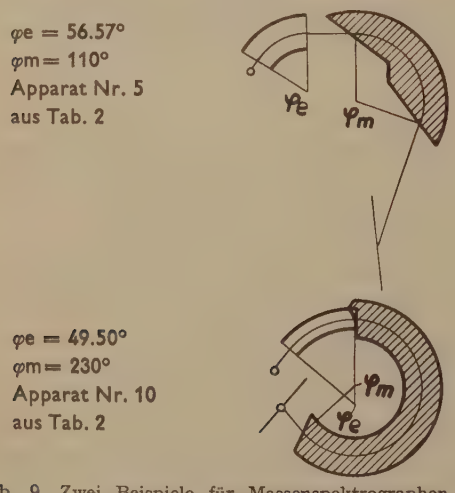

Abb. 9. Zwei Beispiele für Massenspektrographen mit Doppelfokussierung erster Ordnung für alle Massen entlang einer geraden Photoplatte, bei denen in der Mitte der Photoplatte gleichzeitig die von $\alpha\beta$ und β^2 abhängigen Bildfehler korrigiert sind. (Gleichsinnige Ablenkung.)

zu vernünftig grossen ε zu kommen, muss man Apparate mit grossen φ_m wählen. (Siehe Abb. 9.)

(*c*) *Apparate mit* $B_{11} = B_{12} = B_{22} = 0$ (*Vollständige Doppelfokussierung zweiter Ordnung*)

In Tabelle 3 sind einige von vielen berechneten Apparaten mit vollständiger Doppelfokussierung zweiter Ordnung zusammengestellt. Man sieht, dass keiner der angegebenen Apparate ideale Eigenschaften besitzt. Als besonders unangenehm erscheint die Grösse des Radialfeldes. (Siehe Abb. 10.)

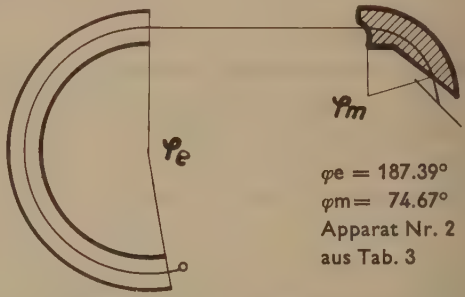

Abb. 10. Beispiel für einen Massenspektrographen mit Doppelfokussierung erster Ordnung für alle Massen entlang einer geraden Photoplatte, bei dem in der Mitte der Photoplatte gleichzeitig die von α^2, $\alpha\beta$ und β^2 abhängigen Bildfehler korrigiert sind. (Gleichsinnige Ablenkung.)

5.2. GEGENSINNIGE ABLENKUNG

(*a*) *Apparate mit* $B_{11} = B_{12} = 0$, $B_{22} \neq 0$

Auch für gegensinnige Ablenkung gelang es nicht, in dem Bereich $0 < \sqrt{2}\,\varphi_e \leq 90°$ physikalisch brauchbare Lösungen zu finden. Von den für $180° < \sqrt{2}\,\varphi_e \leq 270°$ gefundenen Lösungen sind einige in Tabelle 4 zusammengestellt. Wie man sieht, sind die Abmessungen der durch sie gegebenen Apparate zum Teil recht vernünftig. (Siehe Abb. 11.)

(*b*) *Apparate mit* $B_{12} = B_{22} = 0$, $B_{11} \neq 0$

Die Möglichkeit zur gleichzeitigen Korrektur der beiden von β abhängigen Bildfehler zweiter Ordnung bei Massenspektrographen mit Doppelfokussierung erster Ordnung längs einer geraden Bildkurve ist für den Spezialfall des Mattauch-Herzogschen Apparates ($\varphi_m = 90°$, $\sqrt{2}\,\varphi_e = 45°$, gegensinnige Ablenkung) zuerst von Robinson[7]) angegeben worden. Zu einer weiteren Kontrolle unserer allgemeineren Berechnungen haben wir ebenfalls die Korrekturmöglichkeiten von B_{12} und B_{22} fur Apparate dieses Typs unter-

sucht. Während Robinson d/r_m vorgibt, benutzten wir jedoch r_m/R' als unabhängige Veränderliche, so dass wir nicht dieselben Beispiele wie Robinson berechneten. Unsere Ergebnisse passen jedoch recht gut zu jenen von Robinson.

Neben dem Mattauch-Herzog-Robinsonschen Fall haben wir noch viele andere Apparate mit korrigiertem von β abhängigen Bildfehler berechnet. In Tabelle 6 sind einige Ergebnisse zusammengestellt. Wie im Falle gleichsinniger Ablenkung besitzen die Apparate mit $B_{12} = B_{22} = 0$, $B_{11} \neq 0$ besonders angenehme Abmessungen. (Siehe Abb. 12.)

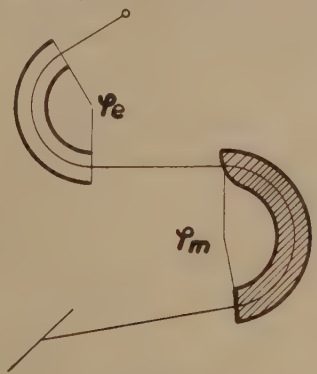

Abb. 11. Zwei Beispiele für Massenspektrographen mit Doppelfokussierung erster Ordnung für alle Massen entlang einer geraden Photoplatte, bei denen in der Mitte der Photoplatte gleichzeitig die von α^2 und $\alpha\beta$ abhängigen Bildfehler korrigiert sind. (Gegensinnige Ablenkung.)

(c) *Apparate mit vollständiger Doppelfokussierung zweiter Ordnung*

Auch im Falle der gegensinnigen Ablenkung lassen sich von zweiter Ordnung in einem Punkt vollständig doppelfokussierende Apparate mit Doppelfokussierung erster Ordnung für alle Massen längs einer geraden Bildkurve angeben. Einige von vielen gerechneten Beispielen sind in Tabelle 7 zusammengestellt. Für eine praktische Ausführung liegt Lösung Nr. 4 am günstigsten. (Siehe Abb. 13).

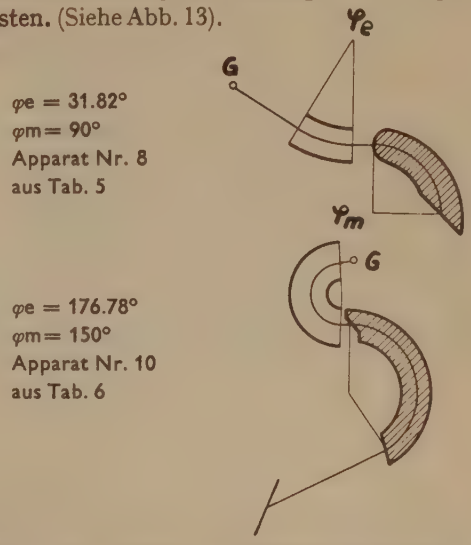

Abb. 12. Zwei Beispiele für Massenspektrographen mit Doppelfokussierung erster Ordnung für alle Massen entlang einer geraden Photoplatte, bei denen in der Mitte der Photoplatte gleichzeitig die von $\alpha\beta$ und β^2 abhängigen Bildfehler korrigiert sind. (Gegensinnige Ablenkung.)

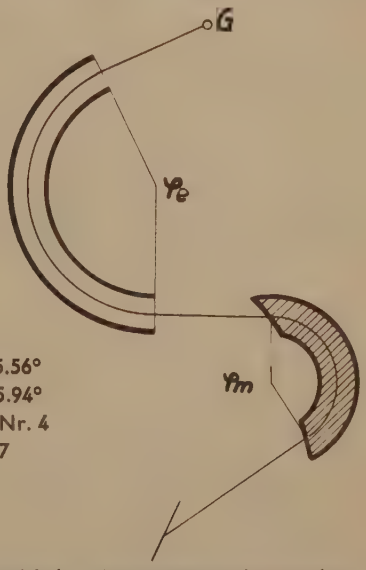

Abb. 13. Beispiel für einen Massenspektrographen mit Doppelfokussierung erster Ordnung für alle Massen entlang einer geraden Photoplatte, bei dem in der Mitte der Photoplatte gleichzeitig die von α^2, $\alpha\beta$ und β^2 abhängigen Bildfehler korrigiert sind. (Gegensinnige Ablenkung.)

TABELLE 1

Nr.	φ_m	ε'	ε''	$\frac{r_m}{R'}$	$\sqrt{2}\,\varphi_e$	φ_e	$\frac{d}{r_m}$	$\frac{r_e}{r_m}$	$\frac{l'_e}{r_m}$	$\frac{l''_m}{r_m}$	B_{22}
1	60	— 17.63	— 60	— 1.000	210	148.49	1.938	1.119	1.370	0.159	— 1.107
2	60	— 17.63	— 60	— 4.000	210	148.49	1.219	0.635	0.778	0.159	— 1.153
3	90	4.76	— 45	— 0.750	230	162.63	1.272	1.323	0.785	0.077	— 1.993
4	90	4.76	— 45	— 1.000	230	162.63	1.224	1.236	0.733	0.077	— 2.031
5	90	4.76	— 45	— 4.000	230	162.63	0.886	0.778	0.462	0.077	— 2.191
6	90	12.67	— 45	— 1.000	240	169.71	1.157	1.331	0.543	0.184	— 1.939
7	90	12.67	— 45	— 4.000	240	169.71	0.817	0.810	0.331	0.184	— 2.103
8	100	16.34	— 40	— 0.500	250	176.78	1.027	1.478	0.380	0.102	— 2.048
9	100	16.34	— 40	— 1.000	250	176.78	0.961	1.275	0.328	0.102	— 2.182
10	100	16.34	— 40	— 3.000	250	176.78	0.775	0.896	0.231	0.102	— 2.380

Tab. 1. Massenspektrographen mit gleichsinniger Ablenkung im elektrischen und magnetischen Feld, bei denen für alle Massen entlang einer geraden Bildkurve Doppelfokussierung erster Ordnung erfolgt und für die in einem Punkt der Bildkurve die beiden von α abhängigen Bildfehler zweiter Ordnung verschwinden ($B_{11} = B_{12} = 0$; siehe auch Abb. 8). Alle Winkel sind in Grad angegeben.

TABELLE 2

Nr.	φ_m	ε'	ε''	$\frac{r_m}{R'}$	$\sqrt{2}\,\varphi_e$	φ_e	$\frac{d}{r_m}$	$\frac{r_e}{r_m}$	$\frac{l'_e}{r_m}$	$\frac{l''_m}{r_m}$	B_{11}
1	110	— 56.44	— 35.00	0	50	35.36	2.584	1.441	0.855	2.178	3.666
2	110	— 59.39	— 35.00	0	70	49.50	2.105	0.754	0.194	1.950	1.517
3	110	— 60.08	— 35.00	0	80	56.57	2.064	0.544	0.068	1.903	1.173
4	110	— 59.39	— 35.00	— 0.25	70	49.50	0.366	1.662	0.428	1.950	4.898
5	110	— 60.08	— 35.00	— 0.25	80	56.57	0.732	0.883	0.110	1.903	1.964
6	130	— 50.47	— 25.00	0	60	42.43	3.578	1.835	0.749	2.107	2.721
7	150	— 45.41	— 15.00	— 0.25	80	56.57	0.534	2.339	0.292	1.840	3.029
8	170	— 38.28	— 5.00	— 0.25	80	56.57	0.097	3.827	0.477	1.599	3.071
9	210	— 25.57	15.0	— 1.00	80	56.57	0.057	1.475	0.184	0.840	1.788
10	230	— 18.91	25.0	— 2.00	70	49.50	0.015	1.251	0.322	0.470	2.072

Tab. 2. Massenspektrographen mit gleichsinniger Ablenkung im elektrischen und magnetischen Feld, bei denen für alle Massen entlang einer geraden Bildkurve Doppelfokussierung erster Ordnung erfolgt und für die in einem Punkt der Bildkurve die beiden von β abhängigen Bildfehler zweiter Ordnung verschwinden ($B_{12} = B_{22} = 0$; siehe auch Abb. 9).

TABELLE 3

Nr.	φ_m	ε'	ε''	$\frac{r_m}{R'}$	$\sqrt{2}\,\varphi_e$	φ_e	$\frac{d}{r_m}$	$\frac{r_e}{r_m}$	$\frac{l'_e}{r_m}$	$\frac{l''_m}{r_m}$
1	71.66	25.88	— 54.17	— 4.000	245	173.24	4.308	2.132	0.703	0.414
2	74.67	31.14	— 52.67	— 4.000	265	187.39	3.217	1.783	0.110	0.442
3	76.36	29.77	— 51.82	— 3.000	265	187.39	4.623	2.530	0.157	0.429
4	89.05	15.99	— 45.47	0.400	245	173.24	0.820	4.255	1.403	0.233
5	90.00	11.27	— 45.00	0.600	238	168.29	0.738	3.803	1.680	0.166

Tab. 3. Massenspektrographen mit gleichsinniger Ablenkung im elektrischen und magnetischen Feld, bei denen für alle Massen entlang einer geraden Bildkurve Doppelfokussierung erster Ordnung erfolgt und für die in einem Punkt der Bildkurve alle drei Bildfehler korrigiert sind (vollständige Doppelfokussierung zweiter Ordnung für eine Masse, $B_{11} = B_{12} = B_{22} = 0$; siehe auch Abb. 10).

TABELLE 4

Nr.	φ_m	ε'	ε''	$\frac{r_m}{R'}$	$\sqrt{2}\,\varphi_e$	φ_e	$\frac{d}{r_m}$	$\frac{r_e}{r_m}$	$\frac{l'_e}{r_m}$	$\frac{l''_m}{r_m}$	B_{22}
1	70	—60.96	—55	1.00	190	134.35	1.406	0.303	1.216	3.619	—0.248
2	90	—59.64	—45	0.75	210	148.49	0.298	0.757	0.927	2.414	2.802
3	110	—50.82	—35	0.75	210	148.49	0.966	0.958	1.173	2.838	1.086
4	170	—23.93	— 5	0.75	210	148.49	2.611	1.442	1.766	2.981	—2.346
5	170	—23.93	— 5	2.00	210	148.49	1.725	0.886	1.085	2.981	—2.460
6	190	—15.04	+ 5	2.00	210	148.49	1.940	0.948	1.161	2.633	—2.999
7	190	—15.04	+ 5	3.00	210	148.49	1.609	0.778	0.953	2.633	—3.006
8	190	—24.62	+ 5	1.00	230	162.63	1.920	1.394	0.827	1.658	—2.944
9	190	—24.62	+ 5	2.00	230	162.63	1.415	1.024	0.608	1.658	—2.944
10	190	—24.62	+ 5	3.00	230	162.63	1.173	0.848	0.503	1.658	—2.945

Tab. 4. Massenspektrographen mit gegensinniger Ablenkung im elektrischen und magnetischen Feld, bei denen für alle Massen entlang einer geraden Bildkurve Doppelfokussierung erster Ordnung erfolgt und für die in einem Punkt der Bildkurve die beiden von α abhängigen Bildfehler zweiter Ordnung verschwinden ($B_{11} = B_{12} = 0$; siehe auch Abb. 11).

TABELLE 5

Nr.	$\frac{r_m}{R'}$	$\frac{d}{r_m}$	$\frac{r_e}{r_m}$	$\frac{l'_e}{r_m}$	B_{11}
1	1.5	3.559	2.730	1.930	3.280
2	2.0	1.628	2.412	1.706	4.326
3	2.5	1.009	2.184	1.545	4.995
4	3.0	0.711	2.011	1.422	5.461
5	3.5	0.539	1.873	1.325	5.803
6	4.0	0.427	1.761	1.245	6.066
7	4.5	0.350	1.666	1.178	6.273
8	5.0	0.293	1.585	1.121	6.441

Tab. 5. Massenspektrographen mit gegensinniger Ablenkung im elektrischen und magnetischen Feld, bei denen für alle Massen entlang einer geraden Bildkurve Doppelfokussierung erster Ordnung erfolgt und für die in einem Punkt der Bildkurve die beiden von β abhängigen Bildfehler zweiter Ordnung verschwinden ($B_{12} = B_{22} = 0$; siehe Abb. 12). Für die Apparate dieser Tabelle ist $\varphi_m = 90°$, $\varepsilon' = 0$, $\varepsilon'' = -45°$, $\sqrt{2}\,\varphi_e = 45°$ und $l''_m = 0$. Die hier angegebenen Lösungen passen recht gut zu den von Robinson mitgeteilten Lösungen dieses Typs.

TABELLE 6

Nr.	φ_m	ε'	ε''	$\frac{r_m}{R'}$	$\sqrt{2}\,\varphi_e$	φ_e	$\frac{d}{r_m}$	$\frac{r_e}{r_m}$	$\frac{l'_e}{r_m}$	$\frac{l''_m}{r_m}$	B_{11}
1	90	9.00	—45	3.00	55	38.89	0.743	1.506	0.746	0.137	2.638
2	90	15.73	—45	3.00	65	45.96	0.652	1.113	0.367	0.220	1.608
3	90	20.10	—45	3.00	75	53.03	0.613	0.799	0.151	0.268	1.111
4	90	22.24	—45	3.00	85	60.10	0.658	0.556	0.034	0.290	0.861
5	90	9.00	—45	4.00	55	38.89	0.501	1.294	0.641	0.137	2.777
6	90	15.73	—45	4.00	65	45.96	0.478	0.954	0.314	0.220	1.643
7	90	20.10	—45	4.00	75	53.03	0.478	0.686	0.130	0.268	1.120
8	90	22.24	—45	4.00	85	60.10	0.530	0.479	0.030	0.290	0.864
9	130	—51.90	—25	0	250	176.78	0.374	0.210	0.054	2.002	1.273
10	150	—44.42	—15	0	250	176.78	0.162	0.404	0.104	1.904	1.442
11	150	—32.90	—15	—2.00	210	148.49	1.973	0.329	0.403	3.139	6.432
12	170	—23.93	— 5	—4.00	210	148.49	1.509	0.239	0.293	2.981	6.627
13	190	—24.62	+ 5	—2.00	230	162.63	1.290	0.149	0.088	1.658	2.413
14	190	—24.62	+ 5	—4.00	230	162.63	0.889	0.103	0.061	1.658	2.413

Tab. 6. Weitere Massenspektrographen mit gegensinniger Ablenkung im elektrischen und magnetischen Feld, bei denen für alle Massen entlang einer geraden Bildkurve Doppelfokussierung erster Ordnung erfolgt und für die in einem Punkt der Bildkurve die beiden von β abhängigen Bildfehler zweiter Ordnung verschwinden ($B_{12} = B_{22} = 0$; siehe auch Abb. 12).

TABELLE 7

Nr.	φ_m	ε'	ε''	$\frac{r_m}{R'}$	$\sqrt{2}\,\varphi_e$	φ_e	$\frac{d}{r_m}$	$\frac{r_e}{r_m}$	$\frac{l'_e}{r_m}$	$\frac{l''_m}{r_m}$
1	60.00	— 65.78	— 60.00	0.75	190	134.35	1.107	0.283	1.133	2.902
2	72.50	— 59.75	— 53.75	0.40	190	134.35	1.944	0.542	2.174	3.801
3	123.75	— 42.57	— 28.13	0.50	205	144.96	1.898	1.328	2.014	3.434
4	145.94	— 38.78	— 17.03	0.40	220	155.56	1.744	1.961	1.652	2.571
5	151.72	— 43.03	— 14.14	0.5	245	173.24	1.241	1.757	0.579	1.941
6	165.83	— 40.02	— 7.08	0	265	187.39	2.672	5.150	0.319	1.643

Tab. 7. Massenspektrographen mit gegensinniger Ablenkung im elektrischen und magnetischen Feld, bei denen für alle Massen entlang einer geraden Bildkurve Doppelfokussierung erster Ordnung erfolgt und für die in einem Punkt der Bildkurve alle drei Bildfehler korrigiert sind (vollständige Doppelfokussierung zweiter Ordnung für eine Masse; $B_{11} = B_{12} = B_{22} = 0$; siehe auch Abb. 12).

Zum Schluss möchten wir Herrn Professor Mattauch für die Bereitstellung der finanziellen Mittel zur Durchführung der Rechnung aufrichtig danken. Ferner danken wir Fräulein Braum und Fräulein Walter für die Durchführung der Kontrollrechnungen auf der Tischrechenmaschine.

NUCLEAR INSTRUMENTS 3 (1958) 149–157; NORTH-HOLLAND PUBLISHING CO. – AMSTERDAM

COLLIMATOR PENETRATION AND SCATTERING EFFECTS

R. A. HEFFERLIN† and W. E. KREGER

U. S. Naval Radiological Defense Laboratory San Francisco 24, California

Received 13 May 1958

The type of lead collimator usually used for gamma-ray spectrometers covering the energy range up to 1 MeV has been found essentially free from scattering; hence, the effective collimator aperture to gamma radiation in certain source-collimator geometries can be calculated according to the theory of Mather[2]). The same quantity for a combination of source collimator and detector collimator can likewise be calculated as if the combination were replaced by a continuous collimator of the same total length; providing the units are at least 4 inches and 6 inches long, respectively.

1. Introduction

In measuring the spectrum of gamma or X-radiation from a radioactive source, either distributed in space or existing at some point in space, or in a gamma penetration experiment, it is often desirable or necessary to collimate the incoming radiation before it impinges on the detector (a scintillation crystal such as NaI(Tl)). However, since no collimator material is perfectly non-scattering and opaque to gamma rays, radiation can reach the detector from directions different from the collimator axis direction, and similarly, the radiation aperture of the collimator is not necessarily the geometrical aperture.

Collimator penetration by, and scattering of gamma radiation are both energy dependent processes. Hence, any type of collimated gamma-ray spectroscopy will require the application of an energy dependent relative aperture correction which must be known before the source spectrum can be determined from the measured detector pulse height spectrum. For such reasons it is desirable to study further the behavior of the typical lead gamma-ray collimator, and to determine the effective aperture of the collimator for gamma radiation.

The problem has been discussed for a special case by Kellershohn and Pellerin[1]) and for several types of cases by Mather[2]). The former investigators consider only the penetration effect; the latter discusses also the scattering effects and treats both in a theoretical manner. The results of the theory are expressed in terms of "aperture", which is defined as

$$\text{Aperture} = \frac{\text{(incident photons/sec) measured with collimator}}{\text{(incident photons/sec cm}^2\text{) at center of gravity of collimator}} \quad (1)$$

It was considered desirable to make some measurements on collimator systems to verify the results of the theoretical treatment. The measurements to be described in this paper cover a special case of a collimator system, as well as the general case which has also been studied somewhat differently by Tomnovec and Mather[3]). In the special case, the collimator was effectively lengthened and its angular resolution for an extended source gamma radiation field was improved by the addition of a length of collimator near the source of the radiation field. It is the purpose of the experiment to study collimator properties and, in particular, scattering apertures for a variety of collimators and of source positions. This will be done, in general, by measuring total aperture and subtracting the geometrical (definition) and penetration (theory[2])) apertures.

† Permanent address: Southern Missionary College, Collegedale, Tennessee.

[1]) C. Kellershohn and P. Pellerin, J. Phys. et Radium 17 (1956) 81A (Supplement to No. 6).

[2]) R. L. Mather, J. Appl. Phys. 28 (1957) 1200.

[3]) F. M. Tomnovec and R. L. Mather, J. Appl. Phys. 28 (1957) 1208.

2. Experiment

The experimental determination of apertures consists of a series of measurements which give the numerator of eq. (1), and of calculations, based on source strength, which are necessary to give the denominator.

The source consists of a bundle of seven, 0.010 in. diameter Co^{60} wires, 1/8 in. long, stuffed horizontally into the end of a 32 mil diameter hole in a piece of lucite about 3/16 in. square and one inch long. The lucite piece is supported on its lower end by the upper end of a toothed rack, which in turn is part of a system allowing careful positioning of the source axis (parallel to the collimator axis) in the plane perpendicular to the axis of the collimator system. This type of source is the result of an effort to obtain a sufficiently strong source in a sufficiently small volume of space, and to avoid self-absorption. Self-absorption was observed (by measuring flux as the source was rotated) on an alternative source, a 5/8 in. length of the same wire, with the long axis of the wire toward the detector; self-absorption was not observed in the above source using the same type of check.

The source activity was measured as a step in this experiment, using a scintillation counter in several different geometries. Knowing the source strength (2.6 mC) one can compute the denominator of eq. (1).

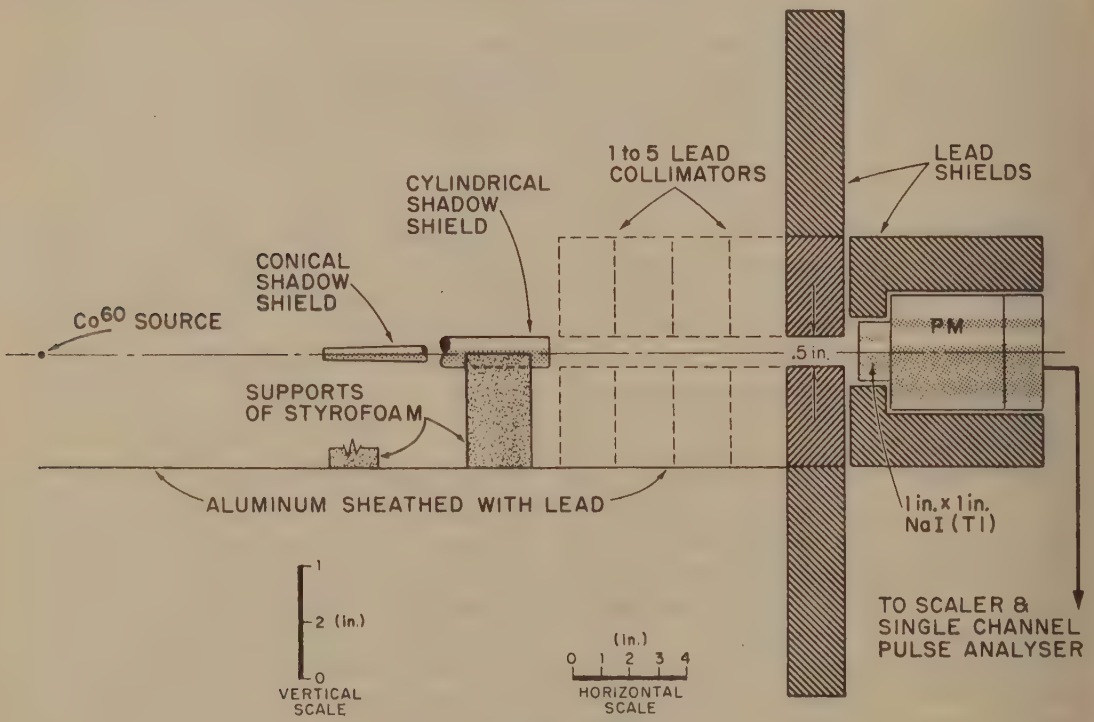

Fig. 1. Collimator experiment.

The measurements of the number of incident photons/sec are made with a 1 in. by 1 in. NaI(Tl) crystal scintillation detector. The detector output feeds either a scaler or a recording single channel analyzer system. The source holder, the detector, and the collimators, shown in fig. 1, are all mounted on an aluminium frame, part of which is sheathed with lead sheet to minimize scattering. There is still some scattering from this table, and it is necessary to measure its magnitude and that of the background by the use of an appropriate shadow shield.

Two shadow shields are employed:

1. A truncated conical shield, whose effective apex is the source and whose effective base is the crystal end of the collimator, is used. This shield exactly and only eliminates the direct rays from source to crystal. The fact that the source is not *exactly* a point means that, for a position where the nearer end of the source is at the apex of the cone, *some* direct rays will arrive at the crystal; the contribution due to this was calculated and a correction is applied where necessary. This shadow shield was aligned very accurately by optical means.

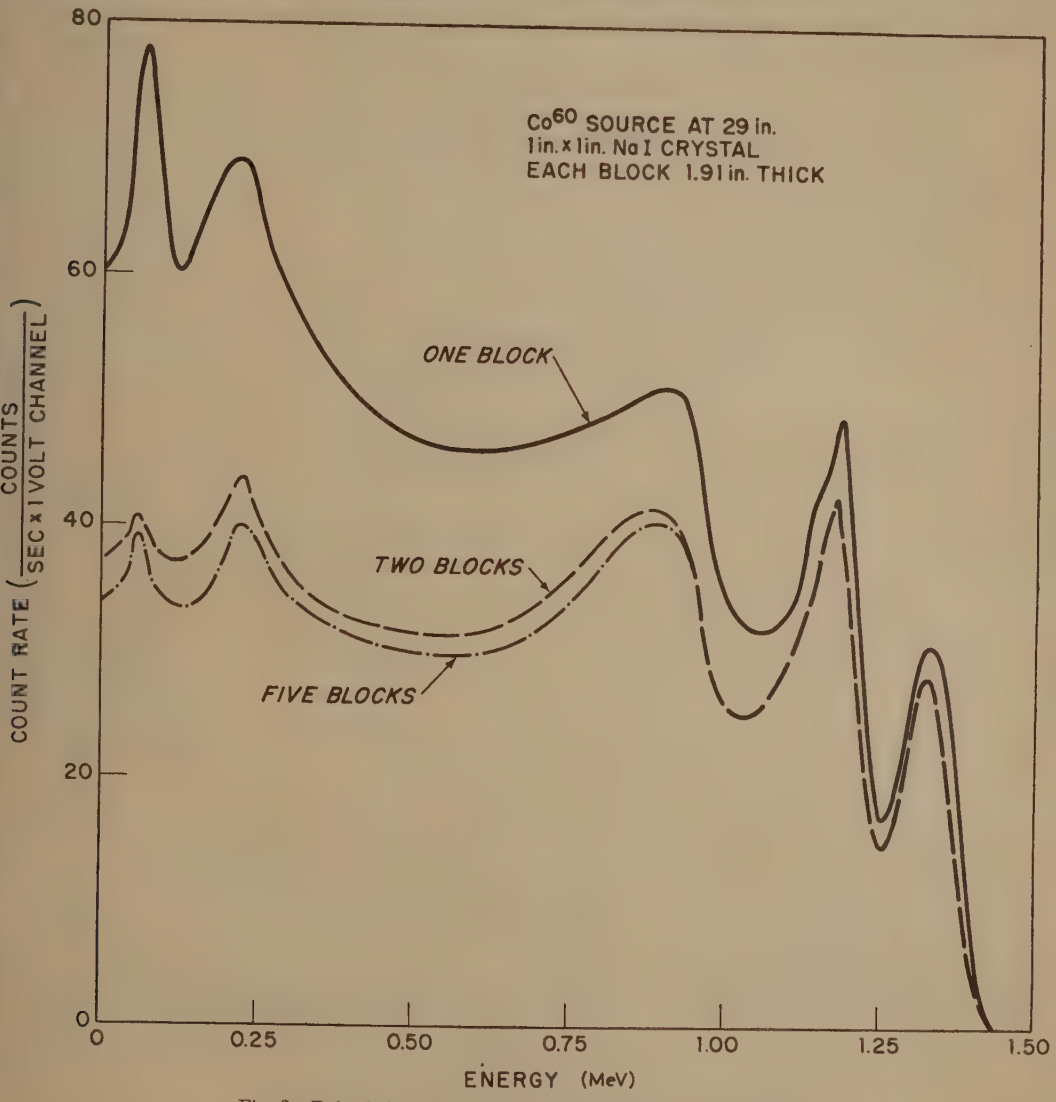

Fig. 2. Pulse height spectra for various collimator thicknesses.

2. The other shield used is a cylinder, which allows only the background and those rays scattering off the table (and which are not intercepted by the cone) to be detected.

These shields are either mounted on small

foam plastic blocks or are supported by wires.

The crystal and photomultiplier are protected from background and large angle scattering by a large lead slab and by a cylindrical lead cover. The photomultiplier is, in addition, shielded by a μ-metal cover.

An integral count is taken for foreground, cone shield-in and cylinder shield-in for several collimator geometries. The spectrum exhibited a large noise level below 2 volts pulse height, so the integral count was taken with a 2 volt threshold. The integral count was then corrected to effectively zero volts threshold.

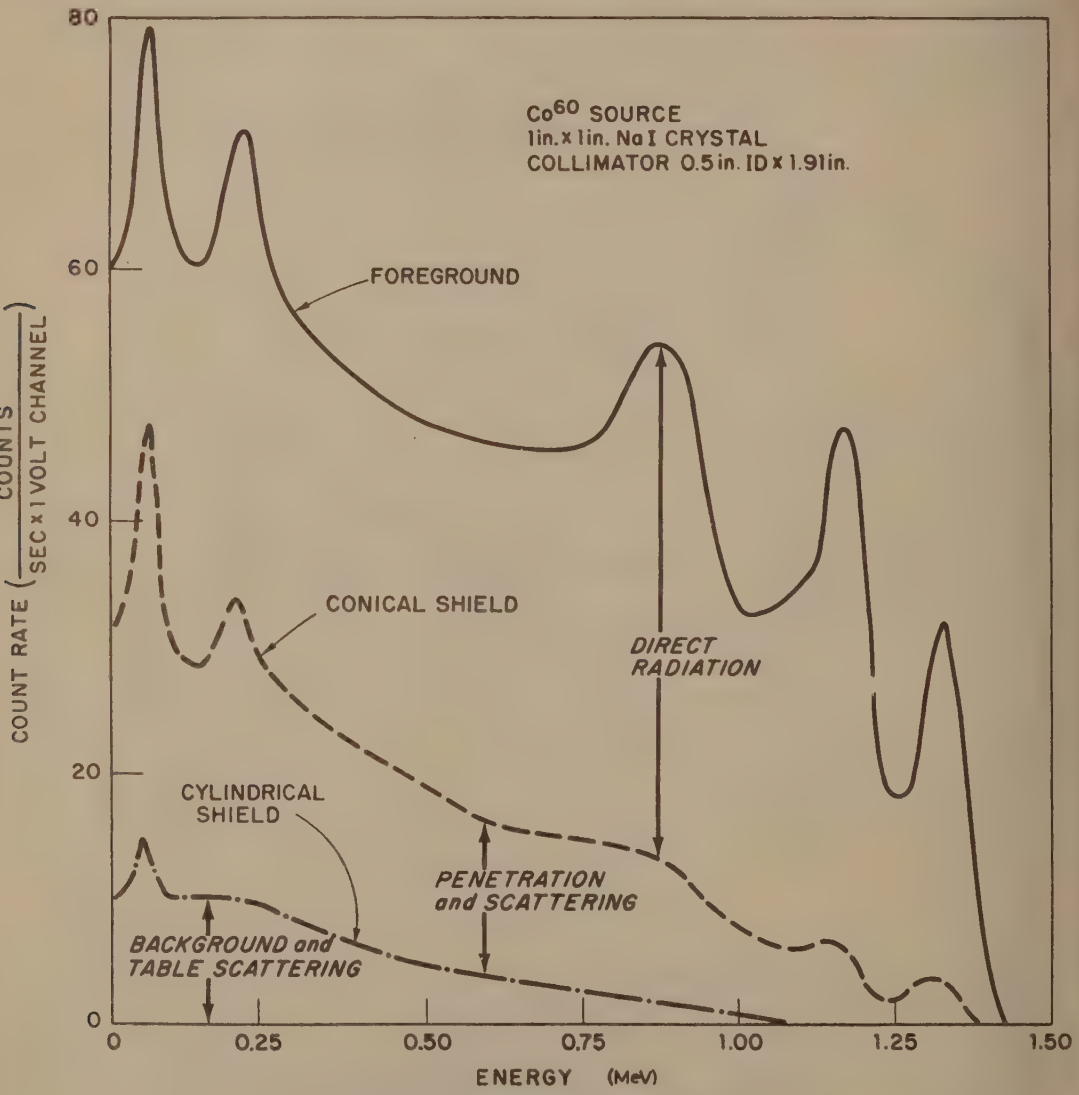

Fig. 3. Pulse height spectra with and without shadow shields.

In order to convert counts into incident photons it is necessary to apply the crystal efficiency correction. The following procedure was used:

1. The efficiency was calculated for each case

using the product of two factors, the $1 - \exp(-\mu' x')$ factor and the solid angle factor. μ' is the NaI total absorption coefficient at the average radiation energy of 1.25 MeV. x' is the axial thickness of the NaI crystal.

2. The above calculation was compared with the tables[4]) for those values of source position which allowed comparison. This comparison shows that the calculation was adequate for the cases to which it was applied.

It is worthwhile to review the corrections which have been considered before discussing the application of the data.

1. Correction of count because of loss below threshold.

2. Dead-time.

3. Radiation past edge of cone.

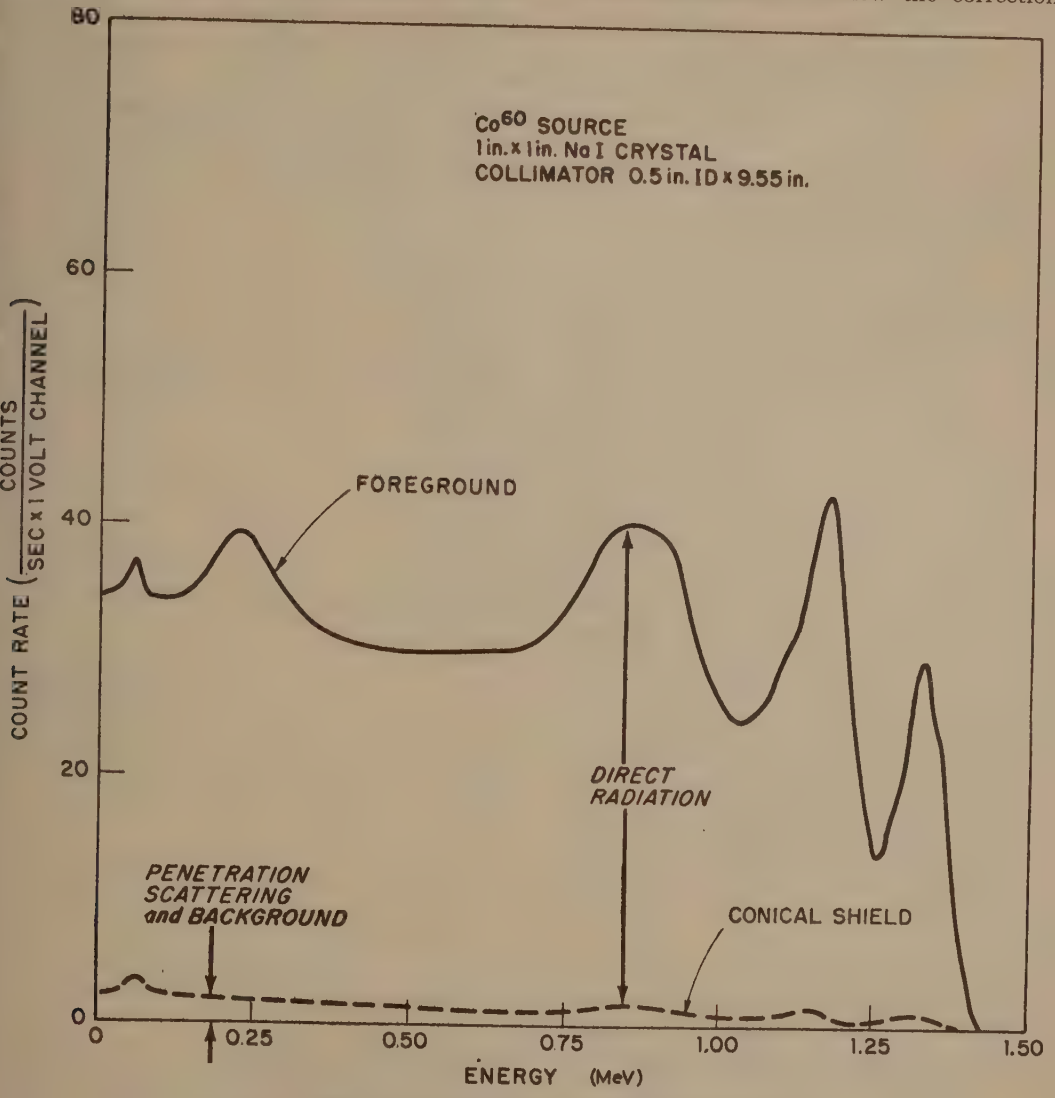

Fig. 4. Pulse height spectra with and without shadow shields.

[4]) Personal communication by R. L. Mather.

4. Error in using inverse square crystal correction (neglect).

5. Absorption and scattering of mountings (neglect).

6. Self-absorption of source (none).

7. Two energies of Co^{60} (average).

3. Results

Data were first taken to measure scattering aperture for the case of a point source on the axis of the lead collimator. These data also were used to determine source activity. Two lead shadow cones were made in such a manner that for 1/2 in. collimators the source could be at either 14 in. or 29 in. from the detector end of the collimator. For 3/4 in. collimators a distance of 21 in. was used.

Fig. 2 shows detector pulse height spectra for three different lengths of 1/2 in. diameter collimators with source at 29 in. The large excess of counts for one block over the 2 and 5 block cases is due to the "build up" of degraded radiation, most of which has passed completely through the two inch thick lead collimator block. These spectra have not had any background subtracted. Figs. 3 and 4 show detector pulse height spectra for two particular cases, with and without shadow shields, The Co^{60} peaks in the "penetration and scattering" spectrum are due to low angle scattering and to that fraction of the source which could see over the edge of the shield used (conical shield). The following subtractions of counts may now be made:

Foreground - Cone shield = direct gamma rays only (2)

Foreground - Cylinder shield = background and table scattering (3)

Cone shield - Cylinder shield = penetration and scattering in collimator bore (4)

An expression for the aperture for a point source on the collimator axis and data obtained using eq. (3) allow a determination of source activity. The photon flux at the center of the collimator is calculated and is corrected for inverse-square factor to yield activity. This determination was made with several different geometries and gave 2.6 mC $\pm$ 5 percent as the result.

Knowing the photon flux at the center of the collimator and using eqs. (4) and (1), one can obtain the aperture sum (penetration plus scattering). By subtracting the theoretically known penetration aperture, one obtains scattering aperture. A check on the calculations is desirable and is made possible by using eqs. (1) and (3) and subtracting aperture (geometrical plus penetration).

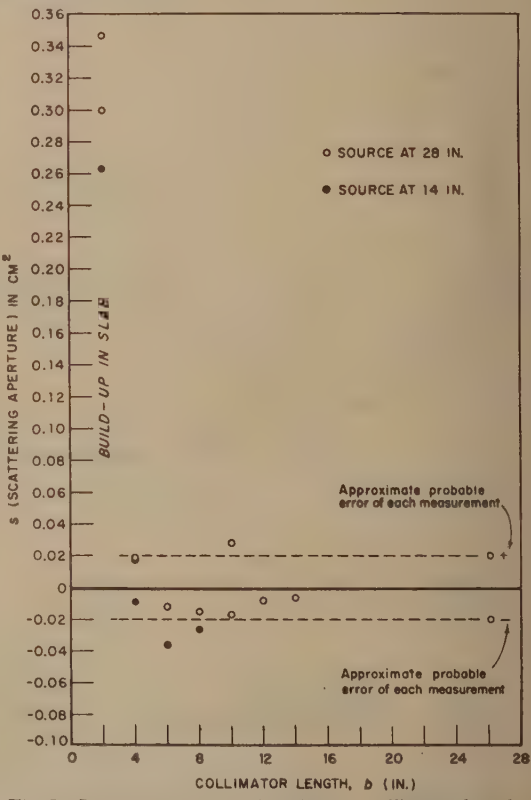

Fig. 5. Scattering aperture for different collimator lengths.

The results of these calculations are shown in fig. 5. It is seen that the scattering aperture is zero within the limits of experimental error with the exception of the case for one block. The large values in this case are due to radiation which penetrated the slab, and are in agreement with estimates based on tabulated build-up factors.

The theory indicates that for an infinitely distant source the scattering aperture is of the order of 10^{-6} of the geometrical aperture. One

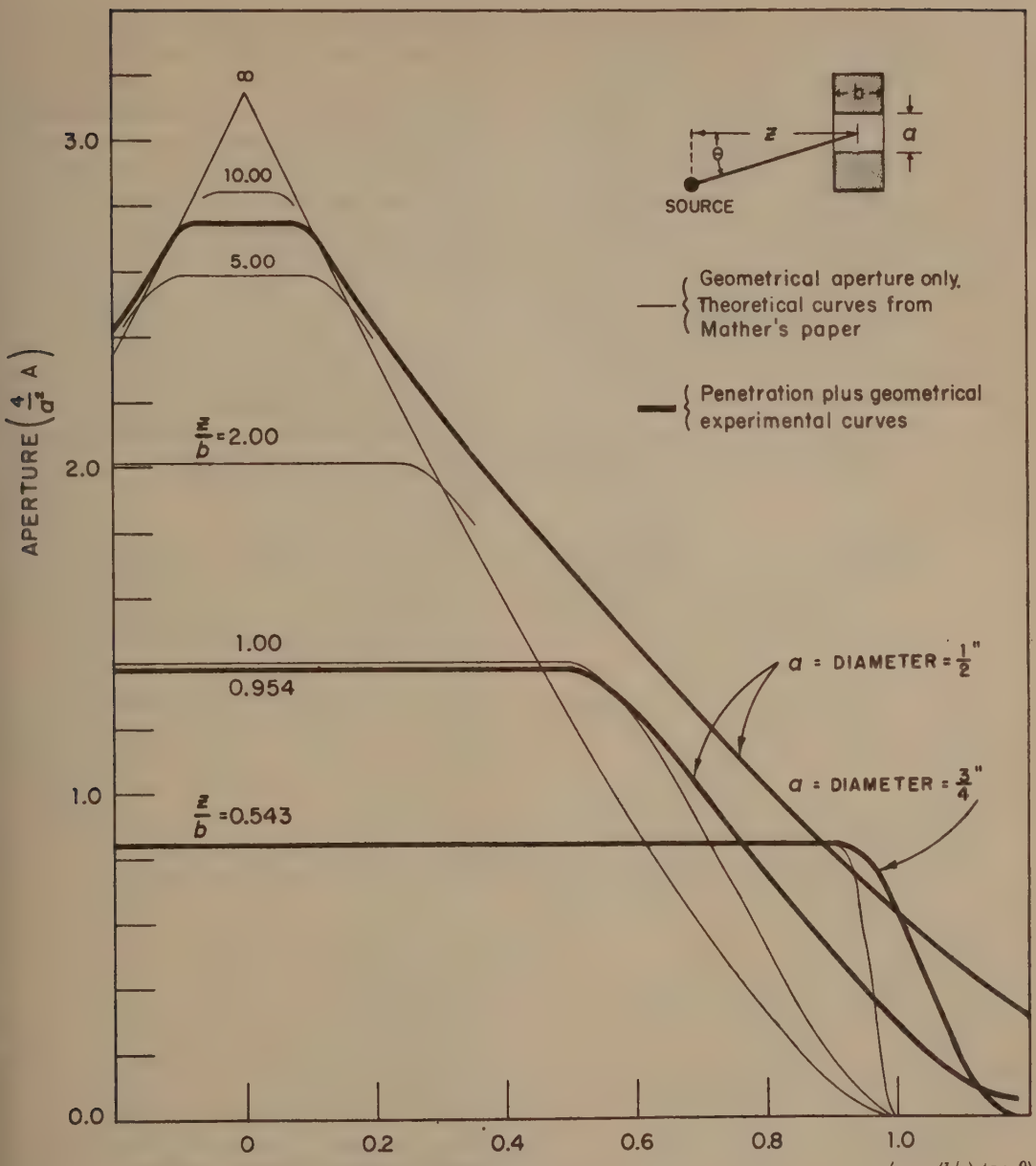

Fig. 6. Angular response to point source.

case with source at a finite distance was worked out[4]) for the source 58 in. from the center of, and on the axis of, a 1/2 in. by 8 in. lead collimator. For an energy of 1.25 MeV the scattering aperture was approximately 0.006 cm². It is seen that the data of fig. 5 are not inconsistent with this value.

It has, therefore, been shown experimentally that there are no significant scattering effects within the following ranges: (1) 0 ⩽ diameter ⩽ 1/2 in., (2) 14 in. ⩽ source to detector distance

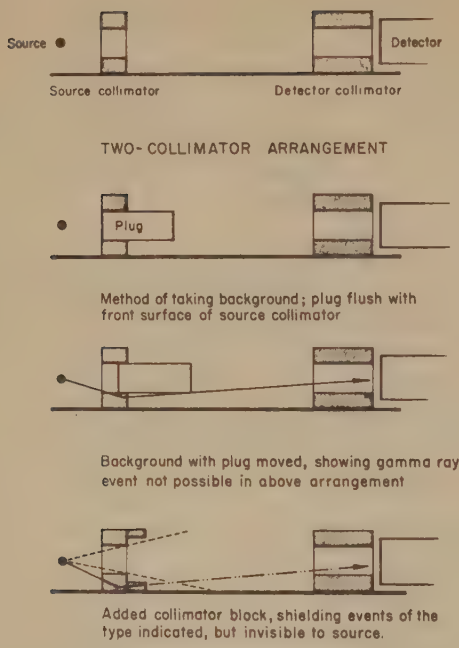
Source
Detector
Source collimator
Detector collimator
TWO-COLLIMATOR ARRANGEMENT
Plug
Method of taking background; plug flush with front surface of source collimator
Background with plug moved, showing gamma ray event not possible in above arrangement
Added collimator block, shielding events of the type indicated, but invisible to source.

Fig. 7. Two-collimator arrangement.

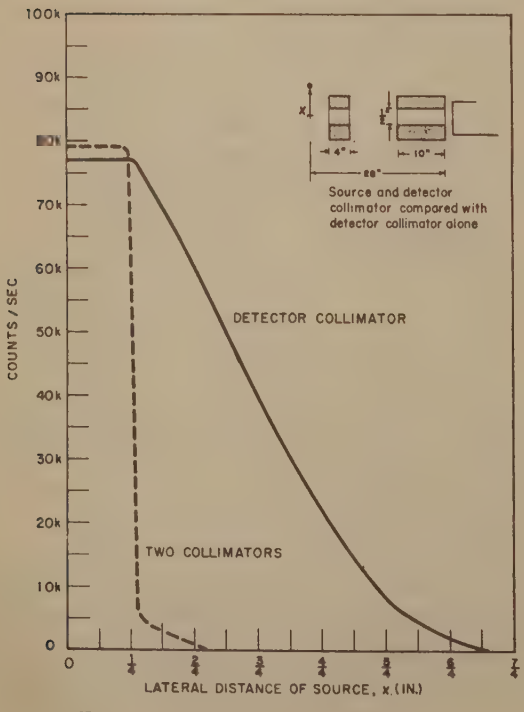

Fig. 8. Angular response to point source.

$\leqslant$ 28 in., (3) 4 in. $\leqslant$ collimator length $\leqslant$ 14 in., and (4) 1.1 MeV $\leqslant$ energy $\leqslant$ 1.3 MeV.

The dominant process with decreasing energy is the photoelectric effect rather than scattering effects; hence, no scattering effects would be expected for energies less than 1.2 MeV when they do not show up at 1.2 MeV.

Data were taken of the count rate by the crystal as the source was moved transverse to the axis of the collimator. Curves obtained for various geometries are shown in fig. 6, along with curves of geometrical aperture versus angle, as given by Mather. The difference between curves with the same value of z/b would give the aperture (penetration plus scattering) as the function of angle. By numerically integrating the first moment of such a curve one can arrive at the integrated aperture, which is defined as the integral of aperture over all source positions given in terms of polar coordinates. The theoretical (geometrical plus penetration) integrated aperture agrees with the experimental total integrated aperture which again leads to the conclusion that the scattering effect is negligible in the range of geometries considered. Therefore, the difference between experimental and theoretical curves in fig. 6 represents penetration aperture as a function of angle. Note that the curves in fig. 6 do not depend directly on the source position or on the collimator diameter.

The addition of a source collimator, as shown in figs. 7a and 7b markedly improves the angular resolution of the existing detector collimator for an extended source radiation field as shown for one case in fig. 8. Note that the response plateau is actually larger with the addition of the source collimator; and yet the measurements on scattering aperture indicate that this increment cannot be due to scattering from the bore of the source collimator. A series of experiments indicate that the increment is due to gamma-radiation entering the slab material of the first collimator and then scattering into the acceptance angle of the detector collimator.

The background was taken with a plug fitted into the source collimator, as indicated in fig. 7b. When the plug was moved to a position farther

back, as in fig. 7c, more of the slab volume was effective in scattering; the background count rose, and the net count decreased so that the plateau for the two collimators was then the same as for one.

It was shown experimentally that if the two collimator sections are sufficiently long the two-collimator arrangement behaves exactly like an uninterrupted collimator of the same total overall length.

4. Conclusions

Design of a satisfactory lead detector collimator for gamma energies up to 1.3 MeV involves a minimum length of 4 in. to prevent slab transmission. Otherwise, the geometry may be chosen to obtain a given angular resolution according to the considerations presented in fig. 6. Evidence has been presented that within the ranges stated in the results there is no appreciable scattering. Therefore, the aperture for a point source on the axis, or the integrated aperture for a distributed source, may be calculated according to the theory presented by Mather.

It has been shown that the aperture of a two-collimator arrangement may be calculated by assuming it to behave in the same manner as an uninterrupted collimator of the same total length if the proper kind of background is taken.

The authors wish to thank Dr. C. Sharp Cook for his suggestions and comments.

NUCLEAR INSTRUMENTS 3 (1958) 158–176; NORTH-HOLLAND PUBLISHING CO. – AMSTERDAM

MEASUREMENT OF CIRCULAR POLARIZATION OF γ-RAYS

HERWIG SCHOPPER

Institute of Nuclear Physics, Mainz

Received 2 May 1958

The various methods for the detection of circularly polarized γ-rays are surveyed, and detailed calculations of effects limiting the obtainable accuracy are communicated.

1. Introduction

The measurement of the circular polarization of γ-rays gives significant information in those experiments in which the detection of a screw sense is of relevance. This is obvious as the circular polarization together with the direction of propagation of the quanta defines a screw sense. Thus the sign of the magnetic moment of an excited state can be found by measuring the circular polarization of γ-rays emitted by nuclei polarized in a magnetic field[1]). If the circular polarization of γ-rays following the capture of a polarized neutron is measured the spins and parities of nuclear states can be determined[2]).

The detection of the circular polarization of γ-rays became of extreme importance after the discovery of non-conservation of parity for weak interactions as the non-invariance under space reflection is equivalent to the existence of a preferred screw sense (or helicity) in physical nature. Lee and Yang[3]) pointed out that in case of parity violation a γ-radiation following a β-decay is expected to be circularly polarized if emitted parallel or antiparallel to the electron. This supposition was verified experimentally for a number of β-decays[4–7]), and important conclusions about the nature of β-interactions could be obtained[8]). In particular it could be shown by this method that the violation of the invariance under space reflection is maximum within an experimental error of about 5%[9]). This type of experiment is also very useful for nuclear spectroscopy as the degree of polarization depends on the spins and multipolarities involved in the β- and γ-transition[10]). Another consequence of parity violation is the longitudinal polarization of β-particles. This was confirmed directly by different methods[8]). If longitudinally polarized electrons are stopped in an absorber they are expected to excite a circularly polarized external bremsstrahlung. This polarization was indeed found and gives indirect information about the electron polarization[11, 5]). But also the inner bremsstrahlung

[1]) J. C. Wheathly, W. J. Huiskamp, A. N. Diddens, M. J. Steenland and H. A. Tolhoek, Physica **21** (1955) 841; W. J. Huiskamp, Thesis (Leiden, 1958).

[2]) G. Trumpy, Nuclear Physics **2** (1956) 664.

[3]) T. D. Lee, and C. N. Yang, Phys. Rev. **104** (1956) 254.

[4]) H. Schopper, Phil. Mag. **2** (1957) 710; H. Appel and H. Schopper, Zeitschr. f. Phys. **149** (1957) 103.

[5]) F. Boehm and A. H. Wapstra, Phys. Rev. **106** (1957) 1364; **107** (1957) 1202); **107** (1957) 1462.

[6]) A. Lundby, A. P. Patro and J. P. Stroot, Nuovo Cimento **6** (1957) 745.

[7]) P. Debrunner and W. Kündig, Hel. Phys. Ac. **30** (1957) 261; J. Berthier, P. Debrunner, W. Kündig and B. Zwahlen, Hel. Phys. Ac. **30** (1957) 483.

[8]) cp. O. R. Frisch and T. H. R. Skyrme, Progr. Nucl. Physics **6** (1957) 267; Proceedings of the Rehovoth Conference on Nuclear Structure (North-Holland Publishing Co. Amsterdam, 1958) 336–418; H. Schopper, Fortschritte der Physik, **5** (1957) 581.

[9]) H. Appel, H. Schopper and S. D. Bloom, Phys. Rev. **109** (1958) 2211.

[10]) K. Alder, B. Stech and A. Winther, Phys. Rev. **107** (1957) 728; M. Morita and R. S. Morita, Phys. Rev. **107** (1957) 1729.

[11]) M. Goldhaber, L. Grodzins and A. W. Sunyar, Phys. Rev. **106** (1957) 826.

accompanying β-decay and K-capture should be circularly polarized if parity conservation is violated. This prediction was verified experimentally, too[12]).

If longitudinally polarized positrons are annihilated in flight the radiation emitted in forward direction is predicted to be circularly polarized. This provides a possibility to measure the positron polarization[13]).

The basic theory and the experimental arrangements suitable to measure the circular polarization of γ-rays were reviewed by Tolhoek[14]). However, in the light of the new development it was thought that a more comprehensive and detailed survey including some unpublished calculations and experimental experiences might be useful.

2. Possible Methods to Detect the Circular Polarization of γ-Rays

As mentioned above, the measurement of the circular polarization of γ-rays is equivalent to the detection of a screw sense. If one wants to find out whether a screw is left or right handed the simplest way is to compare the screw with a nut of a known screw sense.

In the case of γ-rays this can be done in two ways:

(a) interaction of γ-rays with polarized matter;

(b) transfer of the helicity of the γ-rays to secondary particles the polarization of which is measured.

The different interactions of γ-rays with matter shall be discussed with respect to their usefulness as polarization analyzers keeping in mind the possibilities (a) and (b).

2.1. PHOTOELECTRIC EFFECT

A free electron cannot absorb a photon and become a photoelectron. In order to conserve momentum a third body, the nucleus, is necessary. Therefore the electrons are ejected mainly from inner shells. As these shells are filled the electrons cannot be polarized and method (a) cannot be applied.

On the other hand the photoelectrons are longitudinally polarized if they are ejected by circularly polarized γ-rays (case (b)). The calculated electron polarization as function of the quantum energy is shown in fig. 1. For high quantum energies large electron polarizations may be obtained. For the detection of the electron polarization Mott- or Møller-scattering could be used[8]). However, the expected counting rates will be small, as both, the converter and the electron scattering foil must be thin. For small quantum energies ($h\nu \lesssim 250$ keV) and using Mott-scattering this disadvantage is compensated partly by the fact that the asymmetry is larger than for the methods to be described later.

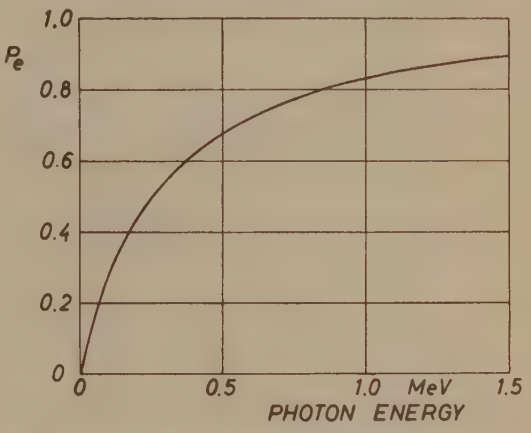

Fig. 1. The average longitudinal polarization of photoelectrons P_e produced by completely circularly polarized photons as a function of photon energy (McVoy[15]).

It may be mentioned that the reverse of the process considered here is the emission of a single circularly polarized quantum following the annihilation of a longitudinally polarized positron[15]).

2.2. COMPTON SCATTERING

Compton scattering from polarized electrons (case (a)) available in magnetized iron is the

[12]) H. Schopper and S. Galster, Nuclear Physics **6** (1958) 125.

[13]) M. Deutsch, B. Gittelmann, R. W. Bauer, L. Grodzins and A. W. Sunyar, Phys. Rev. **107** (1957) 1733;
F. Boehm, T. B. Novey, C. A. Barnes and B. Stech, Phys. Rev. **108** (1957) 1497.

[14]) H. A. Tolhoek, Revs. Mod. Phys. **28** (1956) 277.

[15]) K. W. McVoy, Phys. Rev. in press.

only method used successfully so far to measure the circular polarization of γ-rays. This method will be discussed in some detail in section 3.

Case (b) could also be used as longitudinally polarized electrons are produced by scattering circularly polarized photons from unoriented electrons. The calculation of Lipps and Tolhoek[16]) show (fig. 2) that a large electron polarization

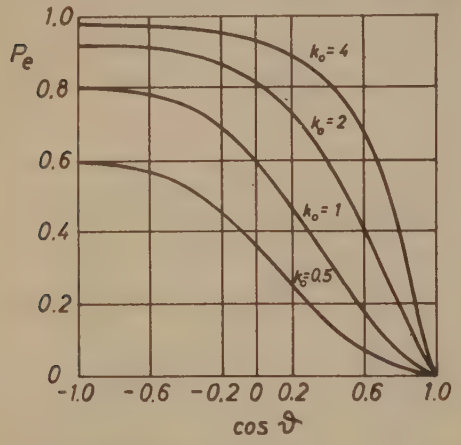

Fig. 2. The longitudinal polarization P_e of recoil electrons produced by Compton scattering of completely circularly polarized photons (Lipps and Tolhoek[16])). ϑ scattering angle, photon energy $k_0 = h\nu/m_0c^2$.

can be obtained for backscattering and high quantum energies. But the detection efficiency will be small again, as an appreciable loss of counts ensues from the measurement of the electron polarization.

2.3. PAIR PRODUCTION

If a circularly polarized high energy quantum produces an electron pair the helicity of the photon is transferred in part to the electrons. This electron polarization could be used to detect the circular polarization of the photons. However, no detailed calculations have yet been performed. The reverse of this process is the production of circularly polarized bremsstrahlung by polarized electrons[17]). It is interesting to note that if these processes happen one after the other one gets an electromagnetic cascade in which, in the relativistic limit, the longitudinal polarization is conserved to a high degree[18]).

2.4. PHOTONUCLEAR EFFECT

Principally the circular polarization of γ-rays could be detected by the photodisintegration of polarized nuclei. But it seems to be very difficult to polarize a sufficient number of nuclei in order to use them as target.

It might be more feasible to use method (b) that is to investigate the polarization of photoprotons or neutrons emitted from unpolarized nuclei. For low quantum energies D^2 and Be^9 would be favourable target nuclei. However, in the case of D^2 the protons will have only small polarization for low photon energies[19]). The polarization of photoneutrons emitted from Be^9 may be somewhat larger. Detailed calculations have not yet been performed. The polarization of the protons or neutrons could be measured by scattering at He^4 [20]). The overall efficiency will be small, but for higher photon energies ($\gtrsim$ 20 MeV) these methods could be useful as for such energies the Compton cross section is very small.

In conclusion it can be said that for intermediate photon energies (from about 0.2 to some MeV) the Compton scattering from polarized electrons is the most favourable method. For higher photon energies pair production and photonuclear effect might turn out to be useful. No satisfactory method is known so far for low photon energies (< 0.1 MeV) excluding of course the limit of classical optics in which case quarter wave plates can be used taking advantage of the double refraction of crystals.

3. Compton Scattering from Polarized Electrons as Analyzer for Circularly Polarized γ-Rays

The state of polarization of γ-radiation can be analyzed by Compton scattering with polarized electrons as this scattering cross section and, hence, the intensity of the scattered radiation depends on the relative direction of

[16]) F. W. Lipps and H. A. Tolhoek, Physica **20** (1954) 395.

[17]) K. W. McVoy, Phys. Rev. **106** (1957) 828.

[18]) K. W. McVoy and F. J. Dyson, Phys. Rev. **106** (1957) 1360.

[19]) P. Stichel, private communication.

[20]) P. E. S. Hodgson, Advances in Physics **7** (1958) 1.

photon and electron spin. Reversing the spins of the scattering electrons results in a change in scattered intensity if the γ-radiation is circularly polarized. As this method turned out to be the most useful one so far, we shall discuss the various experimental arrangements possible in some detail.

The differential scattering cross section was derived by several authors[21]) and can be written in the following form

$$d\sigma = \frac{r_0^2}{2}\left(\frac{k}{k_0}\right)^2 \{\phi_0 + P_1\phi_1 + f P_c \phi_c\} \qquad (1)$$

where r_0 is the classical electron radius.

$\boldsymbol{k}_0$ is the initial photon momentum,

$\boldsymbol{k}$ is the photon momentum after scattering,

P_1 is the degree of linear polarization and is positive if the electric vector $\boldsymbol{E}$ is perpendicular to the $(\boldsymbol{k}_0\,\boldsymbol{k})$-plane, negative if $\boldsymbol{E}$ lies in the plane of scattering†,

P_c is the degree of circular polarization of the photons and is positive if the radiation is right circularly polarized (r.c.p.) ††,

f is the fraction of oriented electrons.

ϕ_0 gives the ordinary Compton cross section (first derived by Klein-Nishina), whereas ϕ_1 and ϕ_c are the polarization dependent parts of the cross section:

$$\begin{aligned}\phi_0 &= 1 + \cos^2\vartheta + (k_0 - k)(1 - \cos\vartheta)\\ \phi_1 &= \sin^2\vartheta \qquad (2)\\ \phi_c &= -(1-\cos\vartheta)\\ &\quad [(k_0 + k)\cos\vartheta\cos\psi + k\sin\vartheta\sin\psi\cos\varphi],\end{aligned}$$

ϑ is the scattering angle, ψ is the angle between the direction of the incident photon $\boldsymbol{k}_0$ and the electron spin $\boldsymbol{S}$ and φ is the angle between the $(\boldsymbol{k}\,\boldsymbol{S})$-plane and the $(\boldsymbol{k}_0\,\boldsymbol{k})$-plane (fig. 3). From the expression for ϕ_c it can be seen that there are two possibilities of measuring the circular polarization. The most obvious way is to reverse the spin direction changing ψ into $\psi + \pi$ thus reversing the sign of ϕ_c. Alternatively one can change the counter position from φ to $\varphi + \pi$ keeping the spin direction fixed†††. The various experimental arrangements resulting from these possibilities shall be discussed now in some detail.

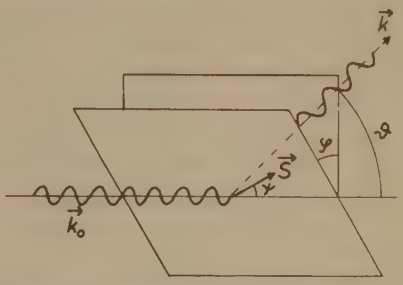

Fig. 3. Compton scattering from polarized electrons. $\boldsymbol{k}_0$, $\boldsymbol{k}$ momentum of incident and scattered photon, respectively, $\boldsymbol{S}$ electron spin.

Denoting N_+ as the number of scattered photons if the electron spin is roughly parallel to the incident γ-quantum $(0 \leqslant \psi < \pi/2)$ and N_- as the corresponding number with the spin approximately antiparallel $(\pi \leqslant \psi < 3\pi/2)$ the relative difference in counting rate on *reversing the electron spin* is

$$E = \frac{N_- - N_+}{(N_- + N_+)/2} = \frac{2 f P_c \phi_c^-/\phi_0}{1 + P_1\phi_1/\phi_0} \qquad (3)$$

where

$$\phi_c^- \equiv \phi_c\ (\pi \leq \psi < 3\pi/2)\ .$$

In order to find the most favourable experimental set-up which gives the highest possible difference E for given values of P_c and f one has to investigate the dependence of ϕ_c/ϕ_0 on ϑ and ψ.

Gunst and Page[22]) computed ϕ_c/ϕ_0 as a function of ϑ for the special case $\psi = 0°$ (fig. 4). From these curves it may be gathered that there are two ways to measure the circular polarization using differential scattering. ϕ_c/ϕ_0 has one maximum for forward scattering ($\vartheta \approx 60°$ for energies near 1 MeV) and another one for backscattering ($\vartheta = 180°$).

†) P_1 is defined by $P_1 = |P_1|\,(\sin^2\chi - \cos^2\chi)$, where χ is the angle between the electric vector and the plane of scattering.

††) Here we shall use the quantum mechanical definition according to which a photon is called r.c.p. if it has an angular momentum $+\hbar$ in the direction of propagation. The electric vector rotates clockwise for an observer looking in this direction. This definition is in contrast to the usual optical convention.

†††) Of course, an equivalent description would be to keep φ fixed and to go from ψ to $-\psi$.

[21]) W. Franz, Ann. Phys. **33** (1938) 689;
V. Fano, Journ. Opt. Soc. Am. **39** (1949) 859;
F. W. Lipps and H. A. Tolhoek, Physica **20** (1954) 85 and 395.

[22]) S. B. Gunst and L. A. Page, Phys. Rev. **92** (1953) 970.

However, $\psi = 0°$ is not the most favourable case. Taking the derivative of ϕ_c with respect to ψ and putting it equal to zero one finds that ϕ_c/ϕ_0 will have a maximum at

$$\operatorname{tg} \psi_m = [2 + k_0 (1 - \cos \vartheta)]^{-1} \cdot \operatorname{tg} \vartheta \ . \qquad (4)$$

ψ_m as a function of ϑ is plotted in the upper part of fig. 5 for different values of k_0.

The optimal scattering angle ϑ_m cannot be calculated as easily. Differentiating ϕ_c/ϕ_0 with respect to ϑ gives a very complicated equation

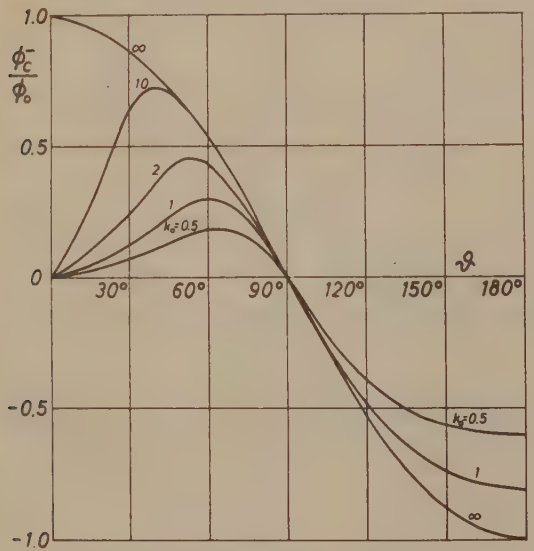

Fig. 4. The ratio of the polarization dependent part ϕ_c of the differential Compton-cross section to the normal Compton cross-section ϕ_0 as a function of the scattering angle ϑ for the case $\psi = 0$. Photon energy in units of $m_0 c^2$ (Gunst and Page[22]).

which cannot be solved analytically. Therefore ϕ_c/ϕ_0 was evaluated as a function of ϑ using for each ϑ the respective ψ_m taken from the upper part of fig. 5. The result is shown in the lower part of fig. 5. Comparison with fig. 4 shows that for low photon energies and forward scattering ϕ_c/ϕ_0 is appreciably higher. For example the increase amounts to about 25% for $k_0 = 1$. On the other hand nothing can be gained for backscattering ($\psi_m = 0$ or 180°).

3.1. FORWARD SCATTERING

In this case the most favourable scattering angle ϑ_m giving maximum ϕ_c/ϕ_0 depends on the incident photon energy as can be seen from figs. 4 and 5. For convenience ϑ_m is plotted as a function of photon energy in fig. 6a for $\psi = 0°$

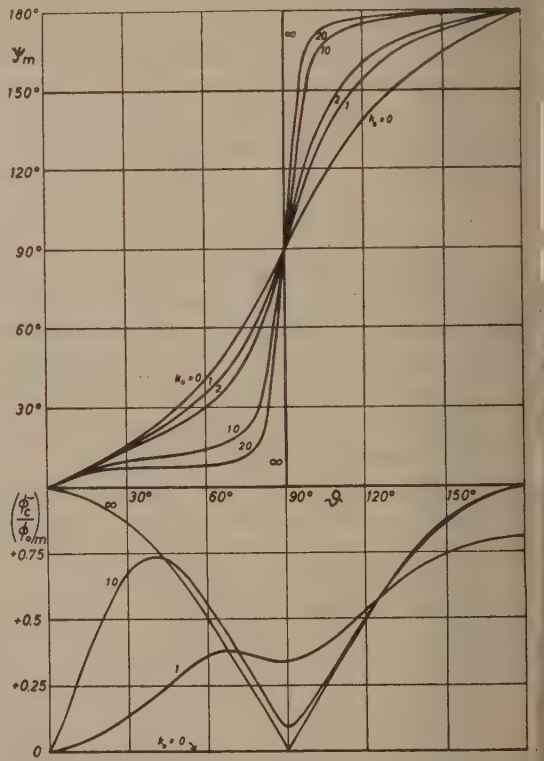

Fig. 5. Upper part: the angle ψ_m between photon momentum and electron spin giving the maximum value $(\phi_c/\phi_0)_m$. Lower part: Maximum value $(\phi_c/\phi_0)1$ as a function of scattering angle. k_0 photon energy in units of $m_0 c^2$.

and for $\psi = \psi_m$. The maximum values of ϕ_c/ϕ_0 belonging to these scattering angles are presented in fig. 6b.

From these figures it can be seen that this method will be suitable for photon energies above 0.2 MeV. For smaller energies ϕ_c/ϕ_0 decreases rapidly. For high energies ϑ_m becomes small. As a consequence only small solid angles can be used and hence the scattered intensity is low. This is compensated partly by the fact that forward scattering is enhanced if the photon energy is high. But above 3 MeV other methods might be more suitable (see below).

Polarized electrons are available, so far, only

in magnetized iron. Even at saturation only about 8% of the electrons can be polarized.

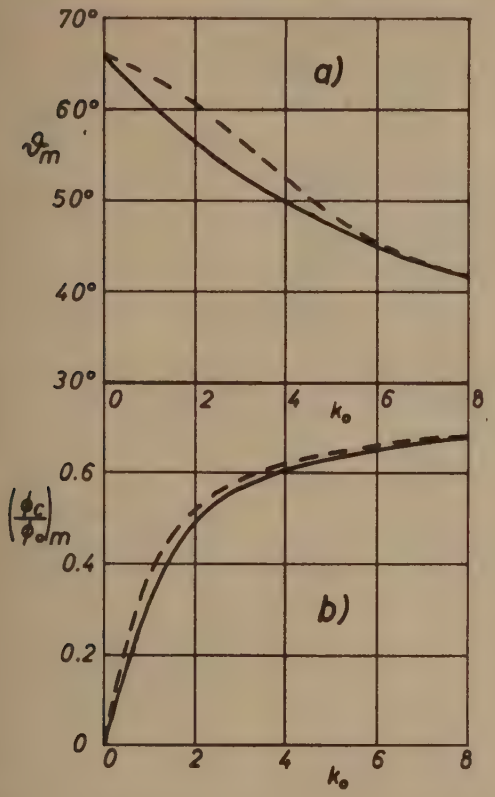

Fig. 6. (a) The scattering angle ϑ_m giving maximum value of ϕ_c/ϕ_0 in case of forward scattering. (b) Maximum value of ϕ_c/ϕ_0 if $\vartheta = \vartheta_m$. Full lines: $\psi = 0^0$, broken lines $\psi = \psi_m$. k_0 photon energy in units of $m_0 c^2$.

Thus even for completely circularly polarized γ-rays ($P_c = \pm 1$) a relative difference in counting rate $E \approx 8\%$ under reversal of magnetization can be obtained. However, changes of about 1% can still be measured sufficiently accurately without too much effort.

The most favourable geometry is one with rotational symmetry. In many cases a cylindrical scattering magnet as shown in fig. 7 is suitable. If the γ-intensity is very low a magnet with semicircular cross section (fig. 8) may be of advantage as in this case the solid angle is large but the scattering angles, nevertheless, are close to ϑ_m. The direct radiation must be shielded against by a lead absorber which imposes a minimum to the dimensions of the magnet. The magnet must be thick enough in order to make the scattering from the magnetizing coil negligible.

Care must be taken that the magnetic stray field does not influence the counter as otherwise an effect could be feigned. It turned out to be advisable to use a light guide (about 0.5 m long) in order to keep the multiplier away from the magnet. If additional magnetic shields or a compensation coil (figs. 7 and 8) are used the relative change in counting rate produced by the strayfield can be kept smaller than 0.1% under reversal of the magnetization. With such arrangements it is possible to count 1 photon out of 10^3 to 10^4 photons emitted by the source. This comparatively high efficiency is one of the main advantages of this method as high counting rates are essential in view of the extreme statistical accuracies which must be obtained.

In order to calculate the effective ϕ_c/ϕ_0 one has to average over the geometry of the set-up. It is another advantage of the forward scattering method that this computation can be carried out to an accuracy of a few percent as will be shown in section 4.

On the other hand the finite sizes of source, magnet and counting crystal have as a consequence that a γ-line is broadened considerably after scattering. Therefore forward scattering is disadvantageous as far as energy discrimination is concerned.

The determination of the sign of the circular polarization is somewhat tedious. Therefore it may be stressed that r.c.p. photons (photon spin parallel to momentum) lead with the definition (3) to a positive change in counting rate ($E > 0$) as ϕ_c^-/ϕ_0 is positive for $\vartheta < 90°$. That means that more photons are scattered in forward direction if the magnetization is pointing away from the source†.

†) Note that the electron spin is antiparallel to the magnetization as the magnetic moment of the electron is negative.

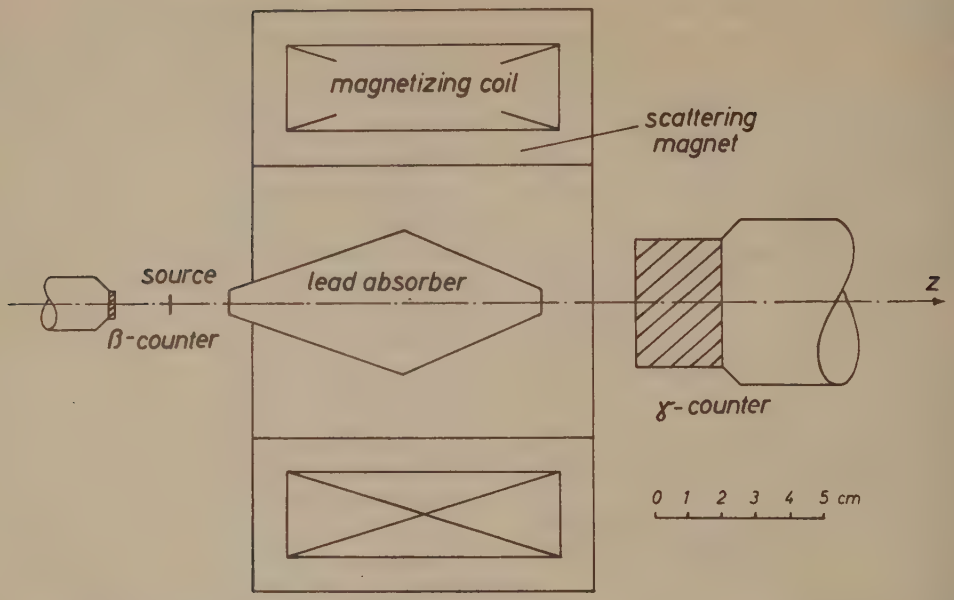

Fig. 7. Experimental arrangement for the measurement of the β–γ circular polarization correlation using forward scattering (Schopper[4])).

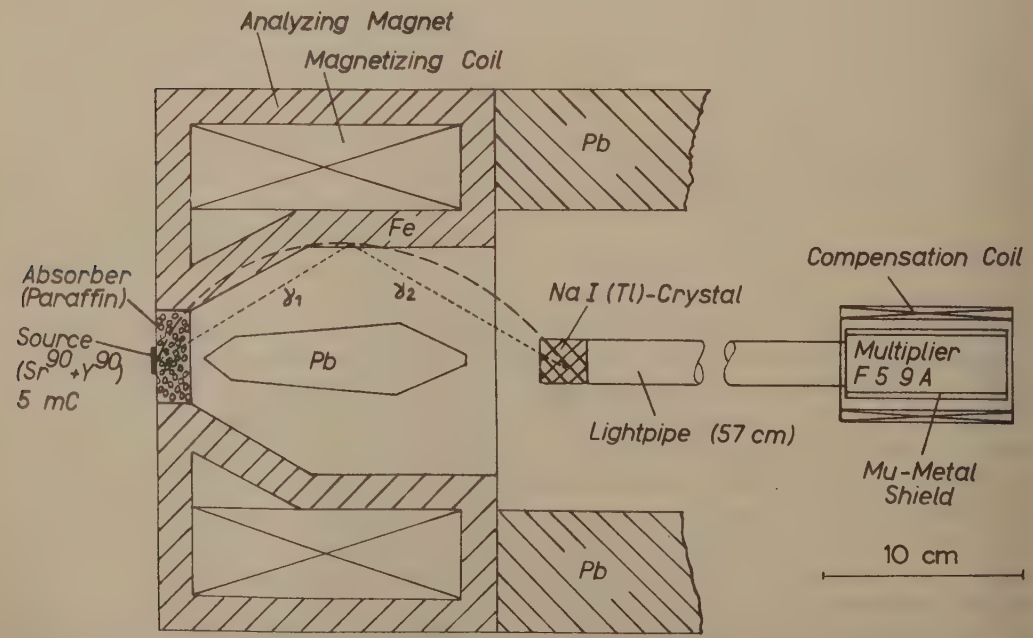

Fig. 8. Scattering magnet used for the measurement of the circular polarization of bremsstrahlung[12]).

3.2. BACKSCATTERING

ϕ_c/ϕ_0 reaches higher values for backscattering than for forward scattering (fig. 9) and approaches even unity for high energy photons.

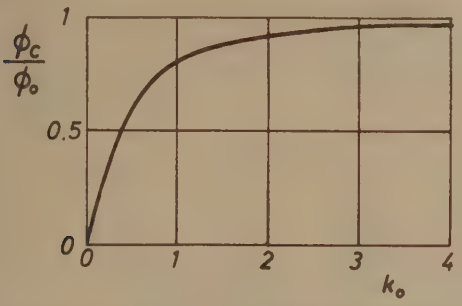

Fig. 9. ϕ_c/ϕ_0 as a function of photon energy k_0 (in units of $m_0 c^2$)) for backscattering ($\vartheta = 180^0$).

Consequently as far as the magnitude of ϕ_c/ϕ_0 is concerned backscattering is the most favourable method. The back scattered intensity, however, will be relatively low, as the differential Compton cross section is particularly small for high photon energies. In addition back scattered photons have similar energies independent of their initial energies. Hence energy discrimination by pulse height selection is practically not possible. Moreover the photons scattered by the floor, walls or parts of the equipment will have similar energies and therefore this background cannot be suppressed by energy selection.

Owing to these disadvantages this method has not yet been tried experimentally.

All the difficulties mentioned could be avoided by detecting the knock-on electrons instead of the back scattered quanta. But as the electrons must not be scattered or slowed down thin iron foils have to be used as scatterers. This implies that the number of knock-on electrons is very small. Therefore this variant of the backscattering method is inferior to other arrangements. It has been used once[23]) but it is thought now that the effect was of instrumental origin[14]).

3.3. TRANSMISSION

The transmission of a beam of circularly polarized photons through iron depends on the magnetization. The largest effect can be achieved if the direction of the incident photon is parallel ($\psi = 0$ or $180°$) or antiparallel to the magnetization.

By integrating the differential Compton-cross section (eq. (1)) one obtains a total scattering cross section which is of the form

$$\sigma = \sigma_0 + f P_e \sigma_e \tag{5}$$

where σ_0 is the well known polarization insensitive and

$$\sigma_e^{\pm} = \pm 2\pi r_0^2 \left\{ \frac{1 + 4k_0 + 5k_0^2}{k_0 (1 + 2k_0)^2} - \right.$$
$$\left. - \frac{1 + k_0}{2 k_0^2} \ln (1 + 2k_0) \right\} \tag{6}$$

the polarization sensitive part. The upper (lower) sign corresponds to photon spin parallel (antiparallel) to the electron spin and hence antiparallel (parallel) to the magnetization. The relative difference in counting rate is given by†

$$E' = \frac{N'_+ - N'_-}{(N'_+ + N'_-)/2} = 2 \tanh (NL \nu \sigma_e^- P_e) \tag{7}$$

N'_+ (N'_-) is the number of transmitted photons if the electron spin is parallel (antiparallel) to the direction of incident photons, N is the number of iron atoms/cm^3, L is the length of the iron absorber and $Zf = \nu$ is the number of oriented electrons per iron atom ($\nu = 2.06$ at saturation)[24]).

σ_e^- is represented as a function of the photon energy in fig. 10. The change in sign occurring for $1.25\ m_0c^2 = 0.65$ MeV can be understood from the difference in sign for ϕ_c for forward and back scattering (see figs. 4 and 5) and from the fact that forward scattering becomes more and more predominant for increasing photon energy. Hence the sign of σ_e^- is the same as of ϕ_c^- ($\vartheta < \pi/2$) for large values of k_0. That means that the transmission is greatest when the photon

[23]) F. P. Clay and F. L. Hereford, Phys. Rev. **85** (1952) 675.

[24]) P. Argyres and C. Kittel, Acta Metallurgica **1** (1953) 241.

†) Note that E' is defined with the reverse sign compared to E (eq. (3)). This seems to be sensible as the *absorption* is measured instead of the *scattering*. Hence E' and E will have the same sign for a given sign of P_c.

spin is parallel to the electron spin. From fig. 10 it can be inferred that the transmission method will not be applicable to photon energies around 600 keV.

$L = L_0$ leads to an effect $E'_m = 4 P_c \tau_c / \tau_t$. The quantity $4 \tau_c / \tau_t$ is plotted in fig. 10.

For a photon energy of 1 MeV L_0 is approximately 4.5 cm and $E'_m \approx 2\%$ for $P_c = 1$. Com-

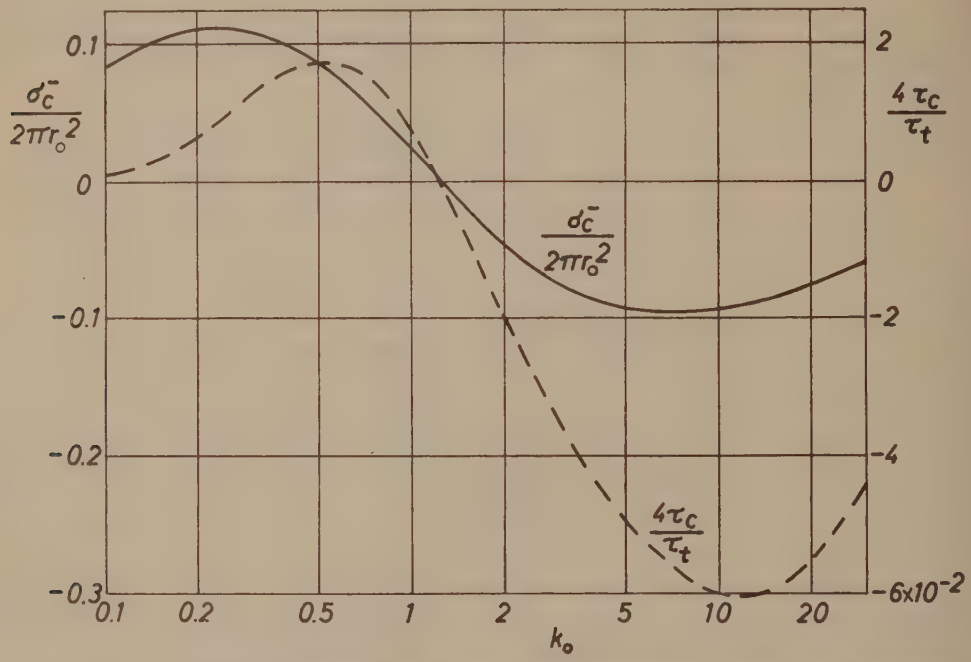

Fig. 10. Full line: The polarization dependent total Compton crosssection σ_c^- as function of the photon energy k_0 (in units of $m_0 c^2$). $2\pi r_0^2 = 0.50$ barn. Broken line: relative change in counting rate $E' = 4 \tau_c / \tau_t$ if $L = L_0$ and $| P_c | = 1$.

It might seem an advantage of the transmission method that one can get very large effects by using long iron absorbers. But as at the same time the counting rate is reduced considerably, long counting times are necessary to obtain a satisfying statistical accuracy. The best information in a fixed time can be achieved if $\Delta E'/E'$ is minimized where $\Delta E'$ is the statistical error of E'. $\Delta E'/E'$ is proportional to $\exp(NL\tau_t/2)/2NLP_c\tau_c$ where τ_t is the total absorption coefficient (including photoelectric effect and pair production) and $\tau_c = \nu \sigma_c$ the polarization dependent part of the cross section per atom. The assumption $NL\tau_c P_c \ll 1$ has been made which is valid for all practical cases. Differentiation with respect to L gives for the optimal length L_0 the condition $NL_0\tau_t = 2$. Optimizing the experimental set-up by choosing pared with the scattering method ($E \approx 8\%$) the effect is reduced considerably. As the counting rate will be smaller too, the transmission method is definitely inferior to the scattering method as far as a quick gathering of information is concerned. Hence the scattering method will be more useful e.g. in coincidence work, in which case the source strength is limited by the number of random coincidences. With respect to energy discrimination, however, the transmission method is superior, as by scattering the γ-lines are considerably broadened.

Fig. 11 shows the arrangement used by Goldhaber *et al.*[11]) to detect the circular polarization of external bremsstrahlung. Lundby *et al.*[25]) used a somewhat improved magnet, the yoke of

[25]) A. Lundby, A. P. Patro and J. P. Stroot, Nuovo Cimento 6 (1957) 745; and preprints.

which had a large diameter enabling them to keep the magnetizing coil away from the absorber. Thus small angle scattering from the copper coil was avoided.

A difficulty arises in determining the effective length of the iron absorber as the magnetization at its ends is not complete. No satisfactory solution of this problem has yet been found.

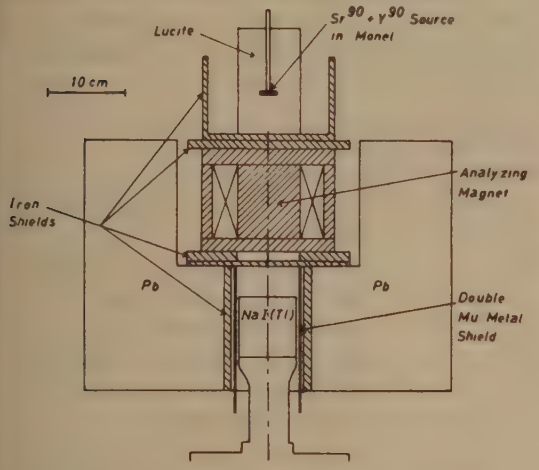

Fig. 11. Experimental arrangement for the measurement of circular polarization of external bremsstrahlung using the absorption method. (Goldhaber *et al.*[11]).)

3.4. MEASUREMENT OF THE AZIMUTHAL ANISOTROPY

In all the methods described so far, the asymmetry was measured by reversing the direction of the electron spin. Such a reversal resulted in a change of sign of ϕ_c. An alternative method is to change the azimuthal position of the counter from φ to $\varphi+\pi$ or equivalenty to change the spin direction from ψ to $-\psi$ (fig. 3). In this case ϕ_c must be split up in two parts $\phi_c = \phi_{c1} + \phi_{c2}$ where

$$\phi_{c1} = -(1-\cos\vartheta)(k_0+k)\cos\vartheta\cos\psi$$

and

$$\phi_{c2} = -(1\cos\vartheta)\, k\sin\vartheta\sin\psi\cos\varphi\,. \qquad (8)$$

Moving the counter from position $\varphi = 0$ to $\varphi = \pi$ changes the sign of ϕ_{c2} whereas ϕ_{c1} is left unaltered. Then an azimuthal anisotropy

$$\Delta = \frac{n_- - n_+}{(n_- + n_+)/2} = \frac{2\, f\, P_c\, \phi_{c2}}{\phi_0 + P_1\,\phi_1 + f P_c\,\phi_{c1}} \qquad (9)$$

can be observed, where n_+ (resp. n_-) is the counting rate for the position $\varphi = 0$ (resp. $\varphi = \pi$) or equivalently $\psi > 0$ (resp. $\psi < 0$).

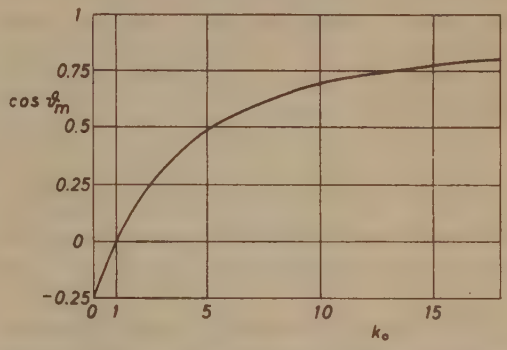

Fig. 12. The scattering angle ϑ_m giving maximum azimuthal anisotropy Δ_m (see (9)) as a function of photon energy k_0 (in units of m_0c^2). (Beard and Rose[26]).)

Obviously the largest effect can be obtained, if ϕ_{c2} is maximum and ϕ_{c1} minimum. This is the case for $\psi = \pm 90°$ ($\phi_{c1} = 0$). This method was proposed by Beard and Rose[26]). They computed the scattering angle ϑ_m for which ϕ_{c2}/ϕ_0 is maximized, thus giving a maximum azimuthal

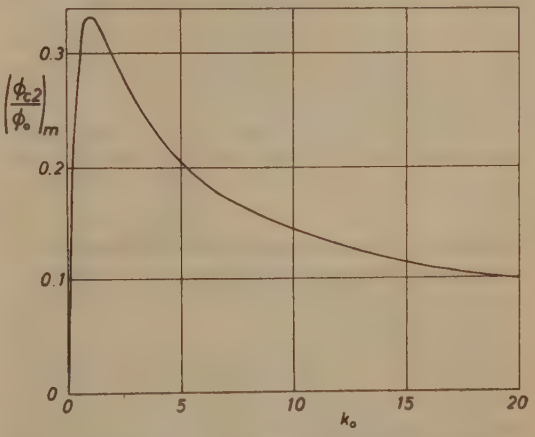

Fig. 13. Maximum value of ϕ_{c2}/ϕ_0 as a function of photon energy (in units of m_0c^2). (Beard and Rose[26]).)

anisotropy Δ_m. ϑ_m as a function of the photon energy is presented in fig. 12. The resulting $(\phi_{c2}/\phi_0)_m$ is shown in fig. 13 as a function of k_0.

[26]) D. B. Beard and M. E. Rose, DRNL-Report No. 1072 (1951); and Phys. Rev. **108** (1957) 164.

One observes that it attains a maximum value of 0.33 at $k_0 = 1$ giving a maximum observable anisotropy $\Delta_m = 5.6\%$. For $k_0 = 1$ the magnitude of this anisotropy is comparable with the asymmetries obtainable with other methods whereas for $k_0 > 2$ it is appreciably smaller. Consequently this method might be useful only for small photon energies.

The main advantage of the method, however, is that the azimuthal anisotropy may be determined from two simultaneous measurements at opposite azimuthal scattering angles. In this way some systematic errors (e.g. temperature changes) can be eliminated, and the counting time will be reduced by a factor of two.

On the other hand as far as intensity is concerned this method is inferior to others (e.g. forward scattering) though the solid angles which can be used are approximately the same. But as ϑ_m is close to 90° for $k_0 \approx 1$ the differential scattering cross section is smaller by a factor of about two compared to forward scattering. Moreover, as $\vartheta_m \approx 90°$ and the magnetization should be perpendicular to the direction of the incident photon ($\psi \approx 90°$) the scattered photon will have to cover a comparatively long path inside the iron. This results in a considerable loss of intensity by absorption owing to the low photon energy after scattering.

These disadvantages may be the reason that this method has not been used up to the present time.

4. Determination of the Circular Polarization from the Observed Asymmetry

4.1. GENERAL CALCULATION

In the discussion of the various methods suitable for the detection of the circular polarization of γ-rays an ideal geometry was assumed and secondary effects were not taken into account. If, however, in an actual experiment the degree of circular polarization is to be determined with some accuracy these effects must be considered.

The forward scattering method shall be investigated in some detail in this section. In this case the following points must be taken care of: finite geometry, absorption of photons in the iron before and after scattering, polarization dependence of this absorption and plural scattering in the iron.

Similar calculations have not yet been performed for the transmission method. In that case the exact determination of the effective absorber length would be the main difficulty.

The number of photons scattered by a volume element dV_{Fe} of the scattering magnet and giving rise to a count in the scintillation crystal is given by

$$dN = \frac{n_\gamma}{4\pi} \cdot \frac{\varepsilon}{r_1^2 r_2^2} d\sigma \cdot n_0 \cdot e^{-(\sigma_1 s_1 + \sigma_2 s_2) n_0} \, dV_{Fe} \, dF_{cr} \quad (10)$$

where

n_γ	number of γ-rays/sec emitted by the source,
$d\sigma$	polarization dependent Compton cross section per electron,
n_0	number of electrons/cm³,
dF_{cr}	differential detecting area of scintillation crystal as seen from the scattering point,
ε	detection probability for a photon falling upon dF_{cr} (ε is a function of photon energy, crystal shape, ϑ and θ),
σ_1, σ_2	total absorption cross sections per electron† for incident and scattered photon, respectively. σ_1, σ_2 are polarization dependent,
r_1, r_2, s_1 and s_2	are defined in fig. 14,
$g = s_2/s_1$	(If the cross section of the scattering magnet is curved g is a function of r_1. Otherwise $g = \sin\psi/\sin(\vartheta - \psi)$ is independent of r_1.)

In all practical cases the source will be small compared with the dimensions of the magnet. Hence its finite size was neglected.

In order to get the total count rate dN must be integrated over the magnet volume and the crystal section. A rigorous calculation of these

† The absorption owing to the photoelectric effect and pair production can easily be taken into account by putting

$$\sigma = \sigma_{compton} + (\tau_{ph} + \tau_{pair})/Z$$

where τ_{ph} and τ_{pair} are absorption coefficients per atom.

integrals would be very complicated. To facilitate this task some simplifications must be introduced.

An overwhelming part of the photons is scattered from an iron layer near to the surface of the magnet as the penetration depth is only of the order of 1 cm (for 1 MeV-quanta). Hence for constant θ the variation of r_1 is small compared to r_2 ($\approx$ 10 cm in practical cases) and the position of the scattering point is nearly unchanged with respect to the crystal. In addition the size of the crystal as compared to the magnet is limited because only scattering angles close to the optimal one are useful (figs. 4 and 5). Therefore k and r_2 are practically the same for different $\mathrm{d}F_{\mathrm{cr}}$. From this follows that a good approximation will be obtained by introducing effective values $\bar{F}$ and $\bar{\varepsilon}$ instead of integrating over the crystal. However, $\bar{F}$ and $\bar{\varepsilon}$ will still be functions of θ.

Then the total counting rate will be obtained by

$$N = \frac{n_\gamma n_0}{4\pi} \int_{V_{\mathrm{Fe}}} \frac{F\varepsilon}{r_2^2} \, \mathrm{d}\sigma \, \mathrm{e}^{-(\sigma_1 s_1 + \sigma_2 s_2) n_0} \sin\theta \, \mathrm{d}\theta \, \mathrm{d}\varphi \mathrm{d}r_1 \quad (11)$$

where polar coordinates were introduced.

From the arguments given above it can be inferred that $\mathrm{d}\sigma$, $\bar{F}$ and $\bar{\varepsilon}$ vary only slightly with r_1 if θ is held fixed. Consequently the integral over r_1 in eq. (11) can be approximated by

$$\int \frac{\overline{F\varepsilon}}{r_2^2} \mathrm{d}\sigma \, \mathrm{e}^{-(\sigma_1 s_1 + \sigma_2 s_2) n_0} \, \mathrm{d}r_1 =$$

$$= \left\langle \frac{\overline{F\varepsilon}}{r_2^2} \mathrm{d}\sigma \right\rangle \int \mathrm{e}^{-(\sigma_1 s_1 + \sigma_2 s_2) n_0} \, \mathrm{d}r_1 \, . \quad (12)$$

This equation can be considered as a definition of the average $< \overline{F\varepsilon}/r_2^2 \cdot \mathrm{d}\sigma >$. If one calculates $< 1/r_2^2 \cdot \mathrm{d}\sigma >$ using (12) for a few typical cases, it turns out that it equals the actual value of $1/r_2^2 \cdot \mathrm{d}\sigma$ at approximately $s_1 = 6$ mm (resp. 8 mm) for $k_0 = 0.5$ MeV (resp. 1 MeV). The difference between this value and the one at $s_1 = 0$ ammounts to a few percent only. Thus for practical cases a sufficient accuracy can be obtained by calculating $1/r_2^2 \cdot \mathrm{d}\sigma$ for the quoted penetration depths and taking these values as the averages.

The integral on the right side of (12) can easily be evaluated and if the scattering magnet has rotational symmetry with respect to the z-axis one finds

$$N = \frac{n_\gamma}{2} \int \left\langle \frac{\overline{F\varepsilon}}{r_2^2} \cdot \mathrm{d}\sigma \right\rangle \frac{1 - \mathrm{e}^{-(\sigma_1 + g\sigma_2) n_0 d}}{\sigma_1 + g\sigma_2} \sin\theta \, \mathrm{d}\theta \, . \quad (13)$$

d is the magnet thickness measured along r_1 (fig. 14). For some magnet geometries cylindrical

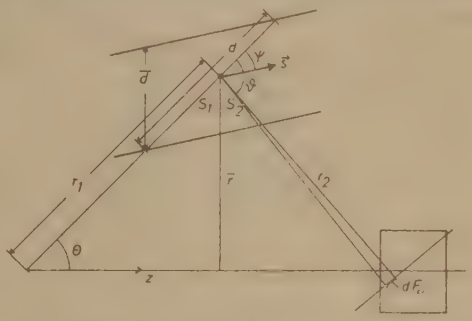

Fig. 14. Pictorial representation of the scattering of a photon inside the magnet.

coordinates $(\bar{r}, \varphi, z)$ are more useful. In this case one gets

$$N = \frac{n_\gamma}{2} \int \left\langle \frac{F\varepsilon}{r_1^2 r_2^2} \bar{r} \, \mathrm{d}\sigma \right\rangle$$

$$\frac{1 - \mathrm{e}^{-(\sigma_1 + g\sigma_2) n_0 \bar{d} \frac{\cos(\psi - \theta)}{\sin\psi}}}{\sigma_1 + g\sigma_2} \cdot \frac{\sin\psi \, \mathrm{d}z}{\cos(\psi - \theta)} \quad (14)$$

instead of (13). Of course, the averaging has to be done here over $\bar{r}$. $\bar{d}$ is the thickness of the magnet measured perpendicular to the z-direction (see fig. 14).

In most experiments the magnet will be chosen thick enough to prevent γ-quanta being scattered to an appreciable ammount from other materials lying behind the iron e.g. the magnetizing coil. As a consequence the exponential functions in (13) and (14) can be neglected.

In order to demonstrate the polarization dependence on N explicitly the cross sections must be split up into polarization dependent and independent parts according to (1) and (5)

$$\mathrm{d}\sigma = \mathrm{d}\sigma_0 + fP_{\mathrm{c}} \, \mathrm{d}\sigma_{\mathrm{c}} \quad (15)$$

and

$$\begin{aligned} \sigma_1 &= \sigma_{t2} + fP_{\mathrm{c}} \, \sigma_{\mathrm{c}1} \\ \sigma_2 &= \sigma_{t2} + fP_{\mathrm{c}} \times \sigma_{\mathrm{c}2} \end{aligned} \quad (16)$$

where σ_t is the sum of the polarization independent Compton-cross section σ_0 and the absorption

cross sections per electron for photoelectric effect and pair production. $\varkappa$ is the ratio between the polarization after and before scattering. As f is very small even at saturation (0.08), the denominator of (13) can be expanded in a power series and higher powers of f may be omitted. Using the expression of N_+ and N_- found in this way in eq. (3) one obtains for the asymmetry the relation†

$$E = 2\, f P_e \langle \mathrm{d}\sigma_c/\mathrm{d}\sigma_0 \rangle \tag{17}$$

where $\langle\ \rangle$ is an abbreviation for

$$\langle \mathrm{d}\sigma_c/\mathrm{d}\sigma_0 \rangle = \frac{\int \left\langle \frac{\overline{F\varepsilon}}{r_2^2}\, \mathrm{d}\sigma_c^- \right\rangle \frac{\sin\theta\, \mathrm{d}\theta}{\sigma_{t1} + g\sigma_{t2}}\, w_p}{\int \left\langle \frac{\overline{F\varepsilon}}{r_2^2}\, \mathrm{d}\sigma_0 \right\rangle \frac{\sin\theta\, \mathrm{d}\theta}{\sigma_{t1} + g\sigma_{t2}}} \tag{18}$$

in polar coordinates and

$$\langle \mathrm{d}\sigma_c/\mathrm{d}\sigma_0 \rangle = \frac{\int \left\langle \frac{\overline{F\varepsilon}}{r_1^2 r_2^2}\, \bar{r}\, \mathrm{d}\sigma_c^- \right\rangle \frac{\sin\psi\, \mathrm{d}z}{\cos(\theta - \psi)\,(\sigma_{t1} + g\sigma_{t2})}\, w_p}{\int \left\langle \frac{\overline{F\varepsilon}}{r_1^2 r_2^2}\, \bar{r}\, \mathrm{d}\sigma_0 \right\rangle \frac{\sin\psi\, \mathrm{d}z}{\cos(\theta - \psi)\,(\sigma_{t1} + g\sigma_{t2})}} \tag{19}$$

in cylindrical coordinates†† with

$$w_p = 1 - \frac{\langle \mathrm{d}\sigma_0 \rangle}{\langle \mathrm{d}\sigma_c^- \rangle} \cdot \frac{\sigma_{c1}^- + g\varkappa\sigma_{c2}^-}{\sigma_{t1} + g\sigma_{t2}}\,. \tag{20}$$

It may be quite instructive to discuss the meaning of the different factors in (18) and (19). Evidently the integrals are averages of $\mathrm{d}\sigma_c$ and $\mathrm{d}\sigma_0$, respectively. Most of the weights are simply of geometrical origin (e.g. r_1, r_2, $\sin\theta$). $F\varepsilon$ takes care of the fact that the counting efficiency varies with the position of the scattering point. If the scintillation crystal is a sphere††† $\overline{F}$ is practically constant. The change in $\overline{\varepsilon}$ might ammount up to about 10% mostly due to the energy dependence of the crystal efficiency. $\sigma_{t1} + \sigma_{t2}$ takes into account that the reduction of intensity by absorption is different for various scattering positions. These weights need not be known with high accuracy as, to a first approximation, they cancel out.

Finally w_p which appears only in the numerator, expresses the influence of the polarization dependent absorption. Fortunately, for photon energies below 1 MeV, w_p is very close to one as $\sigma_c = 0$ at 660 keV.† For higher energies σ_c/σ_t increases (fig. 10) and the value of w_p will be reduced since for the energies in question $\mathrm{d}\sigma_c$ and σ_c have the same sign. Maximum reduction of the asymmetry will occur for quantum energies of about 6 MeV ($w_p \approx 0.6$).

In the expression for w_p the depolarization by scattering is taken care of by $\varkappa$, which is the ratio of the polarization after and before scattering. $\varkappa$ is a function of the photon energy and scattering angle and is plotted in fig. 15. For a scattering angle of about 60° and photon

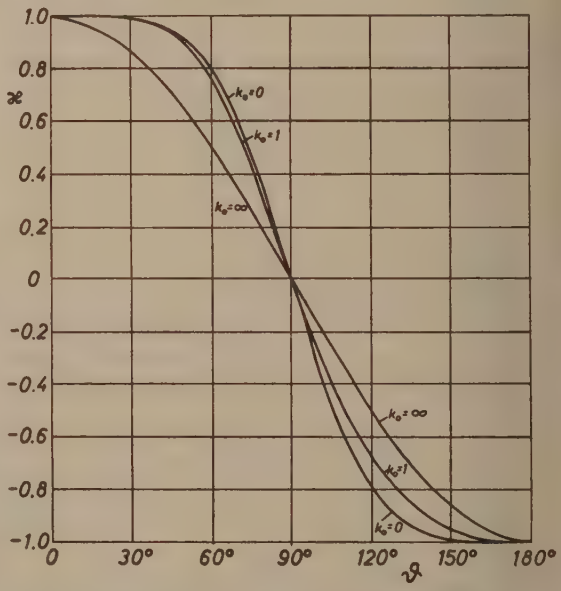

Fig. 15. The ratio of the circular polarization after, to that before scattering (computed with the expression given by Lipps and Tolhoek[16]) as a function of scattering angle ϑ and photon energy k_0 (in units of m_0c^2). The scattering from the oriented electrons was neglected.

† It was assumed that there is no linear polarization ($P_l = 0$).

†† $\mathrm{d}\sigma_c^-$ and σ_c^-, are again the cross sections for the electron spin being approximately antiparallel to the direction of the incident γ-ray ($\pi < \psi \leq 3\pi/2$).

††† The cylindrical crystals generally used can be looked upon as a quite good approximation to a sphere.

† Note that σ_{c1} and σ_{c2} are functions of the angle ψ between the direction of incident photon and electron spin. As, however, for quantum energies up to 1 MeV $w_p \approx 1$, σ_c ($\psi = 0$) as represented in fig. 10 can be used for most calculations.

energies around 1 MeV the polarization will decrease to about 70% of the initial value.

The simplest way to calculate $< d\sigma_c/d\sigma_0 >$ in practical cases is the graphical method. An example will be described in § 4.2.

4.2. THE CYLINDER GEOMETRY

Let us illustrate the calculations of the preceding section by an important example. As shown in a series of papers[1,4,5,9]) the forward scattering method turned out to be very useful for the analysis of circularly polarized γ-rays. Using a geometry with rotational symmetry one gets a high efficiency.

For the geometry shown in fig. 8 the different steps of the calculation are represented graphically in fig. 16 for a γ-energy of 1.25 MeV. In accordance with the considerations of § 4.1 w_p and $\bar{\varepsilon}$ do not vary appreciably. $d\sigma_c$ and $d\sigma_0$, however, change considerably. As a consequence it is of no use to make the magnet longer. No doubt the counting rate is increased thereby but the asymmetry is reduced disproportionately.

In order to compute $< d\sigma_c/d\sigma_0 >$ one has to determine the areas under the curves of fig. 16e and take the ratio. Some difficulty may arise in fixing the limits of the integrals. On account of the finite size of the crystal it is not quite clear which parts of the magnet contribute to the

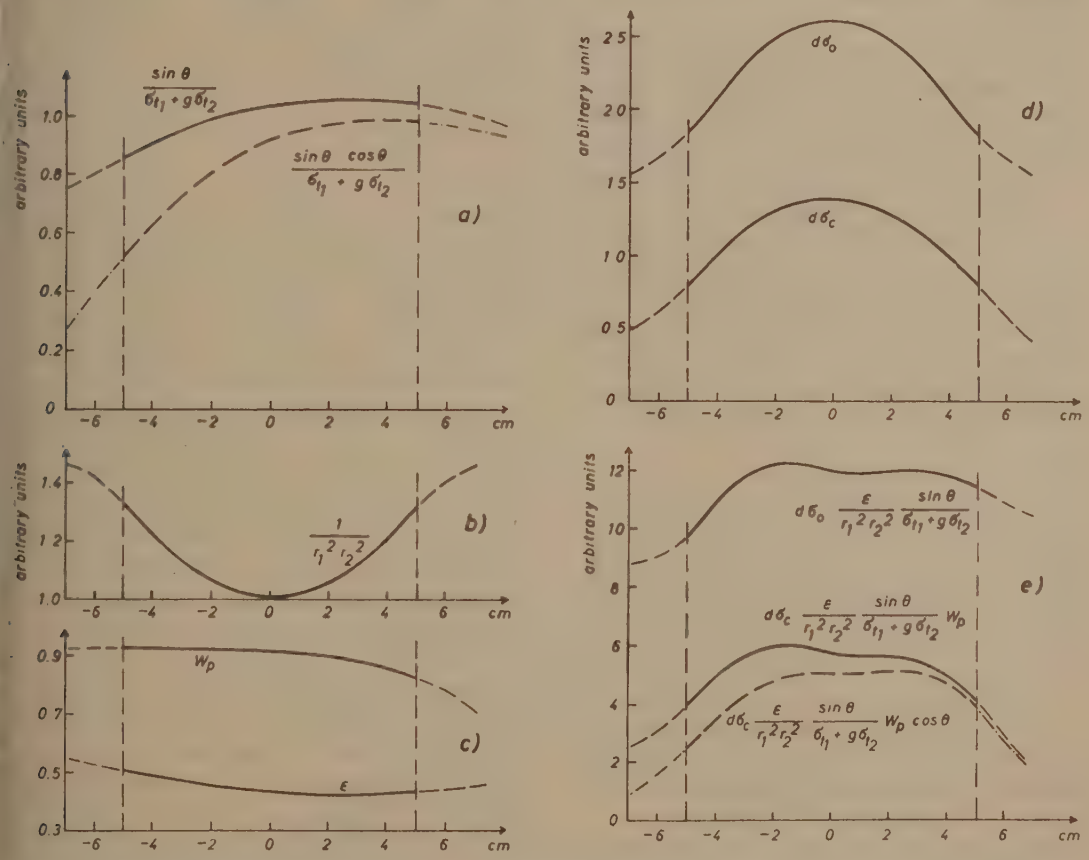

Fig. 16. Graphical representation of the factors and integrands of eq. (19) for the geometry shown in fig. 7 ($\theta = \psi$, r = constant).

scattering. In order to improve this Steffen *et al.*[27]) used conical lead absorbers which define the geometry much better. However, in many cases one can do without such absorbers as it turns out that the integrals do not depend very strongly on the limits. For the example represented in fig. 16 one finds $< d\sigma_c/d\sigma_0 > = 0.473$ for $|z| \leq 4$ cm, and $< d\sigma_c/d\sigma_0 > = 0.452$ for $|z| \leq 5$ cm. Therefore it is thought that the total error in $< \delta\sigma_c/d\sigma_0 >$ will be only of the order of a few percent.

4.3. PLURAL SCATTERING

There are two more processes which one would except to influence the calculation of the magnet response, i.e. multiple and plural scattering.

Multiple scattering, however, is thought to be negligible as the mean free path of the photons in the iron is of the order of 1 cm. On the other hand, the intensity of double scattering might be comparable to that of single scattering as the Compton-cross section decreases with increasing scattering angle and thus the probability for a single scattering e.g. by 60° will be roughly the same as that for two scatterings each by 30°.

The following calculations will show that indeed double scattering cannot be neglected relative to single scattering, but its polarization dependence is very similar to that of single scattering. Consequently, the computations in § 4.2 need not be modified as long as an accuracy of a few percent is satisfactory.

Using the quantities defined in fig. 17 it is easy to show that the ratio of the numbers of double to single scattered quanta, which we denote by ρ, is given for a fixed θ by

$$\rho(\theta) = \frac{d\sigma(\vartheta_1)}{d\sigma(\vartheta)} \int \frac{e^{-\sigma' s'' n_0}}{e^{-\sigma_s s_s n_0}} d\sigma(\vartheta_2)\, e^{-\sigma' s' n_0} \sin\vartheta_1 d\vartheta_1 d\eta ds' \quad (21)$$

where polar coordinates s', η, and ϑ_1 were introduced with the first scattering point as origin. σ' and σ'' are the total absorption coefficients along s' and s'' respectively.

[27]) R. M. Steffen, Proceedings of the Rehovoth Conference on Nuclear Structure (North-Holland Publishing Co., Amsterdam, 1958) p. 419.

An exact evaluation of the integral would be very involved but is not necessary on account of the following reasons. Double scattering processes in which $\vartheta_1 \approx \vartheta$, $\vartheta_2 \approx 0$ or $\vartheta_1 \approx 0$, $\vartheta_2 \approx \vartheta$ will give practically the same polarization effect as single scattering and need not be included in ρ. Furthermore the counting probability of events in which at least one of the

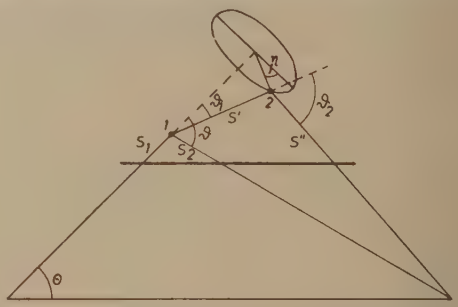

Fig. 17. Pictorial representation of double scattering in the magnet at the points 1 and 2.

scattering angles is large ($\gtrsim 90°$), and the iron path s''_t of the scattered photon is long, will be very low. This will be the case if $\eta > 90°$. Hence complications will arise mainly from double scattering events with $\vartheta_1 \approx \vartheta_2 \approx \vartheta/2$, $\eta \lesssim 90°$. Taking care of these circumstances one can get a rough estimate of ρ. For photon energies in the region of 1 MeV, ρ may have values between 0.1 and 0.3. Thus double scattering cannot be neglected as far as intensity is concerned.

If one calculates the measurable asymmetry $E_{(2)}$, taking into account double scattering, one obtains the relation $E_{(2)} = EK$, where E is the asymmetry produced by single scattering alone and K is given by the formula

$$K = \frac{1 + \varrho m}{1 + \varrho} \quad (22)$$

and

$$m = \frac{\phi_c(\vartheta_1)/\phi_0(\vartheta_1) + \varkappa' \phi_c(\vartheta_2)/\phi_0(\vartheta_2)}{\phi_c(\vartheta)/\phi_0(\vartheta)} \quad (23)$$

$\varkappa'$ is the change in polarization caused by the first scattering of the double scattering.

m averaged over the geometry is generally not very different from 1. This is illustrated by the example shown in fig. 18 where the numerator and the denominator of m are plotted as a

function of z. $\overline{m}$ is found to be 0.87†. With $\rho = 0.2$ one gets $K = 0.98$ which means that the effect will be decreased. But in most cases this small influence of plural scattering wil be smaller than the statistical error.

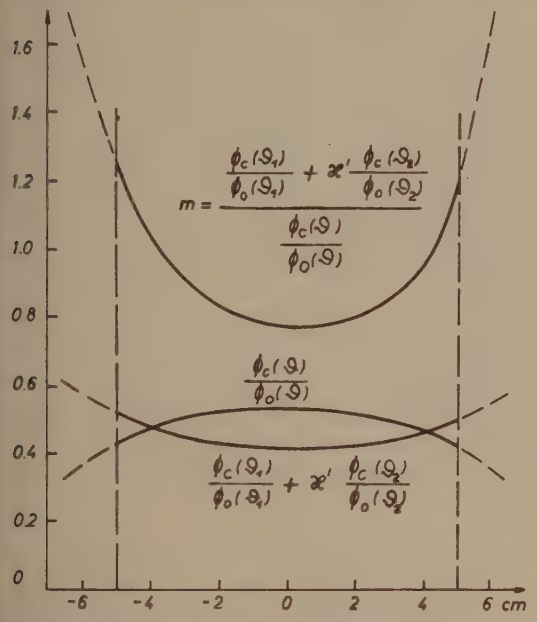

Fig. 18. Plot of the numerator and denominator of eq. (23) and of m for the geometry shown in fig. 7.

4.4. THE DETERMINATION OF f

The fraction of polarized electrons per iron atom may be determined by measuring the magnetic induction in the scattering magnet. The induction B and f are related by the equation $B = H + 4\pi \cdot 26 f \beta n_0$ where H is the magnetic field, β the Bohr magneton and n_0 the number of atoms/cm³. However, there is a contribution to B from the orbital motion of the electrons (approximately 3%) which has to corrected for.

5. β–γ Circular Polarization Correlation

In the foregoing chapters it was assumed that the circular polarization P_c is independent of θ, as will be the case for external and internal bremsstrahlung. In other experiments this may not be true.

The most important case is the measurement of the β–γ circular polarization correlation. For allowed β-transitions the circular polarization of γ-rays is given by [10,28] ††.

$$P_c = A\ (v/c) \cos \tilde{\theta} = -A\ (v/c) \cos \theta \qquad (24)$$

where $\tilde{\theta}$ is the angle between the propagation directions of photon and β-particle (fig. 8) and θ is defined in fig. 14. v and c are the velocities of the electron and photon, respectively. A depends on the type of β-interaction, the γ-transition and the degree of parity violation. By averaging over the magnet geometry P_c can not be considered as constant. Instead of $< d\sigma_c/d\sigma_0 >$ one has now to evaluate the average $< d\sigma_c/d\sigma_0 \cdot \cos\theta >$. If E has been measured A can be calculated with the help of

$$E = -2\, f A\ (v/c) < d\sigma_c/d\sigma_0 \cdot \cos\theta > \qquad (25)$$

where

$$< d\sigma_c/d\sigma_0 \cdot \cos\theta > = \frac{\int \left\langle \frac{\overline{F\varepsilon}}{r_2^2} d\sigma_c - \right\rangle \frac{\sin\theta \cos\theta\, d\theta}{\sigma_{t1} + g\sigma_{t2}}\, w_p}{\int \left\langle \frac{\overline{F\varepsilon}}{r_2^2} d\sigma_0 \right\rangle \frac{\sin\theta\, d\theta}{\sigma_{t1} + g\sigma_{t2}}} \qquad (26)$$

In fig. 16 the results of these calculations were included as broken lines. For $< d\sigma_c/d\sigma_0 \cdot \cos\theta >$ the value 0.407 is found. This deviates somewhat from the value which one would obtain by averaging $< d\sigma_c/d\sigma_0 >$ alone ($< d\sigma_c/d\sigma_0 > \overline{\cos\theta} \approx 0.42$, $|z| \leqslant 4$ cm).

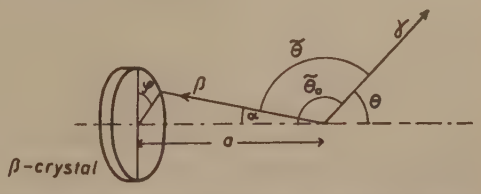

Fig. 19. Pictorial representation of angles necessary to evaluate the influence of the finite size of the β-crystal.

One further correction must be applied on account of the finite size of β-crystal and source. If we assume a point source the angle $\tilde{\theta}$ can have different values for a given angle θ (or $\tilde{\theta}_0$, respectively, (fig. 19)) on account of the extension

† For simplicity the weights (fig. 16) have been omitted as they would not change this estimate appreciably.

†† For forbidden transitions see Alder, Stech and Winther[10]) and Morita[28]).

[28]) M. Morita, Phys. Rev. **107** (1957) 1729.

of the β-crystal. In order to evaluate the average of $\tilde{\theta}$ one has to integrate

$$\cos\tilde{\theta} = \cos\tilde{\theta}_0 \cos\alpha + \sin\tilde{\theta}_0 \sin\alpha\cos\varphi \qquad (27)$$

over φ and α and one obtains

$$\overline{\cos\tilde{\theta}} = \cos\tilde{\theta}_0 \sin\alpha_m/\alpha_m \qquad (28)$$

where α_m is the maximum value of α as determined by the size of the β-crystal and its distance a from the source. Thus $< \mathrm{d}\sigma_c/\mathrm{d}\sigma_0 \cdot \cos\tilde{\theta}_0 >$ should be multiplied by $\sin\alpha_m/\alpha_m$. But for $\alpha_m \leqslant 30°$ the correction amounts to a few percent only.

The easiest way to take into account the finite size of the source, too, is to calculate α_m by the relation $\mathrm{tg}\,\alpha_m = (r_s + r_{cr})/a$ where r_s and r_{cr} are the radii of source and crystals respectively.

In this connection it is interesting to ask which α_m gives the best relative accuracy in a fixed time. That means minimizing $\Delta E/E$ where ΔE is the statistical error of E. ΔE is proportional to $1/\sqrt{1-\cos\alpha_m}$ and E to $\sin\alpha_m/\alpha_m$. From this one finds that $\Delta E/E$ is minimum for $\alpha_m \approx 83°$. However, in many cases such large solid angles cannot be used as the counting rate in the β-counter is limited by pile-up.

The determination of effects which are only of the order of a few percent is not only a question of time necessary to get a sufficient statistical accuracy but also of eliminating small systematic errors. In order to achieve this it is very helpful not to use the registered number of coincidences in order to evaluate E but to divide this number by the singles counting rate. By this procedure, changes in counter efficiencies due to the influence of magnetic stray fields are eliminated. In addition, even time dependent changes drop out completely as long as only one counter is concerned. If both efficiencies vary, only second order effects are not suppressed.

As a final topic the limitation on the source strength will be discussed. It is well known that the ratio between random and genuine coincidences is equal to $2\tau n$ where τ is the coincidence resolution and n the number of decays/sec in the source. If the source strength is too high, the random coincidences will outweigh the genuine ones. On the other hand it can be shown that the error in E is given by

$$(\Delta E)^2 = 2\,(1 + 4\tau n)/tn\,\omega_\beta\omega_\gamma \qquad (29)$$

where $\omega\beta$ and $\omega\gamma$ are the overall efficiencies for the detection of the β- and γ-ray and t is the time of observation. On deriving this expression it was taken into account that the random coincidences must be measured separately and substracted from the total number of coincidences.

From expression (29) it can be inferred that the time necessary to obtain a given relative accuracy will be shorter the stronger the source is. Practically, however, it might not be advisable to make $2\tau n$ larger than 1 because further saving of time is not appreciable whereas the relative change in counting rate is getting small, thus increasing the importance of systematic errors of instrumental origin.

The author would like to thank Dr. Appel, Dr. Bloom, Mr. Jüngst, Mr. Galster, Mr. Hartwig and Mr. Müller for many discussions and for performing some of the calculations.

Appendix

THE DETECTION OF THE LINEAR POLARIZATION OF γ RAYS

Although the main topic of this article is the detection of the circular polarization of γ-rays a few remarks may be added concerning the measurement of the linear polarization.

Again the different interactions of γ-rays with matter can be used for that purpose.

1. *Photoelectric effect*

In the non-relativistic limit the emission of photoelectrons is preferred in the plane of the electric vector. However, if the kinetic energy of the photoelectrons is approximately m_0c^2 a "crossover" takes place. For higher energies the preferred emission is orthogonal to the electric vector. This was verified experimentally by

McMaster und Hereford[29]). Hence this method will be suitable for $h\nu \lesssim 0.4$ MeV only.

2. *Compton effect*

For the detection of the linear polarization Compton scattering is the most favourable method, too, and has been used successfully in many investigations.

As can be inferred from (1) and (2) the scattering of linearly polarized γ-rays occurs predominantly in a direction perpendicular to the plane of the electric vector and incoming photon. It is usual to evaluate the ratio between the number of these electrons and those scattered in the plane of polarization

$$R = \frac{\mathrm{d}\sigma\,(\chi = 90^0)}{\mathrm{d}\sigma\,(\chi = 0^0)} = \tag{30}$$

$$= \frac{1 + \cos^2\vartheta + (k_0 - k)\,(1 - \cos\vartheta) + |P_1| \sin^2\vartheta}{1 + \cos^2\vartheta + (k_0 - k)\,(1 - \cos\vartheta) - |P_1| \sin^2\vartheta}.$$

In order to determine the degree of polarization it might be more suitable to calculate

$$\frac{R-1}{R+1} = \frac{|P_1| \sin^2\vartheta}{1 + \cos^2\vartheta + (k_0 + k)\,(1 - \cos\vartheta)} \tag{31}$$

as this expression is proportional to $|P_1|$.

In the upper part of fig. 20 the scattering angle ϑ_m which gives the maximum value $(R-1)/(R+1)$ is plotted as a function of the photon energy. $(R-1)/(R+1)$ is represented in the lower part of the same figure.

Instead of detecting the photon scattered under an angle ϑ_m one could as well observe the recoil electron emitted under an angle φ_m with respect to the incoming photon. For convenience φ_m is shown also in fig. 20. R and $(R-1)/(R+1)$ are the same, no matter whether the photons or electrons are observed.

From fig. 20 it can be gathered that this method will be useful for energies up to 10 MeV. Above that energy the asymmetry becomes very small.

[29]) McMaster and Hereford, Phys. Rev. **95** (1954) 723.
[30]) T.H. Berlin and L. Madansky, Phys. Rev. **78** (1950) 623; G. C. Wick, Phys. Rev. **81** (1951) 467 and 628; M. M. May, Phys. Rev. **84** (1951) 265; R. L. Gluckstern, M. H. Hull and G. Breit, Phys. Rev. **90** (1953) 1026 and 1030.
[31]) H. Schopper, unpublished.

3. *Pair production*

If an electron pair is produced by a linearly polarized photon one would expect a correlation between the plane of the pair and the plane of polarization.

This problem has been investigated theoretically by several authors[30]). However it turned out that simple cases (e.g. plane of pair contains the incoming photon) are not typical and the general case is very involved†.

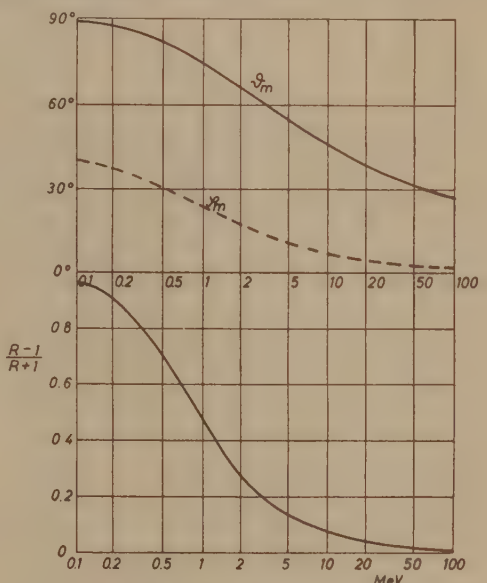

Fig. 20. The detection of the linear polarization of γ-rays. ϑ_m is the scattering angle giving maximum anisotropy $(R-1)/(R+1)$. φ_m is the respective angle between the momentum of recoil electron and incident photon.

Experimentally the pair production in nuclear plates was investigated[31]) using the linearly polarized γ-rays originating from the d(pγ)-reaction ($h\nu \approx 6$ MeV). Unfortunately, statistics are still too bad as the scanning is very laborious and time consuming, so that no definite result can be given.

This method does not seem very promising as the plane of the pair cannot be determined easily, the angle between the electrons being rather small.

† The author would like to thank Prof. Breit for communicating to him unpublished calculations.

4. *Photodisintegration of the deuteron*

The photodisintegration of the deuteron is useful for studying the linear polarization of photons with energies above 5 MeV and up to 50 MeV. As the disintegration takes place in this energy range almost entirely by an electric dipole mechanism the photoprotons are ejected with a $\cos^2 \psi$-distribution where ψ is the azimuthal angle between the proton and the plane of polarization. This was confirmed experimentally by Wilkinson[32]) and the effect has been used by several authors to measure the polarization of γ-rays from various reactions. Up to the present time all experiments were performed with nuclear emulsions impregnated with heavy water. But a proportional counter with a diameter small compared to the range of the photoprotons could be used as well.

[32]) D. H. Wilkinson, Phil. Mag. 43 (1952) 659.

NUCLEAR INSTRUMENTS 3 (1958) 177–178; NORTH-HOLLAND PUBLISHING CO. – AMSTERDAM

LETTER TO THE EDITOR

TWO-CRYSTAL-COMPTON-SPECTROMETER WITH IMPROVED GEOMETRICAL EFFICIENCY

PETER WEINZIERL and GEORG TISLJAR-LENTULIS

Ist Physics Laboratory, University of Vienna

Received 27 May 1958

The low detection efficiency of the Compton-spectrometer described by Hofstadter and McIntyre[1]) is disadvantageous in nuclear decay-scheme work with low level or short life activities.

Omitting the gamma-collimator and placing the source between the two crystals improves the efficiency considerably. No disadvantage results from the wider range of scattering angles: no deterioration of the resolution of the Co^{60} lines with the geometrical arrangement,

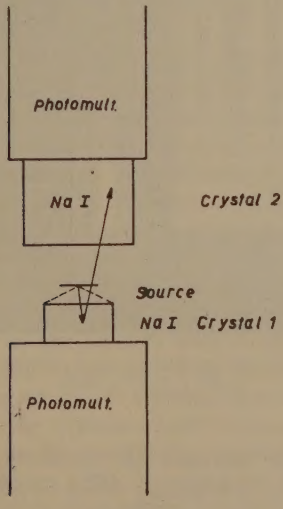

Fig. 1. New arrangement for Compton-spectrometer.

shown in fig. 1, could be noticed, compared with the resolution at much greater source-crystal distances. The diameter of the source area was about 5 mm.

To reduce the number of gamma-gamma coincidences caused by primary quanta in the two crystals, relative to the Comptonscattering coincidences, a kicksorter was applied accepting only those pulses from crystal 2 whose energy falls in the narrow band of back-scattered Compton quanta. A channel width admitting 170 to 280 keV seems to be a reasonable compromise, between overall efficiency and reduction of γ-γ-background for a primary energy range from 0.7–2.5 MeV. In any case a certain number of primary γ-γ-coincidences will be superimposed on the Comptonspectrum but disturbance arises only if the photopeak, or a large portion of the Compton-continuum, of one of the cascade γ-rays falls within this selected energy channel. Correspondingly the use of anthracene as scattering crystal is advisable, if the poorer resolution of this scintillator can be tolerated. In this case the superimposed spectrum does not exhibit any maxima but consists of a distribution that decreases stepwise with energy.

Scattering crystals much thicker than 1 cm (for NaI) are of no advantage: the probability that a back-scattered quantum of about 200 keV penetrates this crystal decreases rapidely with increasing thickness. So the parts of crystal 1 lying farther from the source will not add appreciably to the intensity of the Compton-coincidence spectrum. The superimposed spectrum, however, will be enhanced

[1]) R. Hofstadter and J. A. McIntyre, Phys. Rev. 78 (1950) 619.

since the primary γ-γ coincidences increase proportional to the crystal volume.

Figs. 2 and 3 are gray-wedge Compton-spectra of Co^{60}, and of a mixed test-source containing Cs^{137}, Co^{60} and Y^{88}. Fig. 3 shows a faint superimposed photopeak at 1.33 MeV.

The electronics consist of a fast-slow coincidence assembly, using EFP 60 triggers, and a special wave-forming circuit[2]) which, for NaI-pulses, operates with a resolving time of $5–8 \times 10^{-8}$.

The overall efficiency of the method, i.e. the ratio of coincidences registered within the Compton-peak, to emitted quanta was determined for the following energies:

Cs^{137}	662 keV	$7.0 \pm 0.7 \times 10^{-4}$
Y^{88}	908 keV	$5.8 \pm 0.6 \times 10^{-4}$
Na^{22}	1280 keV	$4.5 \pm 0.5 \times 10^{-4}$
Y^{88}	1850 keV	$2.7 \pm 0.3 \times 10^{-4}$

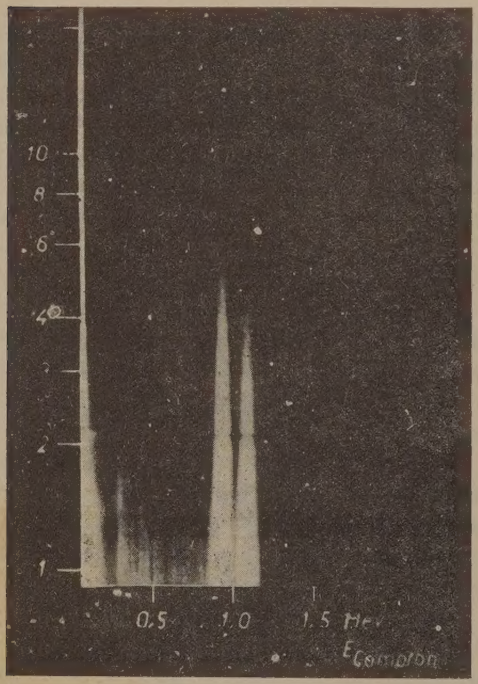

Fig. 2. Gray-wedge spectrum of Co^{60}, measured in the geometry of fig. 1.

For a recent construction of the original Hofstadter-type spectrometer[3]) the efficiency per quantum hitting the scattering crystal is given. Assuming that about 10 cm distance between source and crystal are necessary for an efficient shielding arrangement our new version of the Compton spectrometer gives an increase of overall efficiency by about two orders of magnitude.

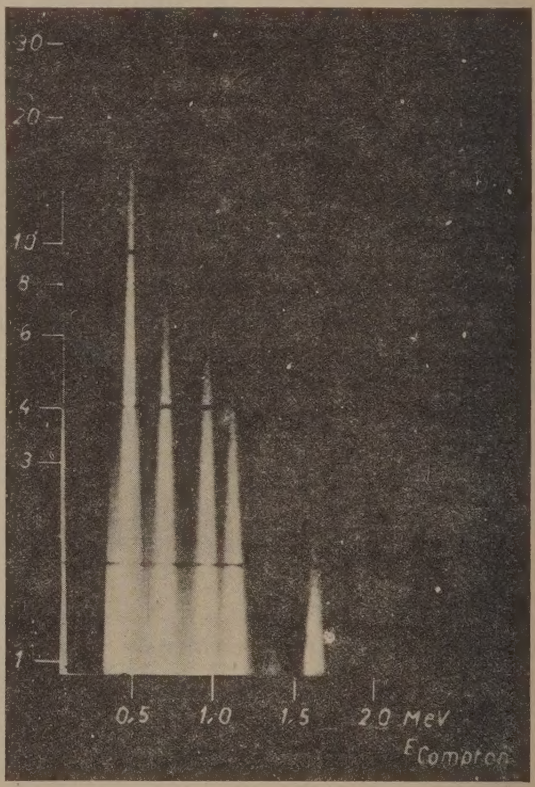

Fig. 3. Gray-wedge spectrum of a mixed test source (Co^{60} + Co^{137} + Y^{88}).

A further increase of efficiency, without impairing line resolution, could be achieved by using specially shaped crystals.

[2]) P. Weinzierl, Rev. Sci. Instr. **27** (1956) 226.
[3]) Howland, Scofield and Taylor, Nucleonics **14** (1956) 50.

NUCLEAR INSTRUMENTS 3 (1958) 179–180; NORTH-HOLLAND PUBLISHING CO. – AMSTERDAM

BOOK REVIEWS

I. T. KAHAN, M. GAUZIT, *Physique et calcul des réacteurs nucléaires* (Dunod, Paris, 1957, XIV + 388 p., 133 fig. 3900 frs).

II. M. GAUZIT, T. KAHAN, *Contrôle et protection des réacteurs nucléaires* (Dunod, Paris, 1957, XIV + 396 p., 180 fig. 3900 frs).

Both books are part of the series "Introduction au genie nucléaire", which eventually will consist of three volumes treating the physical and engineering problems associated with the development of nuclear energy.

The first volume starts with a survey of atomic and nuclear physics including the fission process and then follows a chapter about neutron physics. The main part is, however, devoted to the stationary reactor theory and reactor dynamics and in the last chapter various reactor types are used as examples for calculations.

The second volume is divided into four chapters, namely the detection of radiation with an extensive description of various detectors, the control and safety systems of reactors, including power calibration and stabilization, the radiation hazards and biological effects, and an informative treatment of the shielding problems. In an appendix the fusion process is described.

A third volume is announced and it will treat the problems connected with power reactors.

Obviously an introductory work of this kind cannot give a complete account of all the problems involved in the matter. It appears, however, that in certain cases the references could be more complete with regard to the information published at the Geneva conference 1955. For example the method using a pulsed neutron source in order to find the diffusion and the absorption properties of either clean or poisoned moderators has not been mentioned. Also no remarks have been made regarding the discrepancies of different measurements of the resonance integral. In the first volume more cross-references would have been desirable. References could also advantageously have been given in the text of the figures.

The general impression is, however, that the volumes are well edited. Figures and diagrams illustrate the text instructively, and a lot of references are given, especially in the second volume. The work can be recommended as a good introduction into the field of nuclear energy.

ROLF PERSSON

E. H. GRAUL, *Strahlensyndrom — Radioaktive Verseuchung* (Verlag Gasschutz und Luftschutz, Koblenz, 180 p., DM. 22.40).

Lately there have appeared some excellent monographs on the biological effects of ionizing radiation, among which the official British and United States' reports, The Hazards to Man of Nuclear Radiation and The Biological Effects of Atomic Radiation, respectively, are to be noted. The author of the present book has a similar aim but the illustrates the fundamental radiobiological and medical problems starting out from rather detailed studies of a small number of selected cases of radiation injuries. Among the cases discussed are a lethal overexposure in connection with a reactor accident in Los Alamos 1945 and the exposure of the crew of a Japanese fishing boat at the hydrogen bomb experiment at Bikini 1954. In connection with the analysis of the given examples the author then summarizes the results of related experimental studies with animals as well as the various radiobiological, biophysical and biochemical facts that are necessary for understanding them.

With its orientation it is natural that the book centers about the effects of very heavy exposures, but the interesting questions of late effects—including genetic ones—of low level exposure are also considered.

As a result of many carefully chosen pictures the author has succeeded in presenting a clear and readable report, within limited space, of the harmful effects of ionizing radiation. The fact that the author's own concern with radiation is mainly from a clinical viewpoint need therefore not discourage technical people, who are interested in the problem, from reading the book.

ARNE HEDGRAN